Syntheses, Structures, and Electronic Properties of Novel Polyaromatic Hydrocarbons Annulated with Sulfur and Nitrogen Heterocycles

硫黄及び窒素を含むヘテロ環が縮環した新規多環芳香族化合物の合成、構造、及び電子物性

Yongfa XIE

謝　永發

Department of Chemistry,

Graduate School of Science

Nagoya University

August 2013

Table of contents

Chapter 1 General introduction 3

1.1 Introduction 3

1.2 Aromatic π-conjugated systems for semiconductors 5

1.2.1 Acenes for semiconductors 5

1.2.2 Heterocyclic polyaromatics for organic semiconductors 7

1.2.3 Thiophene-fused materials for organic semiconductors 9

1.2.4 Thiadiazole-fused materials for organic semiconductors 15

1.3 Organic field effect transistors (OFETs) 16

1.4 Fused polyaromatic molecules containing hetero-atoms for organic electronics 19

References 20

Chapter 2 Synthesis, optical properties and charge transport characteristics of a series of novel thiophene-fused phenazines ... 27

2.1 Introduction 27

2.2 Results and discussion 28

2.2.1 Synthesis 28

2.2.2 Electrochemical properties 30

2.2.3 Optical properties 31

2.2.4 Theoretical calculations on the electronic properties of phenazines and anthracene analogues 34

2.2.5 X-Ray Crystallography 40

2.2.6 Preparation, characterization, and FET performance of thin-films 43

2.2.7 Theoretical calculation on charge transport properties of thiophene-fused phenazines 48

2.2.8 Chemical doping effect on transport properties 49

2.3 Conclusion 52
2.4 Experiment section 53
2.5 Appendix 66
References 85

Chapter 3 Synthesis, structures and electronic properties of novel acceptors: thiadiazole-fused aromatics 89

3.1 Introduction 89
3.2 Results and discussion 93
3.2.1 Syntheses 93
3.2.2 Molecular orbital calculation 95
3.2.3 Electrochemical and optical properties 96
3.2.4 X-ray crystal structures 99
3.2.5 Preparation, characterization, and FET performance of thin films 102
3.2.6 Preparation, crystal structures, and magnetic properties of anion radical salts 107
3.3 Conclusion 115
3.4 Experimental section 116
3.5 Appendix 125
References 135

Chapter 4 Conclusion 138

Acknowledgements 140
List of publications 141

Chapter 1 General introduction

1.1 Introduction

In the ancient times, human beings utilized natural products without any knowledge of their chemical structures. With the development of modern chemistry, the ingredients of natural products such as dyes and medicines were extracted, and their chemical structures were determined and reproduced artificially. Due to the development of the field of organic chemistry in the 20th century, large numbers of artificial molecules have been synthesized.

Currently, our life deeply depends on electronic devices, and these systems are controlled by electronic circuits consisting of semiconductors. Silicon, germanium, gallium arsenide, and gallium nitride are typical semiconductor materials, and they are all crystalline inorganic materials, conventionally included in the class of ceramic materials. In contrast, "organics" primarily in the form of plastics, are generally regarded as electrical insulators. However, a new field of electronics has emerged with the discovery of conducting and semiconducting organic materials. In recent years, many researchers have made a significant effort to investigate organic electronics. Electronic devices containing organic materials have already exhibited multiple applications such as organic light-emitting diodes (OLEDs), organic photovoltaics (OPVs), and organic field effect transistors (OFETs). Table 1-1 lists in chronological order the major landmarks in the progress of organic materials for electronics.

As shown in Table 1-1, the field of organic conductors was opened with perylene-bromine salt[1] in 1950's. The first metallic organic conductor, TTF-TCNQ[2], and the first organic superconductor, $(TMTSF)_2PF_6$, are brilliant achievements in this field, and the highest T_c (transition temperature to superconductor state) was increased to more than 10 K.[3] Meanwhile, the field of "organic electronics" has also been developed. For example, an organic field effect transistor was prepared with

Table 1-1. Progress of organic materials for electronics.

Year	Materials	Properties	Reference
1954	Perylene-bromine	σ = ca 1.0 S cm^{-1} (first organic conductor)	1
1962	TCNQ	Semiconductive metal salts	3b
1973	TTF-TCNQ	σ_{rt} = 500 S cm^{-1} (the first organic metallic conductor)	3a
1977	Polyacetylene	The first conducting polymer	11
1980	$(TMTSF)_2PF_6$	The first organic superconductor	9a
1983	Polyacetylene	The first OFET, $\mu = 10^{-5}$ cm^2 V^{-1} s^{-1}	4
1992	K_3C_{60}	Superconductor, T_c = 19 K	9b
1997	Pentacene	OFET, μ = ~ 1.0 $cm^2V^{-1}s^{-1}$	5
1999	P3HT	OFET, μ = ~ 0.1 $cm^2V^{-1}s^{-1}$	7
2008	Picene	OFET, μ = > 1.0 $cm^2V^{-1}s^{-1}$	6
2009	Rubrene	Single crystal OFET, μ = ~ 40 cm2$V^{-1}s^{-1}$	8
2010	A_xPicene (A = alkali metal)	superconductors	21

polyacetylene and showed a low mobility of 10^{-5} cm^2 V^{-1} s^{-1} in 1983.[4] In the past decades, many well-known novel materials such as, pentacene[5], picene[6], P3HT[7], and rubrene[8] have been developed for organic electronics.[9] Approximately 25 years later, it was found that rubrene exhibits very high mobility up to 40 cm^2 V^{-1} s^{-1} in the single crystal state.[8] Providing such novel molecules is essential for the progress of organic electronics, and synthetic organic chemists must contribute to the development of novel electron donors or acceptors for electronics.

Interest has grown with regard to utilizing organic materials for electronics for the following three reasons.[10] First, the size scale of the molecules is between 1 and 100 nm. The scale of functional devices therefore allows for acceptable density of integrated circuits, cost, efficiency, and power dissipation. Second, a certain nanostructure can be formed through self-assembly of small molecules with specific intermolecular interaction. Molecular recognition can also be utilized to modify electronic behavior, providing both switching and sensing capabilities. Finally, by choice of composition and geometry, the physical properties of the molecule, including their optical and transport properties, can be varied extensively. Since various synthetic methods have been developed, any kind of molecule can be synthesized, if it is stable. Although molecules do have some disadvantages such as

instability at high temperatures, these four advantages render molecules potentially very useful for electronic applications.

1.2 Aromatic π-conjugated systems for semiconductors

Since the discovery of highly conducting polyacetylene by Shirakawa, MacDiarmid, and Heeger in 1977,[11] π-conjugated systems have attracted much attention as futuristic materials for the next generation of organic electronics. In particular, aromatic π-conjugated molecules have been widely investigated. The first reason is that an aromatic ring has six π electrons ($4n$+2) and hence their aromaticity contributes to the stability of the materials. The stability of the thiophene-fused materials ensures their potential application for organic semiconductors. Next, their molecular orbitals usually delocalize over the whole π-extended structure, which increases the intermolecular overlaps and enhances the intermolecular charge transport properties. In addition, aromatic π-conjugated molecules often exhibit interesting optical properties due to the narrow bandgaps. To date, the great number of π-conjugated semiconducting materials that have been either discovered or synthesized generate an exciting library of π-conjugated systems for organic electronics such as acenes, thienoacenes, oligomers, TTF and its derivatives, phthalocyanines, and imide derivatives.

1.2.1 Acenes for semiconductors

Typical acenes and fused arenes of aromatic hydrocarbons shown in Scheme 1-1 have wide spread π-conjugated structures. Anthracene (**1**) has been tested for OFETs, and its single crystal devices exhibit a mobility of 0.02 $cm^2\ V^{-1}s^{-1}$ at low temperature.[12] Gundlach et al.[13] have found that a thin film field-effect transistor of tetracene (**2**) showed a mobility of 0.1 $cm^2\ V^{-1}\ s^{-1}$ with a current on/off ratio of 10^6 on octadecyltrichlorosilane (ODTS)-modified SiO_2 substrates. Its single crystal transistors[14] provided a mobility of 2.4 $cm^2\ V^{-1}\ s^{-1}$ by using poly(dimethylsiloxane) (PDMS) as the dielectric layer. A thin film transistor of pentacene (**3**) exhibited

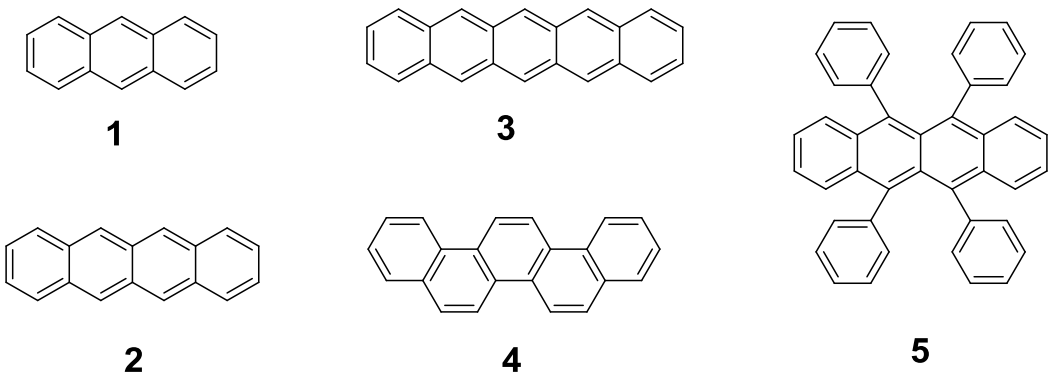

Scheme 1-1. Molecular structures of acenes.

mobilities of up to 1.5 $cm^2 V^{-1} s^{-1}$ with an on/off ratio of over 10^8, a threshold voltage of about 0 V, and a subthreshold slope of less than 1.6 V/decade.[15] when polycrystalline film of pentacene was used for OFETs, the mobility approached 5.0 $cm^2 V^{-1} s^{-1}$ with an on/off ratio of over 10^6.[16] Obviously, the field-effect mobility is increased when going from anthracene to pentacene with the extension of the π-conjugated systems. This increase is attributed to the associated benefits of intermolecular orbital overlap and the fact that charge transport is facilicated (for a larger transfer integral and a lower reorganization energy).[17]

Picene (**4**) has five benzene rings, as in pentacene, but the molecular structure is W-shaped. The crystal shows herringbone stacking in the *ab*-plane,[18] and the structure is similar to that of pentacene. A hole mobility value, greater than 1 $cm^2 V^{-1} s^{-1}$, was achieved in a picene thin-film FETs.[6] Furthermore, interesting characteristics were also observed in the FET: the mobility increased when the FET was exposed to O_2 gas.[19] The field-effect performance of picene was also investigated in the crystalline state. A high mobility value of more than 1 $cm^2 V^{-1} s^{-1}$ in a two-terminal measurement is obtained in picene single crystal FET with a parylene-coated HfO_2 gate dielectric.[20] Picene also exhibited superconductivity upon alkali metal doping.[21]

Rubrene (**5**) is a representative semiconductor material for single crystal OFETs. Such single crystal OFETs were first constructed by Pdzorov *et al* with parylene as gate dielectrics,[22] after which laminated-crystal OFETs were also developed.[23] This compound turned out to be highly compatible with both device structures, resulting in

very high mobility values up to 40 $cm^2 V^{-1} s^{-1}$.[8,24]

1.2.2 Heterocyclic polyaromatics for organic semiconductors

Many organic materials, containing hetero-atoms, such as sulfur, nitrogen, etc., have been used for organic electronic devices. Several features of these materials have led researchers to concentrate on these materials. First, the hetero-atoms produce characteristic electronic structures, due to their electron negativity and valency. Second, the intrinsic intermolecular interactions such as S ··S, S ··N contacts, affect the crystal packing motif, which governs the carrier transport in solid state. Finally, the hetero-atoms easily coordinate to metal ions to form complexes. Scheme 1-2 shows the well-known organic semiconductors, phthalocyanines and naphthalene diimides with hetero-atoms for organic electronics.

The phthalocyanines have been widely investigated for applications to OFETs and organic solar cells. Copper phthalocyanine (CuPc) (**6a**), titanyl-phthalocyanine (TiOPc) (**6b**) and vandyl-phthalocyanine (VOPc) (**6c**) are representative molecules in this family. Of these nitrogen-containing heterocyclic semiconductors, CuPc was probably the first material, for the application to OFETs. Highly ordered, evaporated thin films[25] of CuPc showed a hole mobility of 0.02 $cm^2 V^{-1} s^{-1}$ and a on/off current ratio of 10^5. The mobilities of the single-crystal transistors of CuPc were found to reach up to 1 $cm^2 V^{-1} s^{-1}$.[26] The molecular structures of TiOPc and VOPc are different from those of the planar metal phthalocyanines; these two are non planar, polar molecules. The TiOPc evaporated films[27] exhibit four phases: an amorphous phase, monoclinic phase I (β), triclinic II (α), and phase Y. The crystals of the α phase adopta typical lamellar structure with a large π-π overlap, suggesting a strong π-π intermolecular interaction. Thin film transistors based on the α phase show a mobility of over 1 $cm^2 V^{-1} s^{-1}$ and reaches as high as 10 $cm^2 V^{-1} s^{-1}$.[28] High quality VOPc films were obtained, when they were deposited on the thin ordered para-sexiphenyl layers

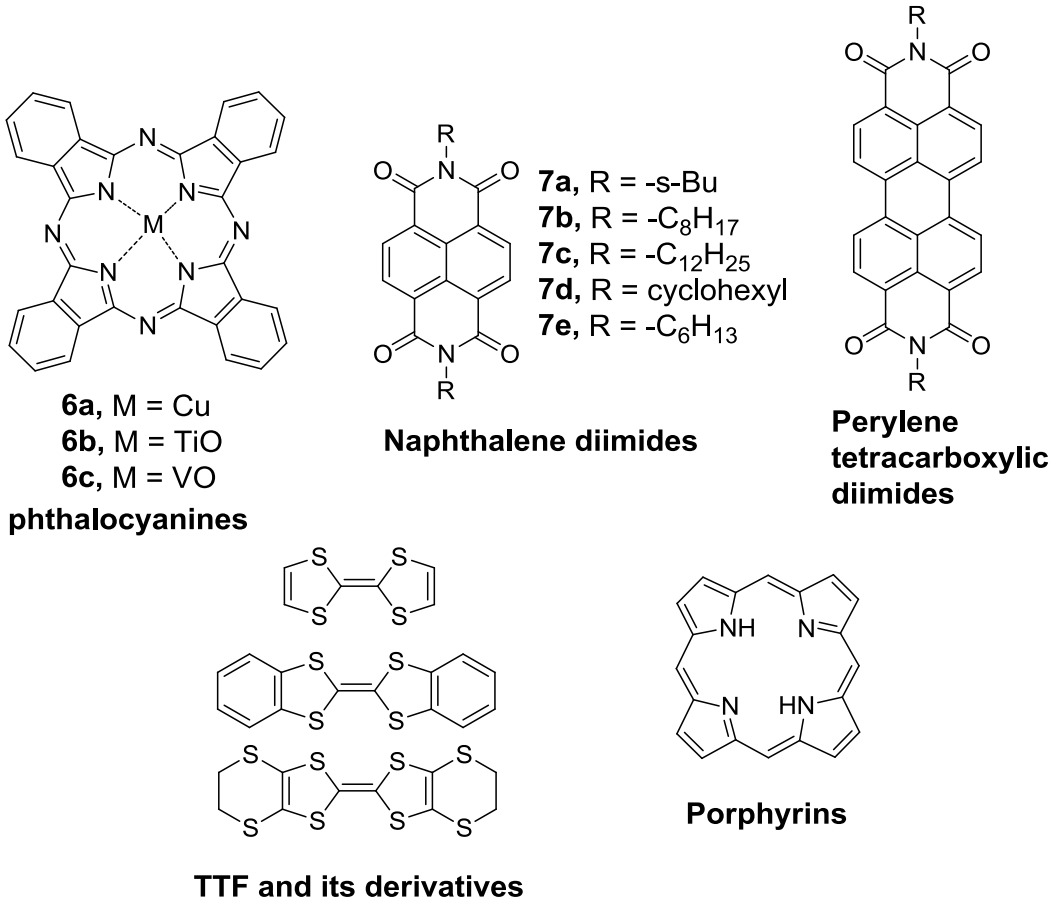

Scheme 1-2. Typical organic semiconductors: Phthalocyanines, Naphthalene diimides, Perylene tetracarboxylic diimides, TTF derivatives, and Porphyrins.

at a high substrate temperature.[29] Transistors based on these VOPc films exhibit a mobility of 1.5 $cm^2 V^{-1} s^{-1}$.[17]

Naphthalene diimide derivatives (NTCDI) (**7a-e**)[30] are a group of the molecules with four carbonyl groups which act as strong electron-withdrawing groups, like a halogen or cyano-group. As a result, these derivatives show n-channel OFET properties. It is found that the naphthalene diimides with alkyl substitutents on the N atoms exhibit high electron mobilities. For instance, the octyl-substituted derivative (**7b**) shows a mobility of 0.16 $cm^2 V^{-1} s^{-1}$, and the sec-butyl (**7a**) and dodecyl functionalized derivatives (**7c**) possess the mobilities of 0.04 and 0.01 $cm^2 V^{-1} s^{-1}$, respectively. Interestingly, the cyclohexyl-substituted naphthalene diimide (**7d**) exhibit a much higher electron mobility of 6.2 $cm^2 V^{-1} s^{-1}$, while the hexyl-substituted corresponding derivative (**7e**) exhibits a peak saturation mobility of only 0.16 $cm^2 V^{-1} s^{-1}$. The significant difference in mobility between these two naphthlalene diimides

(**7d** and **7e**) is mainly attributed to their different molecular packings in the crystals and their different thin-film morphologies, as described in the literature.[30e]

Perylene tetracarboxylic diimides,[31] TTF derivatives,[32] and porphyrin derivatives[33] are also representative candidates for organic semiconductors. Many derivatives of them have been developed for organic semiconductors in recent years.[17]

1.2.3 Thiophene-fused materials for organic semiconductors

In recent years, thiophene-fused polyaromatics have become one of the most important categories for organic field-effect transistor materials. This rise in importance can be explained in several ways. First, the thiophene ring has six π electrons ($4n$+2) and hence its aromaticity contributes to the stability of the materials. The stability of the thiophene-fused materials ensures their potential application for organic semiconductors. Second, compared to the corresponding benzene-ring based materials, these containing thiophene create planar packing structures that can increase the intermolecular overlap in the solid state, thus enhancing the intermolecular charge-transport properties (e.g., polythiophenes or oligothiophenes).[34] Finally, sulfur atoms can create S ··S, S ··H, and S ··π intermolecular contacts, thus enhancing the intermolecular interactions. These interactions can change the packing motifs, and then facilitate charge transport of the organic semiconductors. With the introduction of sulfur atoms, even more extended thienoacenes with six or seven fused aromatic rings exhibit excellent OFET performance and high stability. Some well-known thiophene-fused materials will be introduced below.

1.2.3.1 Oligothiophenes

Oligothiophenes in particular have attracted attention since the discovery of OFETs because (1) oligothiophenes prefer planar structures rather than nonplanar structures as are present in oligophenyls (planar structures are possible under particular conditions), (2) it is much easier to modify thiophene rings than benzene rings due to their high reactivity. Take molecules **8a-d** as an example,[35] their mobilities have

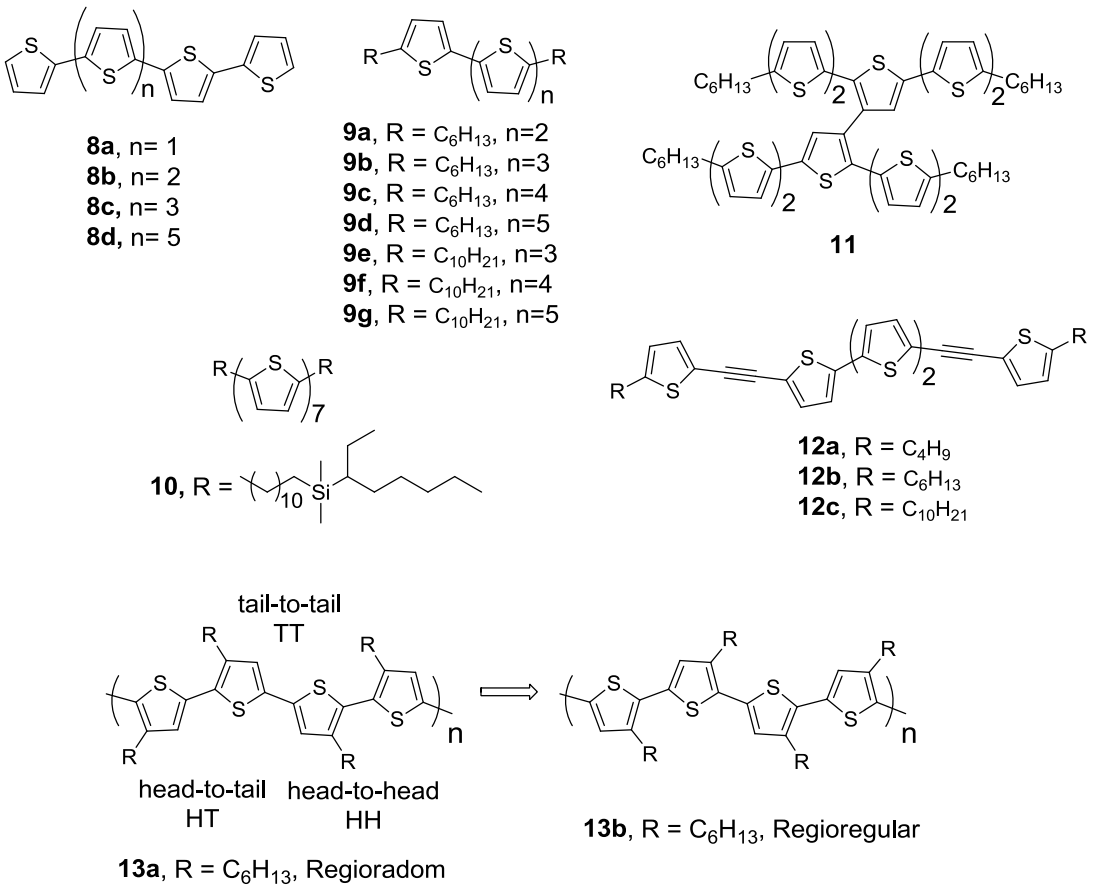

Scheme 1-3. Molecular structures of oligothiophenes.

improved from 10^{-4} cm^2 V^{-1} s^{-1} to 0.1 cm^2 V^{-1} s^{-1} in the past few decades, while that of the octithiophene (**8d**) has reached up to 0.28 cm^2 V^{-1} s^{-1}.[36] The introduction of alkyl chains is useful for improving the solubility of the organic materials. It is facile to modify thiophenes at the 2, 5-positions; moreover, substitution will improve the stability of the resulting oligomers. Hence, the alkylated oligomers (**9a-g**) have been widely studied.[36a] Moreover, many studies have shown that a appropriate substitution of alkyl groups improves the field-effect performance of organic compounds.[37] For example, mobilities have increased from 2.5×10^{-3} cm^2 V^{-1} s^{-1} to 0.03 cm^2 V^{-1} s^{-1} for quaterthiophene (from **9a** to **9b**) and from 0.02 cm^2 V^{-1} s^{-1} to 0.08 cm^2 V^{-1} s^{-1} for sexithiophene (from **8c** to **9d**), respectively.[38] Many swivel cruciforms have also been synthesized, but only very poor OFET performance has been observed because of the swiveling structures.[39] The highest performance has been exhibited by α,α'-dihexylpentathiophene (**11**) with a mobility up to 0.012 cm^2 V^{-1} s^{-1}.

Oligothiophenes with alkylsilyl as an end-capping group (**10**) have been obtained, exhibiting a mobility of 0.18 $cm^2\ V^{-1}\ s^{-1}$.[40] Oligothiophenes linked by carbon-carbon triple bonds (**12a-c**) have also been examined recently.[41] The self-organizing liquid-crystalline monodomain films of triple bond-linked molecules (**12a-c**) show ambipolar performance with hole mobilities of up to 0.02 $cm^2\ V^{-1}\ s^{-1}$ and electron mobilities of up to $2 \times 10^{-3}\ cm^2\ V^{-1}\ s^{-1}$.

Alkylated polythiophenes have been reported to be semiconductor or solar cell materials, and the substitution of the alkyl chain and the arrangement of side chains play an important role in the electronic properties of alkylated polythiophenes. P3HT (**13a**), reported in early work was regiorandom; with the alkyl chains being substituted in ether 3- or 4-positions. In regiorandom P3HT, there are three kinds of random coupling: head-to-head (HH), tail-to-tail (TT), and head-to-tail (HT) coupling. The HH coupling creates a sterically twisted structure in the polymer backbone, thus decreasing the π-conjugated length of the chain. Using suitable synthetic methods, more regioregular P3HT (**13b**) was obtained with a regularity of up to 99%. The regularity of P3HT plays an important role in the molecular arrangement and OFET behaviors. At room temperature, high mobilities of 0.05 ~ 0.1 $cm^2\ V^{-1}\ s^{-1}$ are observed for the P3HT samples with high regioregularity of 96%, in contrast, for the spin-coated P3HT samples with HT ≈ 81%, the mobility is only $2 \times 10^{-4}\ cm^2\ V^{-1}\ s^{-1}$.[7] P3HT is also considered as a benchmark bulk-hetero-junction OPV hole conducting polymer. Power conversion efficiencies (PCEs) in excess of 5% for single-layer devices,[42] and more than 6% in tandem cell configuration[43] have been reported for regioregular P3HT when it is blended with 1-(3-methoxycarbonyl)propyl-1-phenyl[6,6]C_{61} (PCBM) as an acceptor.[44]

1.2.3.2 Thienoacenes

Pentathienoacene (PTA, **15**) reported by Liu's group,[45] is a pentacene analogue, which has a similar conjugation structure and π electrons to that of pentacene. However, the HOMO energy level of PTA (-5.3 eV) has been found to be lower than that of pentacene (-5.0 eV), and its energy gap (3.2 eV) is much larger than that of pentacene (1.8 eV). These results indicate that PTA is more stable than pentacene in

air. It also showed a mobility of up to 0.045 cm^2 V^{-1} s^{-1} in the thin film state. Recently, a series of thieno[3,2-*b*]thieno[2', 3':4,5]thieno[2,3-*d*]thiophene (**14**) and its derivatives[46] with aromatic substituents showed mobilities larger than 0.1 cm^2 V^{-1} s^{-1} together with ideal solubility and environmental stability. It was found that fused thiophenes with seven (**16a**)[47] or eight thiophene rings (**16b**)[48] still exhibit much better stability than the benzene-based analogues.

Thienoacenes with benzene end-capped rings have also been widely studied. For example, alkylated benzothieno[3,2-*b*] benzothiophene (BTBT) derivatives (**17b**)[49] have been found to be highly soluble in common organic solvents, and their spin-coated films show mobilities over 0.1 cm^2 V^{-1} s^{-1}. The derivatives with

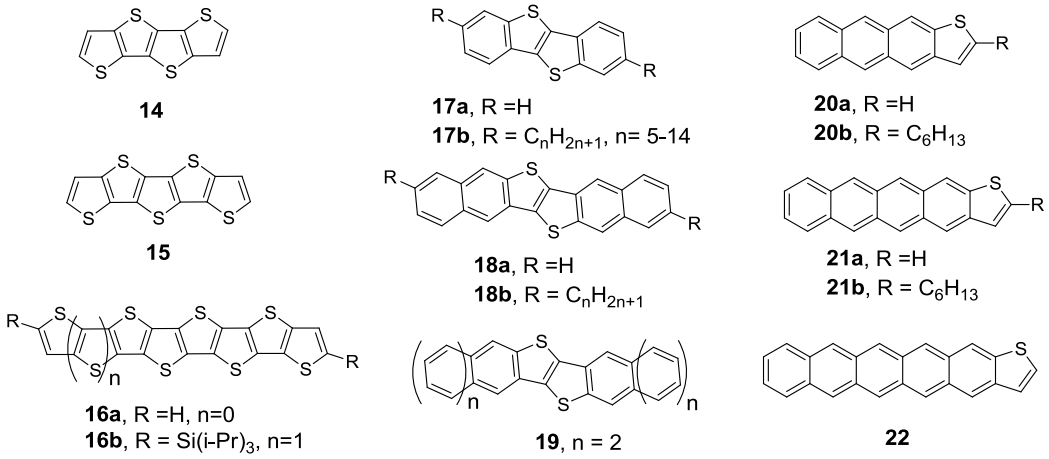

Scheme 1-4. Molecular structures of thienoacenes.

$C_{13}H_{27}$ alkyl chains give the highest device performance with mobilities of 2.75 cm^2 V^{-1} s^{-1} and on/off ratios of up to 10^7. Large extension of π-framework structures (DNTT, **18a** and DATT, **19**) of BTBT have been obtained by fusing more benzene rings on both sides of the BTBT core. Theoretical HOMO levels of these materials (-5.58, -5.18, and -4.88 eV for BTBT, **17a**; DNTT, **18a**; and DATT, **19**, respectively) increase gradually and their band gaps (4.32, 3.37 eV, and 2.66 eV for BTBT, **17a**; DNTT, **18a**; and DATT, **19**, respectively) decrease. However, DNTT and DATT still keep relatively low-lying HOMO energy levels that are sufficient for air stability, to afford mobilities up to 3.1 and 3.0 cm^2 V^{-1} s^{-1} for DNTT and DATT by vapor deposition, respectively.[50] Furthermore, alkylated DNTT derivatives (**18b**) show

enhanced mobilities in vapor-deposited thin film transistors (up to 7.9 $cm^2 V^{-1} s^{-1}$)[51] and solution-processed single-crystalline film transistors (up to 12 $cm^2 V^{-1} s^{-1}$).[52] This work on the thienoacenes system was mainly carried out by Takimiya's group.

To improve the stability of acenes, anthrathiophenes (**20**), tetraacenothiophenes (**21**), and pentacenothiophene (**22**) were synthesized. They have only one thiophene ring as an end-capped group.[53] The compounds, **20a** and **21a** show lower HOMO energy levels and larger band gaps than the corresponding ones of pentacene. They are indicative of their higher stability of **20a** and **21a**. Thin film OFETs of **20a** and **21a** show mobilities of 0.15 and 0.47 $cm^2 V^{-1} s^{-1}$. For comparison, **20b** and **21b** with long alkyl chain have also been examined.[53c] The mobilities for these two compounds are 0.12 and 0.23 $cm^2 V^{-1} s^{-1}$, respectively. Recently, a hexacene analogue pentaceno[2,3-*b*]thiophene (**22**)[53a] was synthesized by Bao' group. It showed much higher stability than hexacene, and its thin film OFETs exhibited a mobility of 0.57 $cm^2 V^{-1} s^{-1}$.

1.2.3.3 Fused aromatic sulfur-containing compounds

Isomeric fused heteroarenes (the NDT derivatives, **23**) that are isoelectronic with pyrene were developed by Takimiya's group.[54] Comparing with pyrene, the HOMO energy levels of NDT were found to be greatly increased, while the LUMO energy levels were lowered due to the aromatic character being reduced by the loss of the kekulé benzene rings in the skeleton. The thienyl substituted anti-NDTs, **23a** and **23b** showed low mobilities of 10^{-4} and 10^{-2} $cm^2 V^{-1} s^{-1}$, respectively. The highest performance was obtained for naphthyl substituted NDT, **23d** with a mobility of 0.11 $cm^2 V^{-1} s^{-1}$, whereas the phenyl substituted NDT, **23c** showed only a low mobility of 10^{-2} $cm^2 V^{-1} s^{-1}$.

A series of tetrathienoacenes was synthesized by Perepichika's group and Pei's group. The acene cores were anthracene, chrysene, and benzo[1,2-*b*:4,5-*b'*]bis[*b*]benzothiophene, which provide the compounds **24a-e**,[55] **25**,[56] and **26**,[57] respectively. The vapor-deposited thin film of **24d** showed very low mobility of 10^{-4} $cm^2 V^{-1} s^{-1}$, while its mobility was improved up to 0.012 $cm^2 V^{-1} s^{-1}$ by thermal annealing at 230 ^oC for 20 min. Perepichika's group showed that the

isomeric hexylate compounds **24b** exhibited a higher mobility of 0.074 cm^2 V^{-1} s^{-1} than **24d**. Interestingly, alkyl-functionalized chrysene derivatives (**25a**, **b**) exhibited mobilities as high as 0.4 cm^2 V^{-1} s^{-1} in their vapor-deposited films. In addition, the benzo[1,2-*b*:4,5-*b'*]bis[*b*]benzothiophene derivative (**26**) showed a good self-assembly character, and its transistors, formed with their mircrowires via slow crystallization, showed typical p-channel behavior with a high mobility of 2.1 cm^2 V^{-1} s^{-1}.[58] Planar star-shaped oligothiophenes (**27**)[59] with benzo[1,2-*b*:3,4-*b'*:5,6-*b''*]trithiophene as the core were synthesized by Blanchard et al. OFETs based on the thermal-evaporated films of **27b**[60] showed a mobility of 10^{-3} cm^2 V^{-1} s^{-1}.

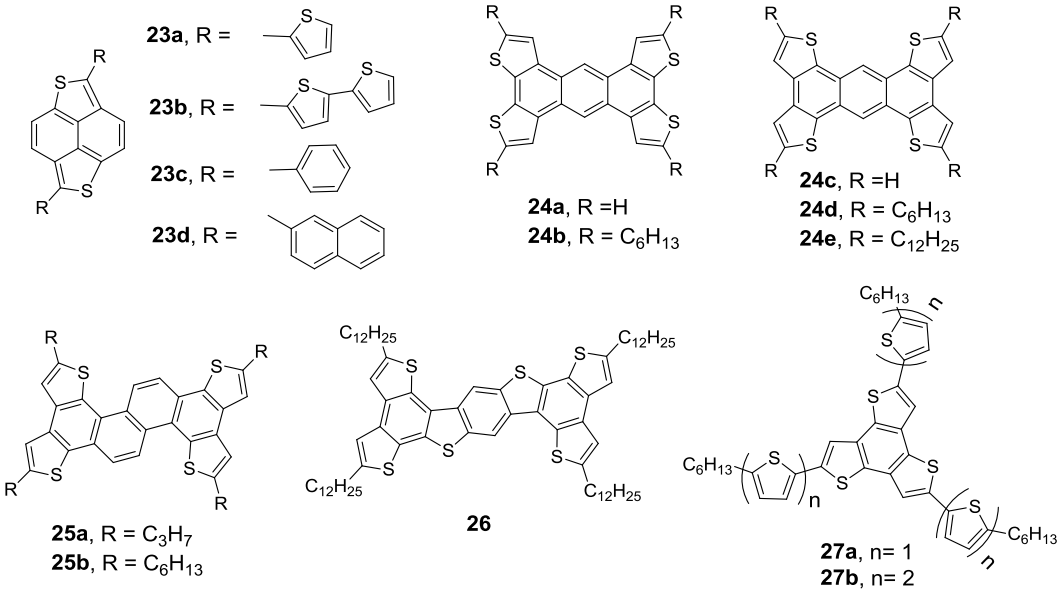

Scheme 1-5. Molecular structures of fused aromatic sulfur-containing compounds

1.2.4 Thiadiazole-fused materials for organic semiconductors

Thiadiazole-fused heterocycle polyaromatics often exhibit short intermolecular S ··N contacts between the thiadiazole rings, which are perpendicular to the π-staking direction due to the polarized S-N bonds. These features are favorable for increasing carrier mobility in molecular crystals. Benzothidiazole (BTz) is an important thiadiazole-based moiety, which is widely applied to organic solar cells as a acceptor component in the donor-acceptor copolymers (**28**). For example, BTz was combined with 9-(heptadecan-9-yl)-9H-carbazole to obtain a copolymer, namely poly[*N*-9′-heptadecanyl-2,7-carbazole-*alt*-5,5-(4′,7′-di-2-thienyl-2′,1′,3′-benzothiadiazole)].[61] The combination of a small band gap with good mechanical and transport properties, led to a power conversion efficiency (PCE) of 3.6 % in the bulk heterojunction (BHJ) solar cells. The BTz was also connected with a donor, dithienosilole (DTS), to form BHJ polymers, and the control solar cells of this polymer showed a higher PCE of 4.6% in the OPV devices.[62] In order to build strong *π*-*π* stracking structures, napptho[1,2-*c*:5,6-*c*']bis[1,2,5]thiadiazole (NTz) was utilized as a acceptor in a copolymer (**29**) for solar cells. NTz, first synthesized by Mataka and co-workers in 1991,[63] was expected to be a strong acceptor with a *π*-extended ring rather than BTz. Thus, the incorporation of NTz into polymer main chain with a donor unit, should lead to a deeper HOMO energy level and a smaller energy bandgap. A NTz-based polymer, PNTz4T, prepared by Takimiya's group, exhibits not only a high

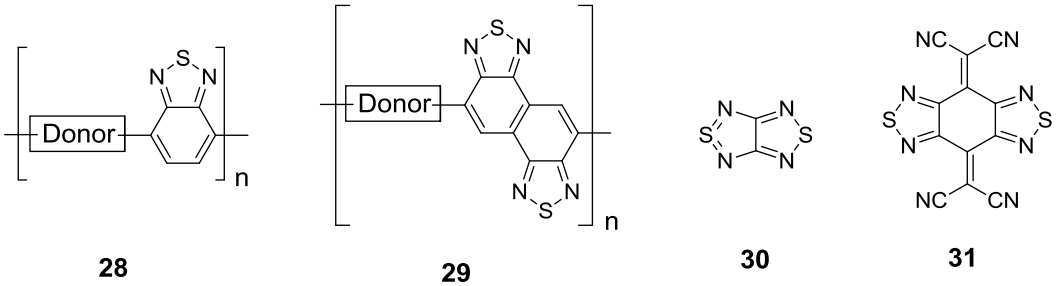

28 **29** **30** **31**

Scheme 1-6. Molecular structures of thiadiazole-fused materials

field-effect mobility of ~0.56 cm^2 V^{-1} s^{-1} but also high photovoltaic properties with a power efficiency of ~6.3%, both of which are significantly high compared to those for a BTz-based polymer, PBTz4T.[64]

[1,2,5]thiadiazolo[3,4-*c*][1,2,5]thiadiazole (**30**), synthesized in 1975,[65] formed long lived radical anion salts with various cations such as alkali metals,[66] cobaltocene[67]. Self-assembling of [$Ru_2(O_2CPh$-*m*-$F_4)$] and BTDA-TCNQ (**31**) produced a charge-transfer system with a 3D structure, which exhibits long-range ferromagnetic order with T_c = 107 K.[68]

1. 3 Organic field effect transistors (OFETs)

Organic field transistors (OFETs) have attracted interest from areas of chemistry, physics, materials, and microelectronics. On the technological side, OFETs are considered to be a key component of organic integrated circuits for use in flexible smart cards, low-cost radio frequency identification tags, and organic active matrix displays.[30a,69] On the scientific side, OFETs also provide an effective means of testing novel organic semiconductors.[24b,49,70] In order to obtain OFETs with high performance, much effort has been devoted to the synthesis of novel π-conjugated molecules and the development of new fabrication techniques.[71]

A typical OFET is composed of a gate electrode, a gate dielectric layer, an organic semiconductor active layer and source drain electrodes. According to the configuration of the FET devices, OFETs can be divided into four types: Bottom gate/bottom contact, Bottom gate/top contact, Top gate/bottom contact, and Top gate/top contact (Fig. 1-1). When a gate voltage is applied, the carriers accumulate near the dielectric layer/organic layer interface and form a conductive channel. Carries were then injected from the source electrode into the organic layer and transported through the channel to the drain electrode.[72] The charge transport process of a p-type active organic layer is shown in Fig. 1-2 (a).

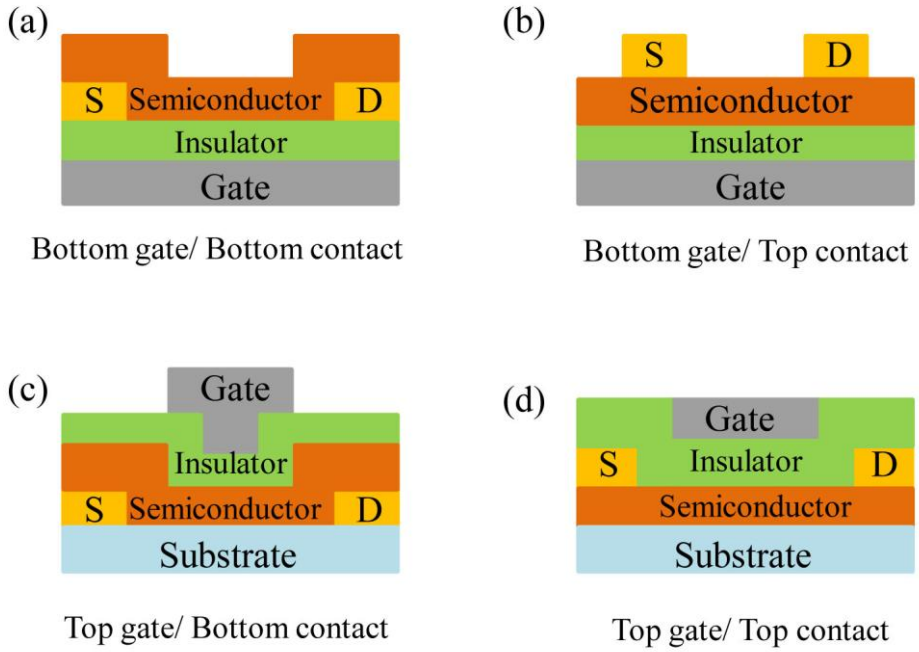

Fig. 1-1. Four types of FETs: Bottom gate/Bottom contact (a), Bottom gate/Top contact (b), Top gate/Bottom contact (c) and Top gate/Top contact.

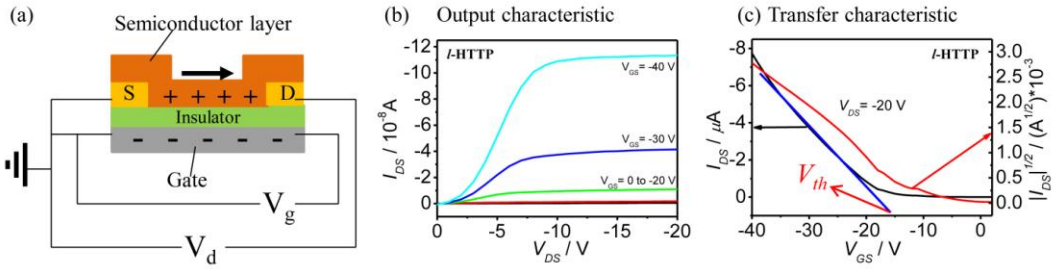

Fig. 1-2. Charge transport of a p-type material (a). Typical I-V characteristics of ***l*-HTTP**-based bottom-gate/bottom-contact p-channel OFET with gate dielectric of 300nm SiO2: output characteristics (b) and transfer characteristics (c). Chart (b) and (c) are adapted from Chapter 2, Page 48.

Typical current-voltage (*I-V*) curves for ***l*-HTTP** p-channel FET with dielectric, SiO_2 substrate are shown in Fig. 1-2 (b) and (c). The output curves show the gate modulation of the source-drain current (I_{DS}). The transfer curves provide more information about the device such as its field-effect mobility (μ), threshold voltage (V_{th}), current on/off ratio (I_{on}/I_{off}) and subthreshold swing (S). According to the common model of OFETs, in the linear regime (at low V_{DS} ($< V_{GS} - V_{th}$)), μ (which has the unit of $cm^2\ V^{-1}\ s^{-1}$) can be calculated from the following equation:

$$I_{DS} = \frac{W}{L} \mu C_i (V_{GS} - V_{th}) V_{DS}$$

The value of μ of the OFETs in the saturation region (at high V_{DS} (> $V_{GS} - V_{th}$)) is given by:

$$I_{DS} = \frac{W}{2L} \mu C_i (V_{GS} - V_{th})^2$$

In this section, the basic principle and calculation of mobility of field effect transistor was introduced. This would be helpful to understand the FET characteristic of the obtained novel materials discussed in chapter 2 and 3.

1.4 Fused polyaromatic molecules containing hetero-atoms for organic electronics

As described above, a large number of organic materials with hetero-atoms such as S and N atoms have been used for organic electronics. In this thesis, two series of materials with hetero-atoms were developed for organic electronics: a series of thiophene-fused phenazine derivatives and a series of thiadiazole-fused aromatic materials with hetero-atoms, S and N atoms.

In chapter 2, the optical and electronic properties of a series of novel thiophene-fused phenazine materials are discussed in terms of the presence of N atoms and the position of S atoms. The redox potentials and the UV-Vis absorption spectra of these derivatives were significantly affected by the positions of the sulfur atoms and the alkyl groups. In comparison with the reported anthrancene analogues, the optical properties of the phenazines are different from those of anthrancene analogues due to the introduction of the nitrogen atoms.

In chapter 3, a series of thiadiazole-fused materials were developed. A thiadiazole ring with a N-S-N moiety having electron-withdrawing group brought strong acceptor ability after fusion of the electron-withdrawing group to the aromatic skeleton. These materials were demonstrated as n-type OFET and stable anion-radical salts, applicable for use in organic electronics and magnetic materials, respectivelty.

In chapter 4, the conclusion of this study, and the promising avenues of future work are described.

References

(1) Akamatu, H.; Inokuchi, H.; Matsunaga, Y. *Nature* **1954**, *173*, 168-169.

(2) (a) Melby, L. R.; Harder, R. J.; Hertler, W. R.; Mahler, W.; Benson, B. E.; Mochel, W. E. *J. Am. Chem. Soc.* **1962**, *84*, 3374-3387; (b) Ferraris, J.; Cowan, D. O.; Walatka, V.; Perlstein, J. H. *J. Am. Chem. Soc.* **1973**, *95*, 948-949.

(3) Kini, A. M.; Geiser, U.; Wang, H. H.; Carlson, K. D.; Williams, J. M.; Kwok, W. K.; Vandervoort, K. G.; Thompson, J. E.; Stupka, D. L.; Jung, D.; Whangbo, M. H. *Inorg. Chem.* **1990**, *29*, 2555-2557.

(4) Shirakawa, H. *Jpn. J. Appl. Phys., Part 1*. **1983**, *22*, 473-478.

(5) Lin, Y. Y.; Gundlach, D. J.; Nelson, S. F.; Jackson, T. N. *IEEE Electron Device Lett.* **1997**, *18*, 606-608.

(6) Okamoto, H.; Kawasaki, N.; Kaji, Y.; Kubozono, Y.; Fujiwara, A.; Yamaji, M. *J. Am. Chem. Soc.* **2008**, *130*, 10470-10471.

(7) Sirringhaus, H.; Brown, P. J.; Friend, R. H.; Nielsen, M. M.; Bechgaard, K.; Langeveld-Voss, B. M. W.; Spiering, A. J. H.; Janssen, R. A. J.; Meijer, E. W.; Herwig, P.; de Leeuw, D. M. *Nature* **1999**, *401*, 685-688.

(8) Hasegawa, T.; Takeya, J. *Sci. Technol. Adv. Mat.* **2009**, *10*.

(9) (a) Bechgaard, K.; Jacobsen, C. S.; Mortenson, K.; Pedersen, H. J.; Thorup, N. *Solid State Commun.* **1980**, *33*, 1119-1125; (b) Tanigaki, K.; Ebbesen, T. W.; Saito, S.; Mizurki, J. S.; Murthy, Y.; Kuroshima, S. *Nature (London, U. K.)* **1991**, *29*, 222.

(10) Heath, J. R.; Ratner, M. A. *Phys. Today* **2003**, *56*, 43-49.

(11) Chiang, C. K.; Fincher, C. R.; Park, Y. W.; Heeger, A. J.; Shirakawa, H.; Louis, E. J.; Gau, S. C.; Macdiarmid, A. G. *Phys. Rev. Lett.* **1977**, *39*, 1098-1101.

(12) Aleshin, A. N.; Lee, J. Y.; Chu, S. W.; Kim, J. S.; Park, Y. W. *Appl. Phys. Lett.* **2004**, *84*, 5383-5385.

(13) Gundlach, D. J.; Nichols, J. A.; Zhou, L.; Jackson, T. N. *Appl. Phys. Lett.* **2002**, *80*, 2925-2927.

(14) Reese, C.; Chung, W. J.; Ling, M. M.; Roberts, M.; Bao, Z. N. *Appl. Phys. Lett.*

2006, *89*, 201108.

(15) Lin, Y. Y.; Gundlach, D. J.; Nelson, S. F.; Jackson, T. N. *IEEE Electron Device Lett.* **1997**, *18*, 606-608.

(16) Kelley, T. W.; Muyres, D. V.; Baude, P. F.; Smith, T. P.; Jones, T. D. *Mater. Res. Soc. Symp. Proc.* **2003**, *771*, 169-179.

(17) Wang, C. L.; Dong, H. L.; Hu, W. P.; Liu, Y. Q.; Zhu, D. B. *Chem. Rev.* **2012**, *112*, 2208-2267.

(18) De, A.; Ghosh, R.; Roychowdhury, S.; Roychowdhury, P. *Acta Crystallogr C* **1985**, *41*, 907-909.

(19) (a) Kawasaki, N.; Ohta, Y.; Kubozono, Y.; Konishi, A.; Fujiwara, A. *Appl. Phys. Lett.* **2008**, *92*, 163307; (b) Lee, X.; Sugawara, Y.; Ito, A.; Oikawa, S.; Kawasaki, N.; Kaji, Y.; Mitsuhashi, R.; Okamoto, H.; Fujiwara, A.; Omote, K.; Kambe, T.; Ikeda, N.; Kubozono, Y. *Org. Electron.* **2010**, *11*, 1394-1398.

(20) Kawai, N.; Eguchi, R.; Goto, H.; Akaike, K.; Kaji, Y.; Kambe, T.; Fujiwara, A.; Kubozono, Y. *J. Phys. Chem. C* **2012**, *116*, 7983-7988.

(21) Mitsuhashi, R.; Suzuki, Y.; Yamanari, Y.; Mitamura, H.; Kambe, T.; Ikeda, N.; Okamoto, H.; Fujiwara, A.; Yamaji, M.; Kawasaki, N.; Maniwa, Y.; Kubozono, Y. *Nature* **2010**, *464*, 76-79.

(22) Podzorov, V.; Sysoev, S. E.; Loginova, E.; Pudalov, V. M.; Gershenson, M. E. *Appl. Phys. Lett.* **2003**, *83*, 3504-3506.

(23) (a) Goldmann, C.; Haas, S.; Krellner, C.; Pernstich, K. P.; Gundlach, D. J.; Batlogg, B. *J. Appl. Phys.* **2004**, *96*, 2080-2086; (b) Takeya, J.; Nishikawa, T.; Takenobu, T.; Kobayashi, S.; Iwasa, Y.; Mitani, T.; Goldmann, C.; Krellner, C.; Batlogg, B. *Appl. Phys. Lett.* **2004**, *85*, 5078-5080.

(24) (a) Menard, E.; Podzorov, V.; Hur, S. H.; Gaur, A.; Gershenson, M. E.; Rogers, J. A. *Adv. Mater.* **2004**, *16*, 2097-2101; (b) Sundar, V. C.; Zaumseil, J.; Podzorov, V.; Menard, E.; Willett, R. L.; Someya, T.; Gershenson, M. E.; Rogers, J. A. *Science* **2004**, *303*, 1644-1646; (c) Takeya, J.; Kato, J.; Hara, K.; Yamagishi, M.; Hirahara, R.; Yamada, K.; Nakazawa, Y.; Ikehata, S.; Tsukagoshi, K.; Aoyagi, Y.; Takenobu, T.; Iwasa, Y. *Phys. Rev. Lett.* **2007**, *98*,

196804; (d) Takeya, J.; Yamagishi, M.; Tominari, Y.; Hirahara, R.; Nakazawa, Y.; Nishikawa, T.; Kawase, T.; Shimoda, T.; Ogawa, S. *Appl. Phys. Lett.* **2007**, *90*, 102120.

(25) Bao, Z.; Lovinger, A. J.; Dodabalapur, A. *Appl. Phys. Lett.* **1996**, *69*, 3066-3068.

(26) (a) Tang, Q. X.; Li, H. X.; He, M.; Hu, W. P.; Liu, C. M.; Chen, K. Q.; Wang, C.; Liu, Y. Q.; Zhu, D. B. *Adv. Mater.* **2006**, *18*, 65-68; (b) Tang, Q. X.; Li, H. X.; Song, Y. B.; Xu, W.; Hu, W. P.; Jiang, L.; Liu, Y. Q.; Wang, X. K.; Zhu, D. B. *Adv. Mater.* **2006**, *18*, 3010-3014.

(27) Mizuguchi, J.; Rihs, G.; Karfunkel, H. R. *J. Phys. Chem.* **1995**, *19*, 16217-16227.

(28) Li, L. Q.; Tang, Q. X.; Li, H. X.; Yang, X. D.; Hu, W. P.; Song, Y. B.; Shuai, Z. G.; Xu, W.; Liu, Y. Q.; Zhu, D. B. *Adv. Mater.* **2007**, *19*, 2613-2617.

(29) (a) Wang, H. B.; Song, D.; Yang, J. L.; Yu, B.; Geng, Y. H.; Yan, D. H. *Appl. Phys. Lett.* **2007**, *90*, 253510-253512; (b) Yu, X. J.; Xu, J. B.; Cheung, W. Y.; Ke, N. *J. Appl. Phys.* **2007**, *102*, 103711-103716.

(30) (a) Baude, P. F.; Ender, D. A.; Haase, M. A.; Kelley, T. W.; Muyres, D. V.; Theiss, S. D. *Appl. Phys. Lett.* **2003**, *82*, 3964-3966; (b) Gawrys, P.; Boudinet, D.; Zagorska, M.; Djurado, D.; Verilhac, J. M.; Horowitz, G.; Pecaud, J.; Pouget, S.; Pron, A. *Synth. Met.* **2009**, *159*, 1478-1485; (c) Katz, H. E.; Johnson, J.; Lovinger, A. J.; Li, W. J. *J. Am. Chem. Soc.* **2000**, *122*, 7787-7792; (d) Katz, H. E.; Lovinger, A. J.; Johnson, J.; Kloc, C.; Siegrist, T.; Li, W.; Lin, Y. Y.; Dodabalapur, A. *Nature* **2000**, *404*, 478-481; (e) Shukla, D.; Nelson, S. F.; Freeman, D. C.; Rajeswaran, M.; Ahearn, W. G.; Meyer, D. M.; Carey, J. T. *Chem. Mater.* **2008**, *20*, 7486-7491.

(31) (a) Chen, Z. J.; Debije, M. G.; Debaerdemaeker, T.; Osswald, P.; Wurthner, F. *ChemPhysChem* **2004**, *5*, 137-140; (b) Chesterfield, R. J.; McKeen, J. C.; Newman, C. R.; Ewbank, P. C.; da Silva, D. A.; Bredas, J. L.; Miller, L. L.; Mann, K. R.; Frisbie, C. D. *J. Phys. Chem. B* **2004**, *108*, 19281-19292; (c) Jones, B. A.; Facchetti, A.; Wasielewski, M. R.; Marks, T. J. *J. Am. Chem. Soc.*

2007, *129*, 15259-15278; (d) Ling, M. M.; Erk, P.; Gomez, M.; Koenemann, M.; Locklin, J.; Bao, Z. N. *Adv. Mater.* **2007**, *19*, 1123-1127; (e) Malenfant, P. R. L.; Dimitrakopoulos, C. D.; Gelorme, J. D.; Kosbar, L. L.; Graham, T. O.; Curioni, A.; Andreoni, W. *Appl. Phys. Lett.* **2002**, *80*, 2517-2519; (f) Schmidt, R.; Ling, M. M.; Oh, J. H.; Winkler, M.; Konemann, M.; Bao, Z. N.; Wurthner, F. *Adv. Mater.* **2007**, *19*, 3692-3695; (g) Schmidt, R.; Oh, J. H.; Sun, Y. S.; Deppisch, M.; Krause, A. M.; Radacki, K.; Braunschweig, H.; Konemann, M.; Erk, P.; Bao, Z. A.; Wurthner, F. *J. Am. Chem. Soc.* **2009**, *131*, 6215-6228.

(32) (a) Bendikov, M.; Wudl, F.; Perepichka, D. F. *Chem Rev* **2004**, *104*, 4891-4945; (b) Mas-Torrent, M.; Rovira, C. *Chem. Soc. Rev.* **2008**, *37*, 827-838.

(33) Che, C. M.; Xiang, H. F.; Chui, S. S. Y.; Xu, Z. X.; Roy, V. A. L.; Yan, J. J.; Fu, W. F.; Lai, P. T.; Williams, I. D. *Chem-Asian J.* **2008**, *3*, 1092-1103.

(34) Garnier, F.; Yassar, A.; Hajlaoui, R.; Horowitz, G.; Deloffre, F.; Servet, B.; Ries, S.; Alnot, P. *J. Am. Chem. Soc.* **1993**, *115*, 8716-8721.

(35) Garnier, F.; Horowitz, G.; Peng, X. Z.; Fichou, D. *Synth. Met.* **1991**, *45*, 163-171.

(36) (a) Halik, M.; Klauk, H.; Zschieschang, U.; Schmid, G.; Ponomarenko, S.; Kirchmeyer, S.; Weber, W. *Adv. Mater.* **2003**, *15*, 917-922; (b) Horowitz, G.; Hajlaoui, M. E. *Adv. Mater.* **2000**, *12*, 1046-1050.

(37) Deman, A. L.; Tardy, J.; Nicolas, Y.; Blanchard, P.; Roncali, J. *Synth. Met.* **2004**, *146*, 365-371.

(38) Garnier, F.; Hajlaoui, R.; El Kassmi, A.; Horowitz, G.; Laigre, L.; Porzio, W.; Armanini, M.; Provasoli, F. *Chem. Mater.* **1998**, *10*, 3334-3339.

(39) (a) Zen, A.; Bilge, A.; Galbrecht, F.; Alle, R.; Meerholz, K.; Grenzer, J.; Neher, D.; Scherf, U.; Farrell, T. *J. Am. Chem. Soc.* **2006**, *128*, 3914-3915; (b) Zen, A.; Pingel, P.; Jaiser, F.; Neher, D.; Grenzer, J.; Zhuang, W.; Rabe, J. P.; Bilge, A.; Galbrecht, F.; Nehls, B. S.; Farrell, T.; Scherf, U.; Abellon, R. D.; Grozema, F. C.; Siebbeles, L. D. A. *Chem. Mater.* **2007**, *19*, 1267-1276; (c) Zen, A.; Pingel, P.; Neher, D.; Scherf, U. *Phys. Status Solidi A* **2008**, *205*, 440-448.

(40) Kreyes, A.; Ellinger, S.; Landfester, K.; Defaux, M.; Ivanov, D. A.; Elschner, A.;

Meyer-Friedrichsen, T.; Ziener, U. *Chem. Mater.* **2010**, *22*, 2079-2092.

(41) (a) Lengyel, O.; Hardeman, W. M.; Wondergem, H. J.; de Leeuw, D. M.; van Breemen, A. J. J. M.; Resel, R. *Adv. Mater.* **2006**, *18*, 896-899; (b) van Breemen, A. J. J. M.; Herwig, P. T.; Chlon, C. H. T.; Sweelssen, J.; Schoo, H. F. M.; Setayesh, S.; Hardeman, W. M.; Martin, C. A.; de Leeuw, D. M.; Valeton, J. J. P.; Bastiaansen, C. W. M.; Broer, D. J.; Popa-Merticaru, A. R.; Meskers, S. C. J. *J. Am. Chem. Soc.* **2006**, *128*, 2336-2345.

(42) Peet, J.; Kim, J. Y.; Coates, N. E.; Ma, W. L.; Moses, D.; Heeger, A. J.; Bazan, G. C. *Nat. Mater.* **2007**, *6*, 497-500.

(43) Kim, J. Y.; Lee, K.; Coates, N. E.; Moses, D.; Nguyen, T. Q.; Dante, M.; Heeger, A. J. *Science* **2007**, *317*, 222-225.

(44) Marrocchi, A.; Lanari, D.; Facchetti, A.; Vaccaro, L. *Energy & Environmental Science* **2012**, *5*, 8457-8474.

(45) Xiao, K.; Liu, Y. Q.; Qi, T.; Zhang, W.; Wang, F.; Gao, J. H.; Qiu, W. F.; Ma, Y. Q.; Cui, G. L.; Chen, S. Y.; Zhan, X. W.; Yu, G.; Qin, J. G.; Hu, W. P.; Zhu, D. B. *J. Am. Chem. Soc.* **2005**, *127*, 13281-13286.

(46) Liu, Y.; Wang, Y.; Wu, W. P.; Liu, Y. Q.; Xi, H. X.; Wang, L. M.; Qiu, W. F.; Lu, K.; Du, C. Y.; Yu, G. *Adv. Funct. Mater.* **2009**, *19*, 772-778.

(47) Zhang, X. N.; Cote, A. P.; Matzger, A. J. *J. Am. Chem. Soc.* **2005**, *127*, 10502-10503.

(48) Okamoto, T.; Kudoh, K.; Wakamiya, A.; Yamaguchi, S. *Chem-Eur J* **2007**, *13*, 548-556.

(49) Ebata, H.; Izawa, T.; Miyazaki, E.; Takimiya, K.; Ikeda, M.; Kuwabara, H.; Yui, T. *J. Am. Chem. Soc.* **2007**, *129*, 15732-15733.

(50) Niimi, K.; Shinamura, S.; Osaka, I.; Miyazaki, E.; Takimiya, K. *J. Am. Chem. Soc.* **2011**, *133*, 8732-8739.

(51) Kang, M. J.; Doi, I.; Mori, H.; Miyazaki, E.; Takimiya, K.; Ikeda, M.; Kuwabara, H. *Adv. Mater.* **2011**, *23*, 1222-1225.

(52) Nakayama, K.; Hirose, Y.; Soeda, J.; Yoshizumi, M.; Uemura, T.; Uno, M.; Li, W. Y.; Kang, M. J.; Yamagishi, M.; Okada, Y.; Miyazaki, E.; Nakazawa, Y.;

Nakao, A.; Takimiya, K.; Takeya, J. *Adv. Mater.* **2011**, *23*, 1626-1629.

(53) (a) Tang, M. L.; Mannsfeld, S. C. B.; Sun, Y. S.; Becerril, H. A.; Bao, Z. N. *J. Am. Chem. Soc.* **2009**, *131*, 882-883; (b) Tang, M. L.; Okamoto, T.; Bao, Z. N. *J. Am. Chem. Soc.* **2006**, *128*, 16002-16003; (c) Tang, M. L.; Reichardt, A. D.; Okamoto, T.; Miyaki, N.; Bao, Z. A. *Adv. Funct. Mater.* **2008**, *18*, 1579-1585; (d) Valiyev, F.; Hu, W. S.; Chen, H. Y.; Kuo, M. Y.; Chao, I.; Tao, Y. T. *Chem. Mater.* **2007**, *19*, 3018-3026.

(54) Takimiya, K.; Kunugi, Y.; Toyoshima, Y.; Otsubo, T. *J. Am. Chem. Soc.* **2005**, *127*, 3605-3612.

(55) (a) Brusso, J. L.; Hirst, O. D.; Dadvand, A.; Ganesan, S.; Cicoira, F.; Robertson, C. M.; Oakley, R. T.; Rosei, F.; Perepichka, D. F. *Chem. Mater.* **2008**, *20*, 2484-2494; (b) Liu, W. J.; Zhou, Y.; Ma, Y. G.; Cao, Y.; Wang, J.; Pei, J. *Org. Lett.* **2007**, *9*, 4187-4190.

(56) Wang, J. Y.; Zhou, Y.; Yan, J.; Ding, L.; Ma, Y. G.; Cao, Y.; Wang, J.; Pei, J. *Chem. Mater.* **2009**, *21*, 2595-2597.

(57) Zhou, Y.; Liu, W. J.; Ma, Y. G.; Wang, H. L.; Qi, L. M.; Cao, Y.; Wang, J.; Pei, J. *J. Am. Chem. Soc.* **2007**, *129*, 12386-12387.

(58) Zhou, Y.; Lei, T.; Wang, L.; Pei, J.; Cao, Y.; Wang, J. *Adv. Mater.* **2010**, *22*, 1484-1487.

(59) Nicolas, Y.; Blanchard, P.; Levillain, E.; Allain, M.; Mercier, N.; Roncali, J. *Org. Lett.* **2004**, *6*, 273-276.

(60) Roncali, J.; Leriche, P.; Cravino, A. *Adv. Mater.* **2007**, *19*, 2045-2060.

(61) Blouin, N.; Michaud, A.; Leclerc, M. *Adv. Mater.* **2007**, *19*, 2295-2300.

(62) Beaujuge, P. M.; Tsao, H. N.; Hansen, M. R.; Amb, C. M.; Risko, C.; Subbiah, J.; Choudhury, K. R.; Mavrinskiy, A.; Pisula, W.; Bredas, J. L.; So, F.; Mullen, K.; Reynods, J. R. *J. Am. Chem. Soc.* **2012**, *134*, 8944-8957.

(63) Mataka, S.; Takahashi, K.; Ikezaki, Y.; Hatta, T.; Torii, A.; Tashiro, M. *Bull. Chem. Soc. Jpn.* **1991**, *64*, 68-73.

(64) Osaka, I.; Shimawaki, M.; Mori, H.; Doi, I.; Miyazaki, E.; Koganezawa, T.; Takimiya, K. *J. Am. Chem. Soc.* **2012**, *134*, 3498-3507.

(65) Komin, A. P.; Street, R. W.; Carmack, M. *J. Org. Chem.* **1975**, *40*, 2749-2752.

(66) (a) Ikorskii, V. N.; Irtegova, I. G.; Lork, E.; Makarov, A. Y.; Mews, R.; Ovcharenko, V. I.; Zibarev, A. V. *Eur. J. Inorg. Chem.* **2006**, 3061-3067; (b) Makarov, A. Y.; Irtegova, I. G.; Vasilieva, N. V.; Bagryanskaya, I. Y.; Borrmann, T.; Gatilov, Y. V.; Lork, E.; Mews, R.; Stohrer, W. D.; Zibarev, A. V. *Inorg. Chem.* **2005**, *44*, 7194-7199.

(67) Konchenko, S. N.; Gritsan, N. P.; Lonchakov, A. V.; Irtegova, I. G.; Mews, R.; Ovcharenko, V. I.; Radius, U.; Zibarev, A. V. *Eur. J. Inorg. Chem.* **2008**, 3833-3838.

(68) Motokawa, N.; Miyasaka, H.; Yamashita, M.; Dunbar, K. R. *Angew. Chem. Int. Edit.* **2008**, *47*, 7760-7763.

(69) (a) Crone, B.; Dodabalapur, A.; Lin, Y. Y.; Filas, R. W.; Bao, Z.; LaDuca, A.; Sarpeshkar, R.; Katz, H. E.; Li, W. *Nature* **2000**, *403*, 521-523; (b) Rogers, J. A.; Bao, Z.; Baldwin, K.; Dodabalapur, A.; Crone, B.; Raju, V. R.; Kuck, V.; Katz, H.; Amundson, K.; Ewing, J.; Drzaic, P. *Proc. Natl. Acad. Sci. U. S. A.* **2001**, *98*, 4835-4840; (c) Someya, T.; Sekitani, T.; Iba, S.; Kato, Y.; Kawaguchi, H.; Sakurai, T. *Proc. Natl. Acad. Sci. U. S. A.* **2004**, *101*, 9966-9970.

(70) (a) Alves, H.; Molinari, A. S.; Xie, H. X.; Morpurgo, A. F. *Nat. Mater.* **2008**, *7*, 574-580; (b) Yan, H.; Chen, Z. H.; Zheng, Y.; Newman, C.; Quinn, J. R.; Dotz, F.; Kastler, M.; Facchetti, A. *Nature* **2009**, *457*, 679-U671.

(71) Guo, Y. L.; Yu, G.; Liu, Y. Q. *Adv. Mater.* **2010**, *22*, 4427-4447.

(72) (a) Di, C. A.; Liu, Y. Q.; Yu, G.; Zhu, D. B. *Acc. Chem. Res.* **2009**, *42*, 1573-1583; (b) Egginger, M.; Bauer, S.; Schwodiauer, R.; Neugebauer, H.; Sariciftci, N. S. *Monatshefte Fur Chemie* **2009**, *140*, 735-750; (c) Facchetti, A.; Yoon, M. H.; Marks, T. J. *Adv. Mater.* **2005**, *17*, 1705-1725; (d) Newman, C. R.; Frisbie, C. D.; da Silva, D. A.; Bredas, J. L.; Ewbank, P. C.; Mann, K. R. *Chem. Mater.* **2004**, *16*, 4436-4451; (e) Zaumseil, J.; Sirringhaus, H. *Chem. Rev.* **2007**, *107*, 1296-1323.

Chapter 2 Syntheses, optical properties and charge transport characteristics of a series of novel thiophene-fused phenazines

2.1 Introduction

Organic π-conjugated materials have attracted considerable attention in recent years due to their potential application in organic electronics such as organic light emitting diodes (OLEDs),[1] organic photovoltaics (OPVs)[2] and organic field transistors (OFETs).[3] Among them, thiophene-fused polyaromatic compounds have been interested since the thienyl S ··S contacts can contribute to the intermolecular charge transport in the solid state, as well as the π-π stacking. Some thiophene-fused polyaromatic compounds have shown high-performance in OFET devices, rivaling that of amorphous silicon in terms of carrier mobility. Diacene-fused thieno[3,2-*b*]-thiophenes (up to 12 cm^2 V^{-1} s^{-1} of field-effect mobility)[4]; 2,6-diaryl-NDTs (up to 0.1 cm^2 V^{-1} s^{-1} of field-effect mobility)[5] and2,7-dialkyl[1]benzothieno[3,2-*b*][1]benzothiophenes (C_n-BTBTs) (up to 2.7 cm^2 V^{-1} s^{-1} of field-effect mobility)[6] are some representative examples.

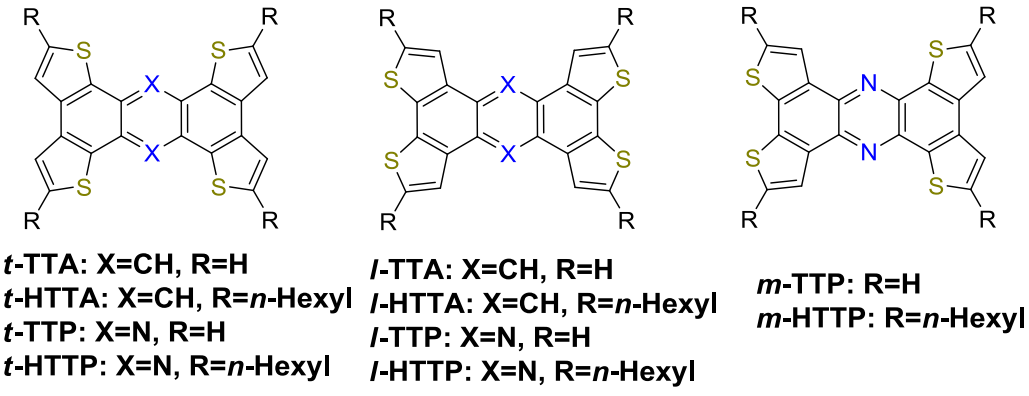

Scheme 2-1**.** Chemical structure of phenazine derivatives(X = N) and anthracene analogues(X = CH).

---

* This chapter is reproduced by permission of The Royal Society of Chemistry.[7]

However, the preparation of such molecules usually involves many steps, and often utilizes toxic organometallic chemicals. In the present work, a series of thiophene-fused phenazines (***t*-TTP**, ***l*-TTP** and ***m*-TTP**) and their alkyl-substituted derivatives (Scheme 2-1) were designed and synthesized. All of these derivatives were obtained by a key reaction (Scheme 2-2), a condensation reaction between a diketone and a diamine, itself derived from the diketone.[8] The physical properties, crystal structures and transport properties of these molecules were compared with each other in terms of the positions of sulfur atoms, and the effect of the nitrogen atoms in the central aromatic ring is discussed in comparison with the anthracene analogues reported by Perepichka[9] and Pei[10] (Scheme 2-1).

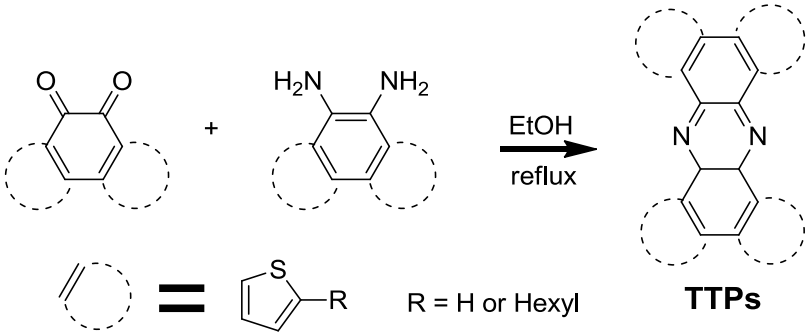

Scheme 2-2**.** Key reaction for thiophene-fused phenazines.

2.2 Results and discussion

2.2.1 Synthesis

The synthetic route to the tetrathienophenazines (***t*-TTP**, ***l*-TTP**, ***m*-TTP, *t*-HTTP**, ***l*-HTTP** and ***m*-HTTP**) is outlined in Scheme 2-3. The phenazine skeleton was formed by a condensation reaction between a diketone and a diamine.[11] For example, ***t*-TTP** was obtained by refluxing the diketone **1a** and the diamine **4a** in ethanol in 79% yield. Diamine **4a** was prepared from dioxime **3a** by reduction with stannous chloride in 67% yield, and dioxime **3a** can be obtained from **1a** by reaction with hydroxylamine hydrochloride in nearly quantitative yield. Diketones **1a** and **2a** were prepared in accordance with a literature.[12] Hexylated diketones **1b** and **2b** were synthesized from

hexyl thiophene, as shown in Scheme 2-4. The unsubstituted derivatives (***t*-TTP**, ***l*-TTP** and ***m*-TTP**) showed poor solubility in common organic solvents such as toluene, dichloromethane and chloroform, while the solubility was much improved by substituting the hexyl groups at the α-position of the fused thiophene rings (***t*-HTTP**, ***l*-HTTP** and ***m*-HTTP**).

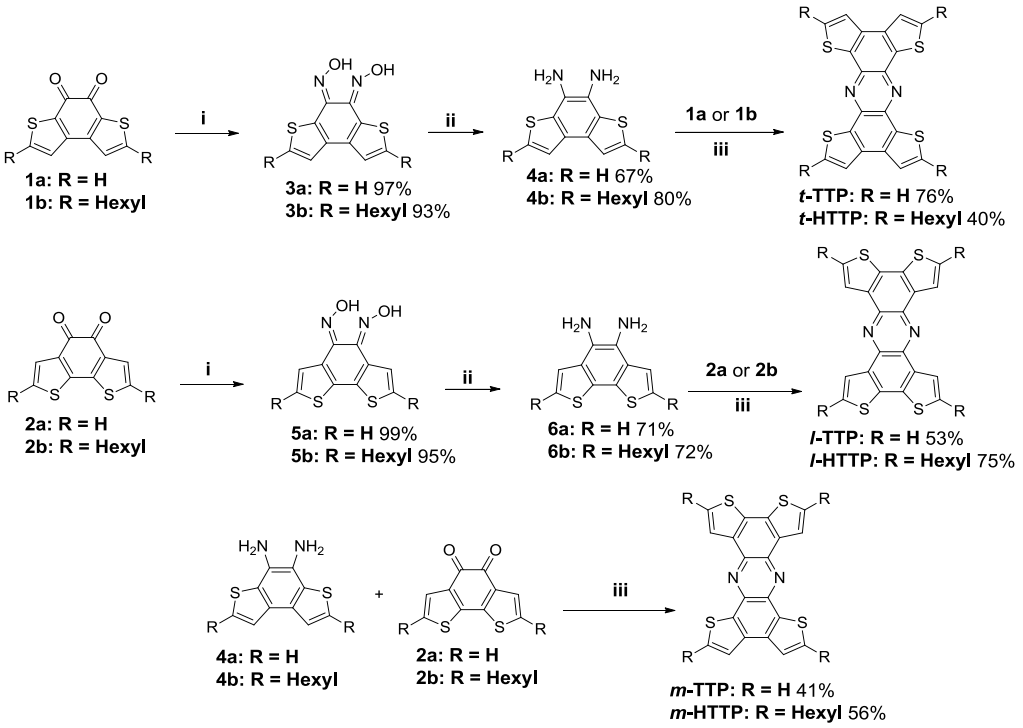

Reagents and conditions: (i) NH_2OH HCl, Pyridine/EtOH, 90 ^oC; (ii) $SnCl_2$, HCl(con.), EtOH, 0^oC ~ RT; (iii) EtOH, reflux.

Scheme 2-3**.** Synthesis of thiophene-fused phanazines.

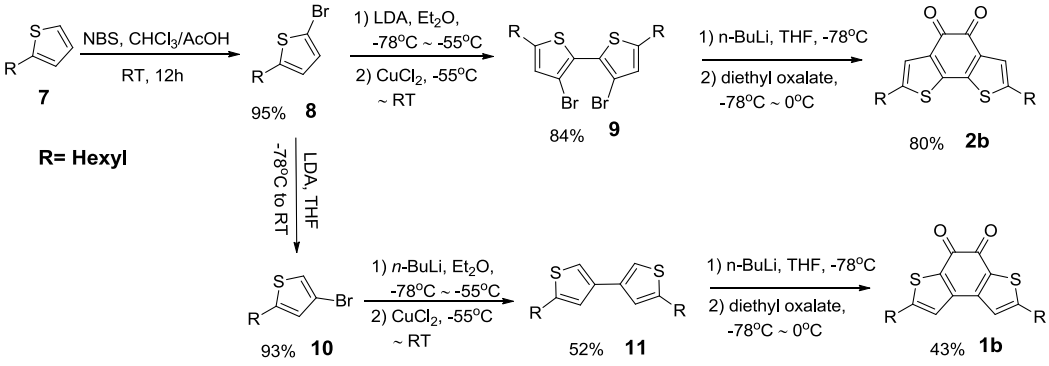

Scheme 2-4**.** Synthesis of diketone compounds

In conclusion, a series of thiophene-fused phenazines were synthesized in reasonable

yields by a simple condensation reaction using only two types of diketones (**1a, 1b, 2a** and **2b**) as starting materials. Furthermore, both symmetric and asymmetric molecules can be prepared by this method, while the corresponding anthracene analogues require different synthetic routes for each molecule.[9] Recently, Reynolds et al.[13] also reported the synthesis of tetrathieno[3,2-a:2',3'-c:3",2"-h:2'",3'"-j]phenazine (***l*-TTP**) by a condensation reaction between a diketone and a diamine. This method could be utilized widely for constructing fused polyaromatic compounds.

2.2.2 Electrochemical properties

The electrochemical properties of the newly synthesized molecules were investigated by cyclic voltammetry (CV). The unsubstituted tetrathienophenazine derivatives did not show any redox peaks within the electrochemical window of tetrabutylammonium hexafluorophosphate ((n-Bu_4N)PF_6) in dichloromethane (DCM). On the other hand, thin films of these molecules deposited on an ITO electrode showed gradually increasing redox waves upon cycling (Fig. 2-1). This behavior resembles the redox properties of the corresponding anthracene analogues, and can be explained as the formation of small amounts of the radical cation species, which is followed by the polymerization at the α-position.[9] However, the alkyl-substituted derivatives showed reproducible cyclic voltammograms with two oxidation peaks, although the corresponding reduction peaks were not observed (Fig. 2-2). From these redox potentials (1.06 V, 0.83 V and 1.21 V vs. Fc/Fc^+ for ***l*-HTTP**, ***m*-HTTP** and ***t*-HTTP**, respectively), the HOMO levels of these molecules were estimated to be -6.2 eV, -5.9 eV and -6.3 eV for ***l*-HTTP**, ***m*-HTTP** and ***t*-HTTP,** respectively.[14] These values indicate that these phenazine derivatives are weaker donors in comparison with the corresponding tetrathienoanthrancene analogues[9] (-5.9 eV and -6.0 eV for ***l*-HTTA** and ***t*-HTTA**, respectively).

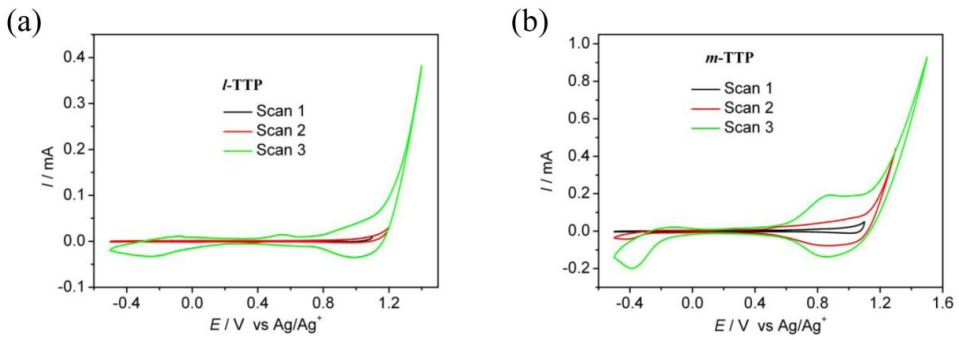

Fig. 2-1**.** Cyclic voltammograms (scan rate 100 mV s^{-1}) of 100nm thin film of ***l*-TTP** and ***m*-TTP** on ITO recorded in DCM solution containing (*n*-Bu_4N)PF_6 (0.1M) as electrolyte. ITO and a Pt electrode were used for the working electrode and the counter electrode, respectively. Potentials referenced to Ag/Ag^+.

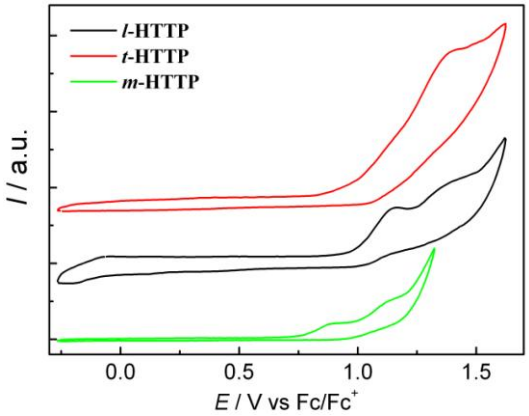

Fig. 2-2**.** Cyclic voltammograms (scan rate 100 mV s^{-1}) of ***l*-HTTP**, ***t*-HTTP** and ***m*-HTTP** recorded in DCM solution containing (*n*-Bu_4N)PF_6 (0.1M) as electrolyte. A glassy carbon electrode and a Pt electrode were used for the working electrode and the counter electrode, respectively. Potentials referenced to Fc/Fc^+.

2.2.3 Optical properties

The UV-vis absorption spectra of the tetrathienophenazine derivatives in $CHCl_3$ are shown in Fig. 2-3, and their λ_{max} are summarized in Table 2-1. In all cases, two strong absorption bands are observed; one absorption band lies around 310 nm for all derivatives, while the other absorption band lies between 400 nm and 490 nm, depending on structure. Introduction of alkyl chains at the α-positions of the fused thiophenes results in a bathochromic shift (3~20 nm) of the λ_{max} values in comparison with their unsubstituted derivatives (Fig. 2-3). The λ_{max} of the unsubstituted derivatives follows the progression ***l*-TTP** > ***m*-TTP** > ***t*-TTP**, and this tendency of

absorption bands was also maintained in the corresponding alkyl-substituted derivatives (Fig. 2-3). These features in the absorption spectra were well reproduced by time-dependent Density Functional Theory (TD-DFT) calculations as discussed later.[15]

The three unsubstituted derivatives (***l*-TTP**, ***m*-TTP** and ***t*-TTP**) showed light-blue fluorescence (λ_{max}^{fl}: around 480 nm) in chloroform while ***t*-HTTP** showed green fluorescence (λ_{max}^{fl}: 501 nm), and both ***m*-HTTP** and ***l*-HTTP** showed yellow fluorescence (λ_{max}^{fl}: around 530 nm). Fig. 2-4 shows the fluorescence spectra of these derivatives and the maximum emissions are listed in Table 2-1. Introduction of the alkyl-chains also caused a red shift in the fluorescence peaks. The Stokes shifts of each material are 0.46 eV, 0.25 eV and 0.07 eV for ***l*-TTP**, ***m*-TTP**, and ***t*-TTP**, respectively, and a decrease in the Stokes shifts was also observed in the alkyl-substituted derivatives (Table 2-1). The fluorescence absolute quantum yields (Φ_f) of these materials were in the range of 0.02 ~ 0.19, as listed in Table 2-1.

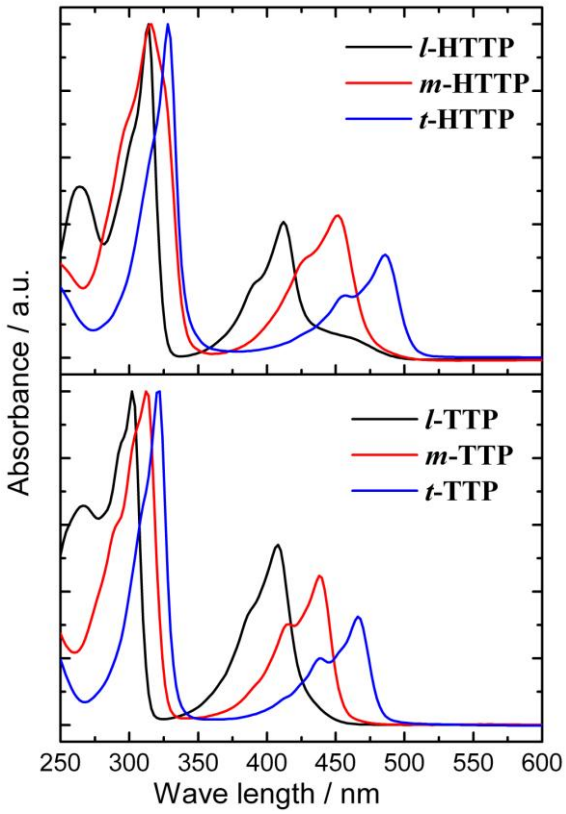

Fig. 2-3**.** Comparison of the UV-Vis spectra of thiophene-fused phenazines in $CHCl_3$ solution.

Table 2-1. Electrochemical,[a] and Optical Properties of Thiophene-fused Phenazines, compared to theoretical values.

	***l*-TTP**	***m*-TTP**	***t*-TTP**	***l*-HTTP**	***m*-HTTP**	***t*-HTTP**	***l*-TTA**[f]	***t*-TTA**[f]
$E_{1/2}^{exp}$ **(V)** [a]	---	---	---	1.06	0.83	1.21	---	---
E_{HOMO}^{exp} **(eV)** [b]	---	---	---	-6.21	-5.93	-6.33	-6.22	-6.69
E_{HOMO}^{calcd}	-5.60	-5.64	-5.68	-5.19	-5.21	-5.32	-5.18	-5.23
E_{LUMO}^{calcd}	-2.27	-2.33	-2.39	-2.04	-1.92	-2.11	---	---
E_{g}^{calcd} **(eV)** [c]	3.33	3.31	3.29	3.15	3.29	3.21	3.52	3.50
λ_{max}^{abs} **(nm)** [d]	408	439	467	411	451	486	379	418
λ_{max}^{abs} **(nm)** [d]	375	404	432	379	414	444	---	---
λ_{max}^{fl} **(nm)** [d]	480	481	479	526	534	501	398	422
Φ_f [e]	0.02	0.02	0.19	0.15	0.05	0.18	0.17	0.32
Stokes shift (eV) [d]	0.46	0.25	0.07	0.66	0.43	0.07	0.16	0.03

[a] Measured in DCM, (n-Bu_4N)PF_6 (0.1M) as supporting electrolyte, and referenced to Fc/Fc^+. [b] Estimated from the CV measurement according to the empirical formula $E_{HOMO} = -(1.4 \pm 0.1) \times qV_{CV} - (4.6 \pm 0.08)$ eV from reference 13. [c] B3LYP/6-31G(d). [d] Measured in $CHCl_3$. [e] Absolute fluorescence quantum yields were determined with a Hamamatsu C9920-02 calibrated integrating sphere system. [f] Cited from reference 8.

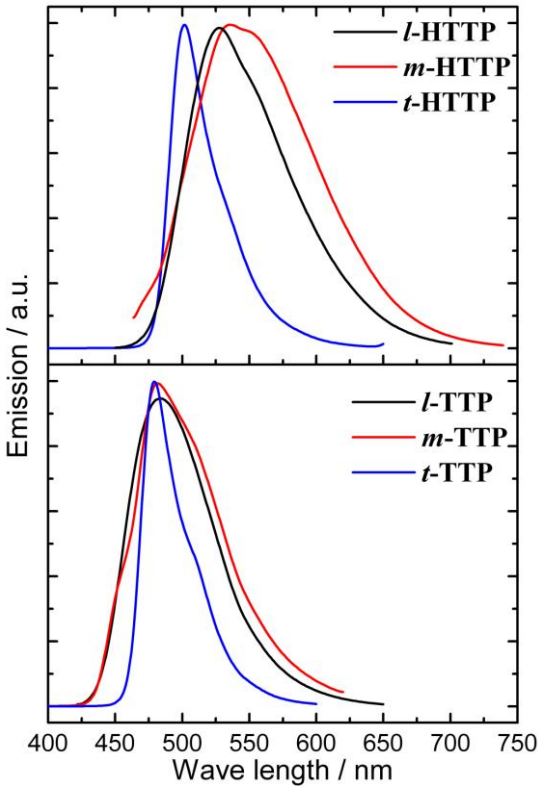

Fig. 2-4**.** Photoluminescence spectra of thiophene-fused phenazines in $CHCl_3$ solution (λ_{ex} 322 nm for ***t*-TTP**, 316 nm for ***m*-TTP**, 303 nm for ***l*-TTP**, 370 nm for ***l*-HTTP**, 380 nm for ***t*-HTTP**, and 380 nm for ***m*-HTTP**).

The maximum emission wavelengths of ***l*-TTP**, ***m*-TTP** and ***t*-TTP** are nearly the same (Fig. 2-4) as each other in the fluorescence spectra probably because the symmetry and orbital distribution of the excited molecular orbitals contributing to the emission are nearly the same as shown in Fig. 2-25 ~ 28.

2.2.4 Theoretical calculations on the electronic properties of phenazines and anthracene analogues

The molecular orbital calculations on the tetrathienophenazine derivatives and the corresponding anthracene analogues were carried out based on a density functional theory. The energy levels of the HOMO and LUMO for each molecule are listed in Table 2-1, and the energy diagrams are shown in Fig. 2-5 accompanied by the spatial distributions of the molecular orbitals. The HOMO levels of the unsubstituted tetrathienophenazine derivatives were estimated to be -5.60, -5.64, and -5.68 eV for

***l*-TTP**, ***m*-TTP**, and ***t*-TTP**, respectively. These values are lower than those of typical thiophene-fused aromatic molecules such as the anthrancene analogues (-5.18 ~ -5.23 eV)[9] and diacene-fused thieno[3,2-*b*]-thiophenes (-4.88 ~ -5.58 eV).[4c] This result is consistent with the experimental results from electrochemical measurements, and can be attributed to the introduction of an electron-deficient aromatic ring. The energy levels of LUMOs of the unsubstituted tetrathienophenazine derivatives were -2.27, -2.33, and -2.39 eV for ***l*-TTP**, ***m*-TTP**, and ***t*-TTP**, respectively. The ordering of the LUMO energy levels follows the same progression as those of the HOMOs, while the difference between the molecules was slightly larger than that of the HOMOs. Therefore, the HOMO-LUMO gaps in these molecules have the order ***l*-TTP** > ***m*-TTP** > ***t*-TTP**. This tendency was also observed in the optical band-gaps of these molecules, obtained experimentally, although the observed optical transitions did not come from the transitions between the HOMO and LUMO, as discussed later.

Although the energetic orders are not usually the same for each molecule, all the molecules show the same sets of molecular orbitals because all the molecules are based on the same shape of π-conjugating skeleton. The energy and the coefficients of the molecular orbitals on each atom are affected by the positions of sulfur atoms and the introduction of nitrogen atoms compared to the anthracene analogues. For example, the LUMO of the unsubstituted derivatives have the same orbital symmetry as each other, while the orbital symmetry of the HOMOs was not the same, depending on the positions of sulfur atoms (Fig. 2-5).

The estimated HOMO levels of the tetrathienophenazines from electrochemical experiments and DFT calculations were lower than those of the corresponding anthracene derivatives. This seems reasonable considering the introduction of an electron deficient aromatic ring. In the case of ***l*-TTP**, the frontier orbitals were estimated to be -5.60 and -2.27 eV for the HOMO and LUMO (Fig. 2-5), respectively, and those of the corresponding anthracene analogue (***l*-TTA**) were -5.19 and -1.69 eV (Fig. 2-5). On the other hand, the introduction of alkyl chains at the alpha positions of the fused thiophene rings increased the donor abilities. The effect of alkyl-substitution in these molecules was mainly seen in HOMO levels: the energy difference (increase)

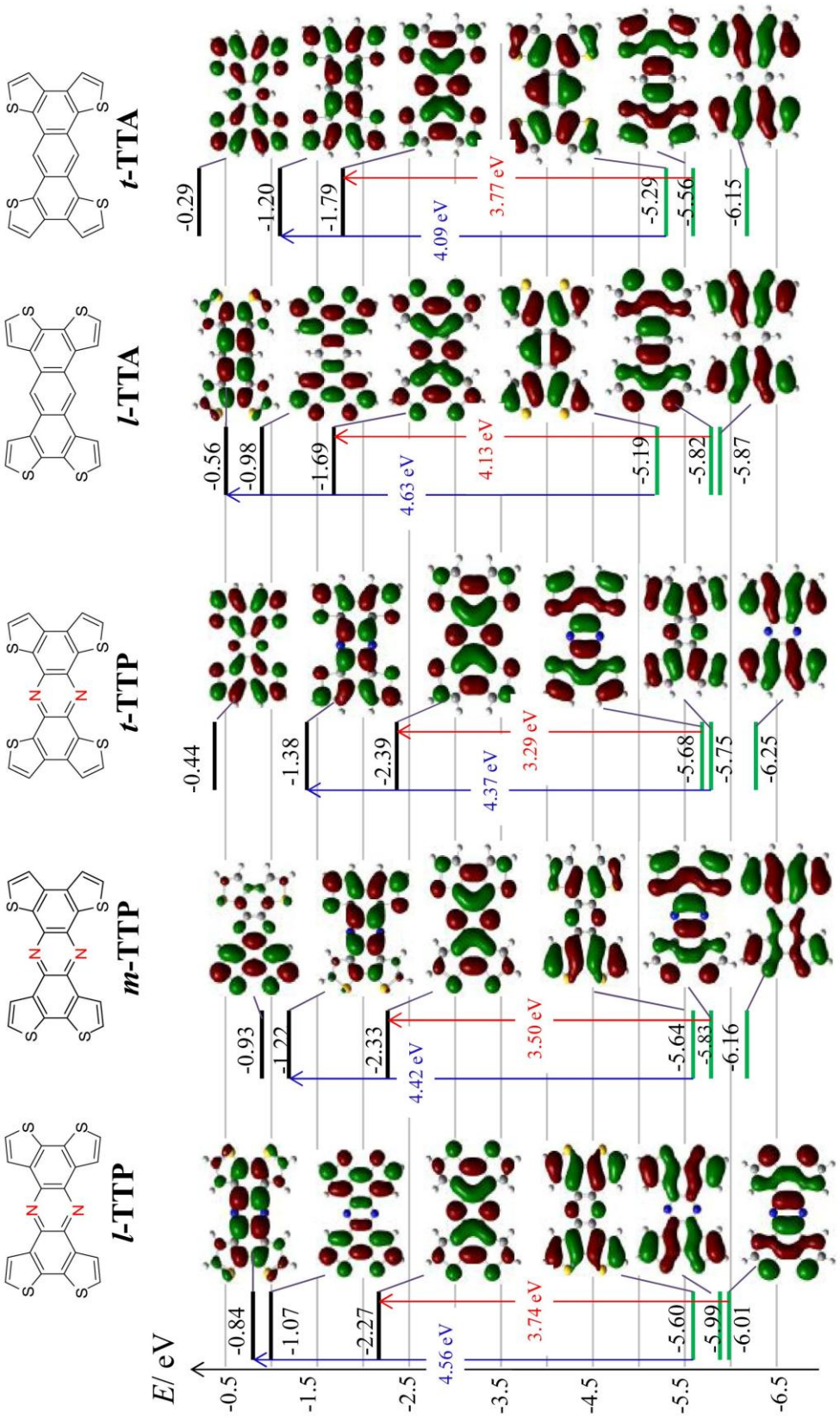

Fig. 2-5**.** Energies and spatial distributions of frontier orbitals of ***l*-TTP, *m*-TTP, *t*-TTP, *l*-TTA,** and ***t*-TTA**. Characteristic transitions are also indicated

upon alkyl-substitution in the HOMO levels were 0.41, 0.43, and 0.36 eV for ***l*-TTP**, ***m*-TTP** and ***t*-TTP**, respectively, and these values were larger than the change in LUMOs (0.23, 0.41, and 0.28, respectively). This leads to a bathochromic shifts in the absorption and florescence spectra upon both nitrogen introduction and alkyl-substitution of the molecules.

The absorption spectra of the phenazine derivatives showed two strong absorption bands, while those of the anthracene analogues showed only one strong absorption band, corresponding to the shorter wavelength band of the phenazine derivatives. This result was well reproduced by theoretical calculation, with an energy scaling factor of 0.94: two absorption bands for all of the phenazine derivatives and only one absorption band for the anthracene derivatives were predicted by TD-DFT

Table 2-2. Absorption wavelengths and their theoretical assignments for ***l*-TTP**, ***m*-TTP**, ***t*-TTP**, ***l*-TTA**, and ***t*-TTA**.

	Observed absorption band (λ_{max})	Calculated by TD-DFT	Assigned transition[a]	Energy difference	Contri-bution	Oscillator strength (*f*)
***l*-TTP**	302 nm	286 nm	HOMO→LUMO + 2	4.56 eV	0.24	0.831
			HOMO - 2→LUMO	3.74 eV	0.64	
	408 nm	375 nm	HOMO→LUMO + 2	4.56 eV	0.62	0.399
			HOMO - 2→LUMO	3.74 eV	-0.16	
***m*-TTP**	312 nm	309 nm	HOMO→LUMO + 1	4.42 eV	0.58	0.381
			HOMO - 1→LUMO	3.50 eV	-0.12	
	439 nm	405 nm	HOMO→LUMO + 1	4.42 eV	0.22	0.325
			HOMO - 1→LUMO	3.50 eV	0.64	
***t*-TTP**	320 nm	311 nm	HOMO - 1→LUMO + 1	4.37 eV	0.63	0.797
			HOMO→LUMO	3.29 eV	0.13	
	467 nm	432 nm	HOMO - 1→LUMO + 1	4.37 eV	-0.22	0.302
			HOMO→LUMO	3.29 eV	0.64	
***l*-TTA**	300 nm (strong)	286 nm	HOMO→LUMO + 2	4.63 eV	0.59	1.446
			HOMO - 1→LUMO	4.13 eV	0.35	
	479 nm (weak)	350 nm	HOMO→LUMO + 2	4.63 eV	-0.35	0.127
			HOMO - 1→LUMO	4.13 eV	0.61	
***t*-TTA**	310 nm (strong)	320 nm	HOMO→LUMO + 1	4.09 eV	0.60	1.262
			HOMO - 1→LUMO	3.77 eV	-0.37	
	418 nm (weak)	393 nm	HOMO→LUMO + 1	4.09 eV	0.37	0.058
			HOMO - 1→LUMO	3.77 eV	0.60	

[a] Assigned transitions and their corresponding energy difference were showed in Fig. 2-5.

calculations (Fig. 2-17 ~ 25). Although the orbital symmetries around the frontier orbitals (HOMO and LUMO) are not the same for each molecule, the symmetries of the molecular orbitals that contribute to the major two absorption bands are the same for all derivatives (Fig. 2-5). Furthermore, the two absorption bands consist of the same transitions as summarized in Table 2-2. For example, the two absorption bands in ***l*-TTP** are represented by a linear combination of two kinds of elemental transitions. One is the HOMO to LUMO+2 transition (4.56 eV) and the other is the HOMO-2 to LUMO transition (3.74 eV). These transition moments couple with each other to afford the two absorption bands (shorter and longer). Although the origin and the transition moments of the corresponding elemental transition in ***l*-TTA** are almost the same as that of ***l*-TTP**, the balance of the contributions of two transition moments for each band are not the same (Fig. 2-5). This could be attributed to the energy difference in the frontier orbitals. Among the four molecular orbitals of ***l*-TTP** participating to these optical transitions, the HOMO and LUMO have significant coefficients at the nitrogen atoms in the central ring, while HOMO-2 and LUMO+2 do not have any coefficient because these are the nodal positions of the MOs (Fig. 2-5). Compared with the energy difference from the corresponding MOs of ***l*-TTA**, the HOMO and LUMO of ***l*-TTP** are much lower than that of the HOMO-2 and LUMO+2. Since the nitrogen atoms with larger electron negativity are introduced at the central ring, the energies of HOMO and LUMO are decreased to a large extent, while the effect in the other two orbitals was not as large, due to the nodal positions. In the case of ***l*-TTA**, the two transitions were assigned to HOMO to LUMO+2 (4.63 eV) and HOMO-1 to LUMO (4.13 eV), respectively. Since the transition energies are close to each other, the transition moments couples effectively to cancel a longer absorption band, while the shorter absorption band is enhanced. On the other hand, the two transition moments in ***l*-TTP** have a relatively large difference so that the longer absorption band appears due to the imperfect cancellation between them.

The positions of the sulfur atoms also yield a significant difference in the orbital energies and absorption spectra. Both the HOMO and LUMO energies decrease in the order of ***l*-TTP** > ***m*-TTP** > ***t*-TTP** due to the effect of the different positions of the

sulfur atoms (Fig. 2-5). The longer absorption bands showed obvious red shifts in the order of ***l*-TTP** > ***m*-TTP** > ***t*-TTP**. This feature was also preserved in the alkyl substituted molecules (Fig. 2-5). Since the longer absorption band is mainly due to transitions related to LUMO, the decrease in the LUMO energy mainly contributes to the red shift of the longer wavelength absorption bands in the order of ***l*-TTP** > ***m*-TTP** > ***t*-TTP** (Fig. 2-5). The position of the sulfur atoms in ***t*-TTP** result in the higher energy of the HOMO (-5.68 eV) contributing to the longer wavelength absorption in comparison with that of ***l*-TTP** (-6.01 eV).

2.2.5 X-Ray Crystallography

From the six newly prepared derivatives, four derivatives (***t*-TTP**, ***m*-TTP**, ***l*-TTP** and ***l*-HTTP**) could be crystallized by solution or sublimation methods to afford single crystals suitable for X-ray diffraction. The cell parameters of these crystals are listed in Table 2-3. All of the unsubstituted derivatives (***t*-TTP**, ***m*-TTP** and ***l*-TTP**) have different space groups and cell parameters depending on the different positions of sulfur atoms in the skeleton. ***t*-TTP** (Fig. 2-6) showed nearly the same cell parameter and packing structure as its corresponding anthrancene analogue (***t*-TTA**), although the shortest S ··S contacts and π-π intermolecular distance (3.664(1) Å and 3.43 Å) are different from those of ***t*-TTA** (3.769(1) Å and 3.354(3) Å). ***l*-TTP** showed a different crystal structure from that of the corresponding anthracene analogue (***l*-TTA**).

Table 2-3. Crystal data and intermolecular contacts.

	***t*-TTP**	***l*-TTP**	***m*-TTP**	***l*-HTTP**
Crystal system	*monoclinic*	*monoclinic*	*monoclinic*	*triclinic*
Space group	$P2_1/n$	$P2_1/a$	$P2_1$	$P\bar{1}$
a (Å)	11.247(5)	17.064(2)	12.581(1)	4.894(1)
b (Å)	5.014(2)	3.894(4)	4.8247(5)	12.751(3)
c (Å)	14.169(6)	25.72(3)	13.718(1)	17.057(5)
α (deg)	---	---	---	76.147(1)
β (deg)	91.668(7)	108.820(2)	96.563(2)	84.810(1)
γ (deg)	---	---	---	72.178(1)
R, Rw	0.0618, 0.1027	0.1284, 0.2638	0.0502,	0.0627,
S ··S(Å)[a]	3.664(1)	3.686(2)	4.073(1)	---
δ(Å)[b]	3.43	3.48	3.46	3.40

[a] the shortest S ··S ´contacts. [b] δ is the averaged inter-planar distance between molecules along the π-stack.

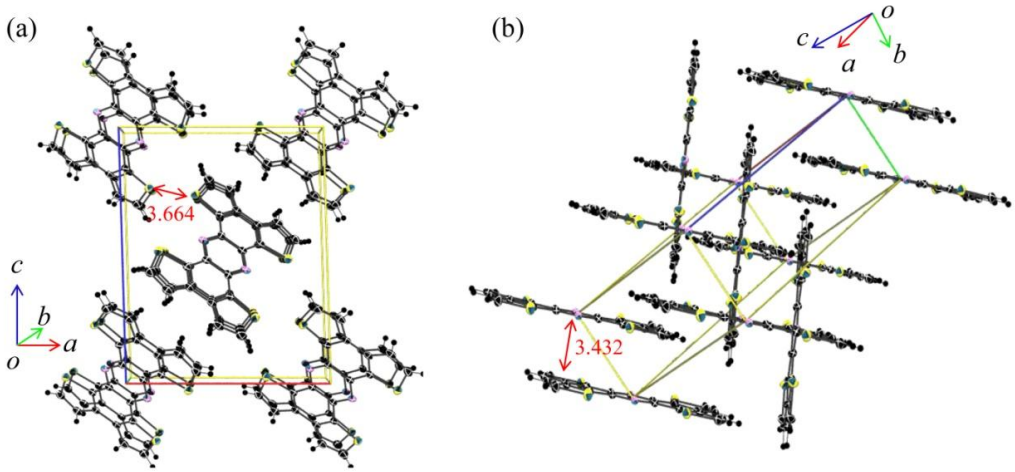

Fig. 2-6. (a) Crystal structure of ***t*-TTP**. S ··S ´contacts. (b) π···π distance between the molecules (unit: Å).

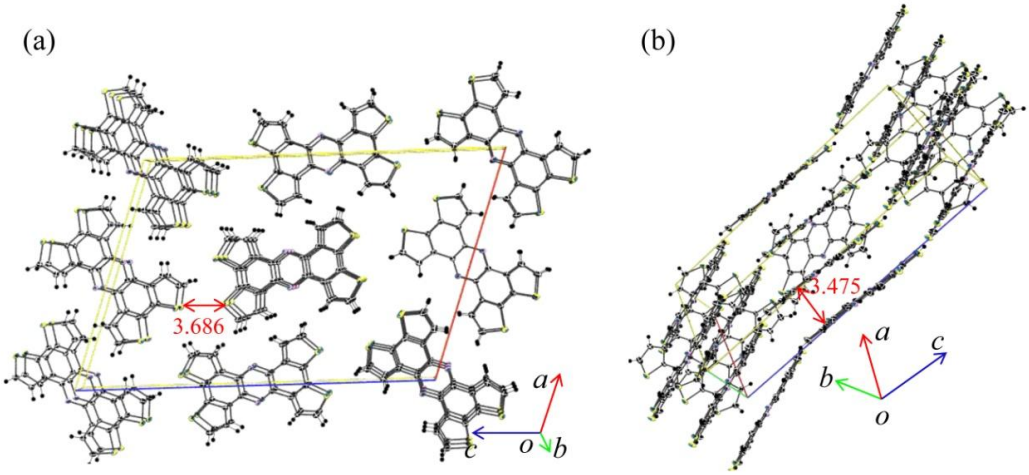

Fig. 2-7**.** (a) Crystal structure of ***l*-TTP**. (b) S ··S ´contacts. π···π distance between the molecules (unit: Å).

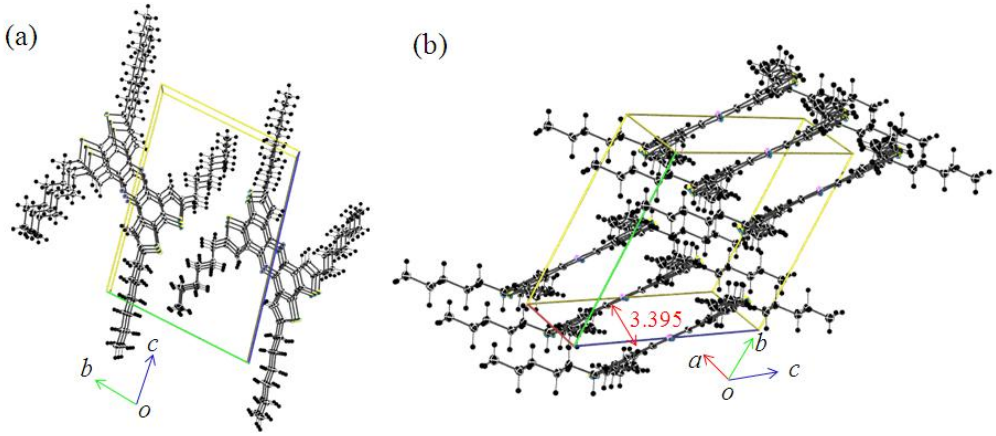

Fig. 2-8**.** Crystal structure of ***l*-HTTP**. (a) View along the *a* axis. (b) π···π distance between the molecules (unit: Å).

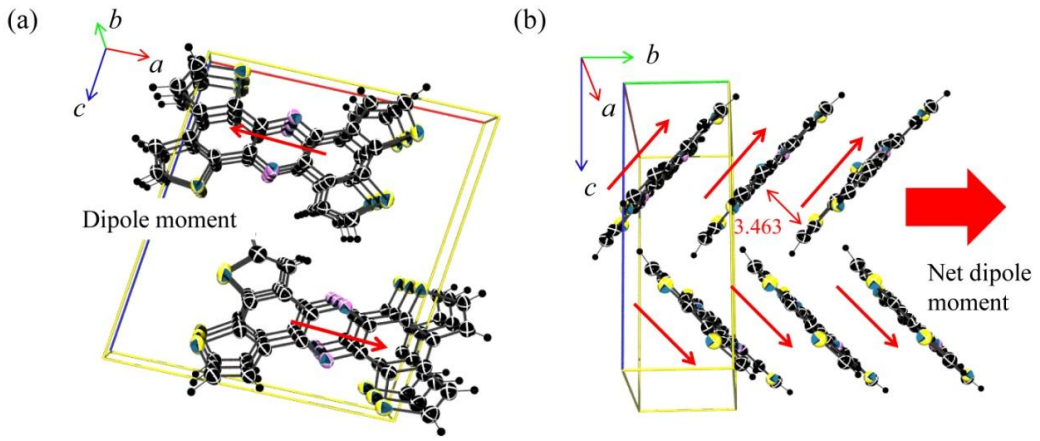

Fig. 2-9**.** Crystal structure of ***m*-TTP**. (a) Dipole moment of the molecular stacks. (b) π···π distance between the molecules and direction of the dipole moment (unit: Å).

The ***l*-TTP** crystal consists of two columns of slipped *π*-stacked (along the *b* axis) molecules with a *π*-*π* intermolecular distance of 3.48 Å (Fig. 2-7). The ***l*-HTTP** crystal consists of slipped *π*-stacked molecules along the *a* axis with a shorter *π*-*π* intermolecular distance (3.40 Å) than that of ***l*-TTP** (3.48 Å) (Fig. 2-8). The crystal of ***m*-TTP** also showed a slipped *π*-stacking structure with a *π*-*π* intermolecular distance of 3.46 Å. Since the dipole moments of molecular stacks do not completely compensate each other in the crystal cell, ***m*-TTP** is a polar crystal (Fig. 2-9).

The crystals of the three isomers, ***l*-TTP**, ***m*-TTP** and ***t*-TTP,** showed different packing structures. The different sulfur positions of these molecules lead to a difference in their molecular shape, intermolecular S ··S contacts, distributions and energies of the molecular orbitals, and the resultant charge distributions. Since all these factors can contribute to the intermolecular packing structures, it is hard to conclude what is the most important factor to control the crystal structure in this case.

On the other hand, the difference in **TTP**s and **TTA**s is simpler. The replacement of the –CH= moieties of the **TTA**s with –N= does not change the molecular shape, and has little effect on the intermolecular S ··S contacts although the molecular orbitals and the charge distributions should be affected. Actually, there are obvious differences in the energies of frontier orbitals and the charge distribution on the central ring between these systems. Furthermore, the characters of the HOMOs are different between ***t*-TTP** and ***t*-TTA**. Among the obtained crystals, ***l*-TTP** has the most different crystal structure

from ***l*-TTA**, while ***t*-TTP** afforded an isostructural crystal with ***t*-TTA.** While the charge distributions on the central ring can mainly contribute to the π-stacking structure in this case, the S ··S contacts are considered to affect both the π-stacking and the side-by-side interactions. The above result could be explained by means of the balance of the effects of charge distributions and the S ··S contacts.

2.2.6 Preparation, characterization, and FET performance of thin-films

Thin films of the alkyl-substituted tetrathienophenazine derivatives were prepared by vapor deposition (Fig. 2-13a) on Si substrates (with SiO_2 on the surface). X-ray diffraction analyses of thin films yielded information on the molecular arrangements in the films. Thin-film X-ray diffraction of ***l*-HTTP** grown under different conditions show sharply resolved peaks assignable to multiple reflections, indicating crystalline order in the direction of substrate normal (Fig. 2-10). Thin films deposited on the untreated and HMDS (Hexamethyldisilazane) treated Si substrates at T_{sub} = 25 ˚C consisted of two series of multiple (00*l*) and (00*l'*) reflections, while thin films deposited at T_{sub} = 75 ˚C showed only one series of multiple (00*l*) reflections. However, neither the (00*l*) nor (00*l'*) peaks were assignable to the simulated powder pattern of the single-crystal phase vapor-deposited thin films of ***l*-HTTP** have distinct phases from the single crystalline phase. The interlayer spacing (*d*), determined from the first-layer line of the XRD, are 19.4 Å and 24.3 Å for (00*l*) and (00*l'*) reflections, respectively. This result suggests that the thin film contains only one molecular arrangement on the substrate when deposited at higher temperature. In addition, the thin films deposited at T_{sub} = 75 ˚C showed larger grains (width: 0.25 ~ 0.5 μm and height: 10.0 ~ 30.0 nm), and tighter packing on the substrates than thin films deposited at room temperature (width: 0.5 ~ 1.5 μm and height: 20.0 ~ 40.0 nm) observed from AFM images (Fig. 2-11).

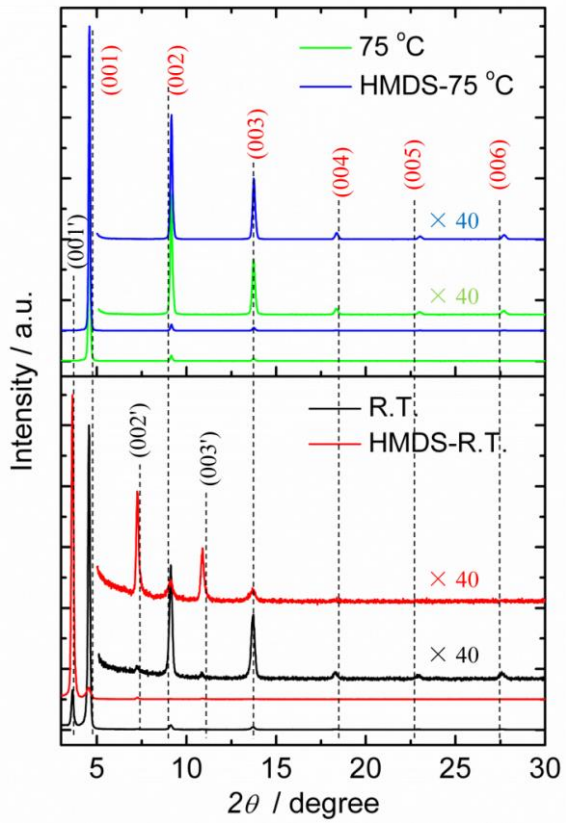

Fig. 2-10**.** Out-of-plane XRD pattern of ***l*-HTTP** thin films (50 nm) at different substrate temperatures (no in-plane signal).

Organic field-effect transistor (OFET) devices of these derivatives were prepared on bottom-gate, bottom-contact substrates by vacuum deposition (Fig. 2-13). The thin films of ***l*-HTTP** deposited at room temperature on surface-oxidized silicon substrate showed FET characteristics. The field-effect mobilities for this compound were μ_h = 1.2 × 10^{-8} cm^2 V^{-1} s^{-1} and μ_h = 4.6 × 10^{-9} cm^2 V^{-1} s^{-1} for untreated and HMDS treated substrates (Table 2-4), respectively. These values were greatly improved by increasing the substrate temperature during vapor deposition: μ_h = 6.2 × 10^{-6} cm^2 V^{-1} s^{-1} andμ_h = 3.2 × 10^{-6} cm^2 V^{-1} s^{-1} for untreated and treated substrates (T_{sub} = 75 ˚C), respectively. The on/off ratio and threshold voltage of the FET devices are listed in Table 2-4. These results suggest that the mono-oriented phase and bigger grains in the thin films can improve the transistor performance while the HMDS treatment on the SiO_2 surface does not yield an obvious effect in ***l*-HTTP** thin film transistor characteristic.

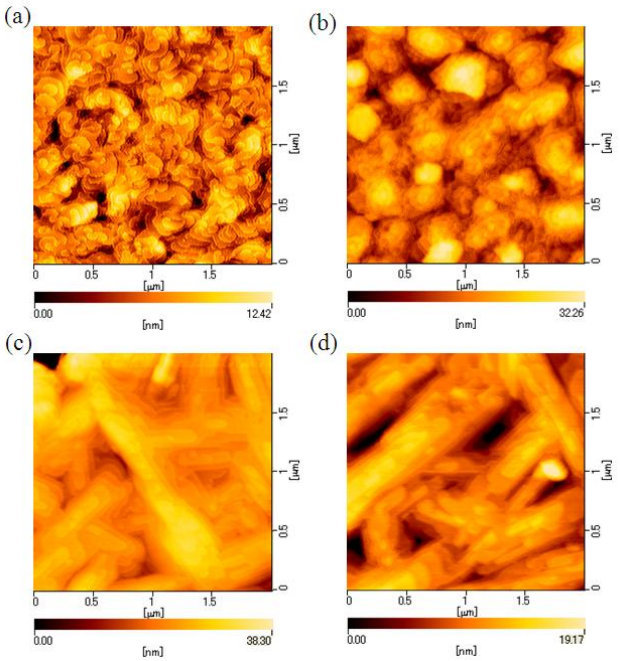

Fig. 2-11**.** AFM images of thin films of ***l*-HTTP** on bare substrates with T_{sub} = 25 ˚C (a), substrates treated by HMDS with T_{sub} = 25 ˚C (b), bare substrates with T_{sub} = 75 ˚C (c) and substrates treated by HMDS with T_{sub} = 75 ˚C (d).

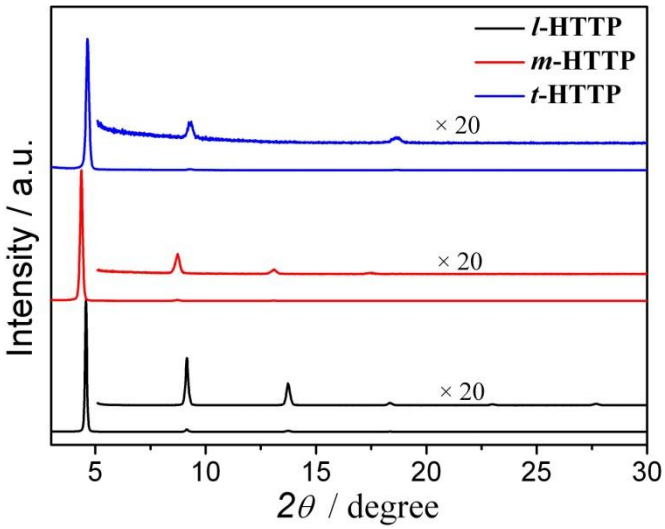

Fig. 2-12**.** Out-of-plane XRD pattern of ***l*-HTTP**, ***t*-HTTP** and ***m*-HTTP** vacuum-sublimed on Si substrates (no peak in in-plane spectrum) with T_{sub} = 75˚C.

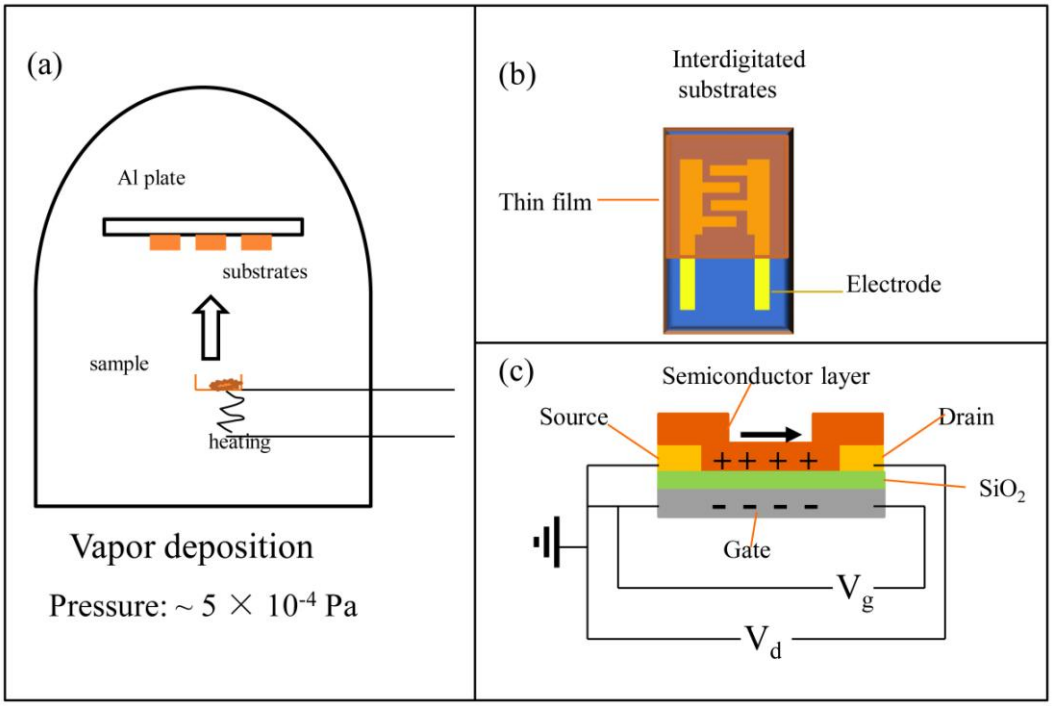

Fig. 2-13**.** Chamber of vapor deposition (a), interdigitated substrate (b), bottom gate/bottom contact circuit of FET device (c).

Thin films of ***m*-HTTP** and ***t*-HTTP** were also prepared by vapor deposition at T_{sub} = 75 ˚C on the Si substrates without HDMS treatment. The thin films of these materials also showed high crystallinity, characterized by thin-film XRD (Fig. 2-12). These films also showed FET characteristics with field-effect mobilities of $\mu_h = 2.9 \times 10^{-6}$ cm^2 V^{-1} s^{-1} and $\mu_h = 2.5 \times 10^{-6}$ cm^2 V^{-1} s^{-1} for ***t*-HTTP** and ***m*-HTTP**, respectively (Fig. 2-14 and Table 2-4). The substitution dependence of the tetrathienophenazines on the FET characteristics is similar to that of the anthrancene analogues: the alkyl-substituted anthrancene analogues showed reasonable transistor performance (~10^{-2} cm^2 V^{-1} s^{-1}), while the unsubstituted anthrancene analogues did not show a field effect.

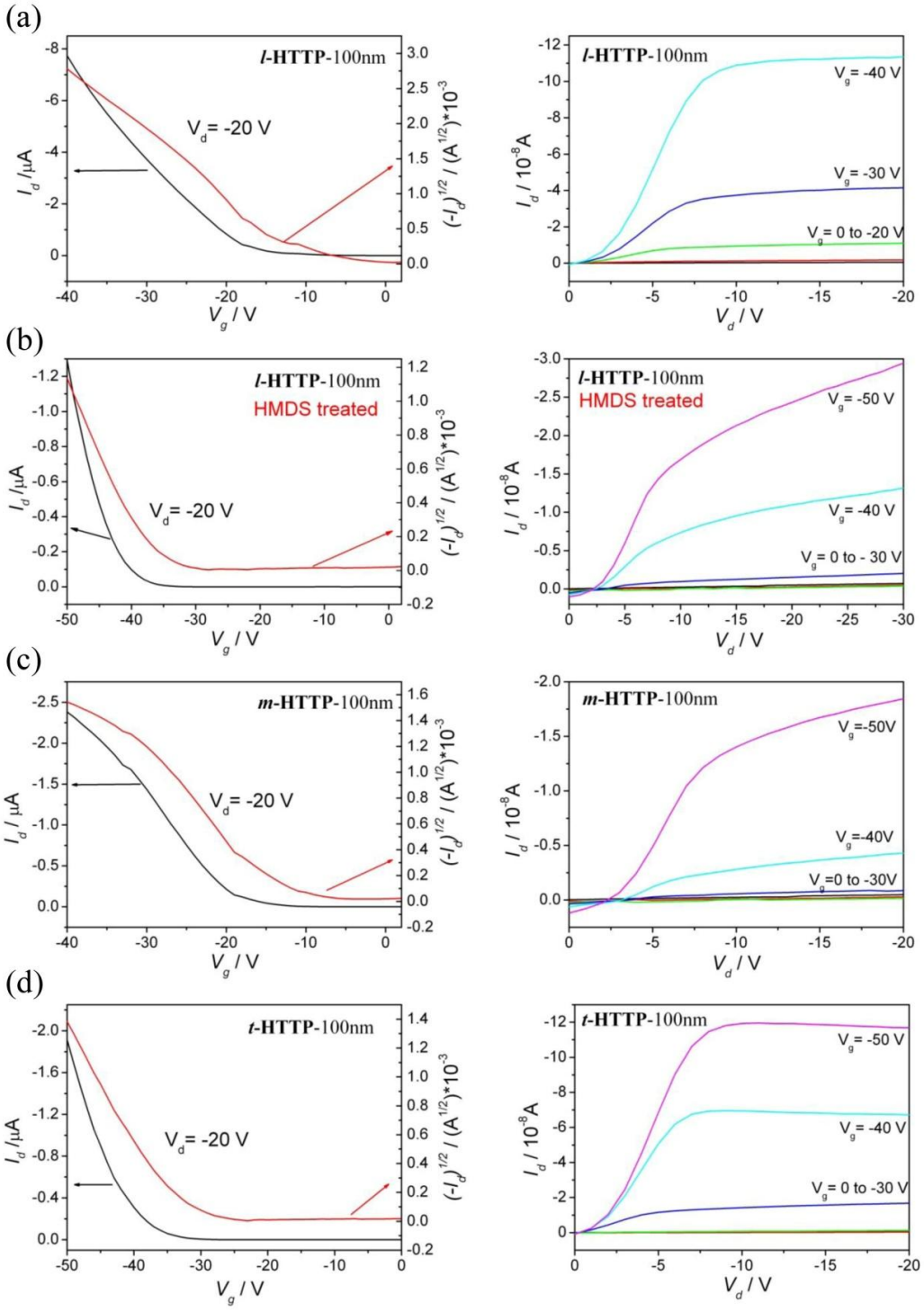

Fig. 2-14**.** Transfer (left) and output (right) characteristics of thin films of ***l*-HTTP** (a), ***m*-HTTP** (c) and ***t*-HTTP** (d) vacuum-sublimed on SiO_2/Si. Thin film of ***l*-HTTP** on HMDS treated SiO_2/Si (b).

Table 2-4. Thin film properties of thiophene-fused phenazines.

	Surface	T_{sub} [a]	*d*-spacing / Å	μ_h / $cm^2V^{-1}s^{-1}$	$I_{on/off}$	V_{th} / V
***l*-HTTP**	HMDS	25℃	24.3	1.2×10^{-8}	10^3	---
***l*-HTTP**	Bare	25℃	24.3	4.6×10^{-9}	10^4	---
***l*-HTTP**	HMDS	75℃	19.4	3.2×10^{-6}	10^4	−33
***l*-HTTP**	Bare	75℃	19.4	6.2×10^{-6}	10^4	−24
***t*-HTTP**	Bare	75℃	19.0	2.9×10^{-6}	10^5	−23
***m*-HTTP**	Bare	75℃	20.2	2.5×10^{-6}	10^4	−38

[a] Substrate temperature upon vapor deposition

The alkyl-substituted phenazines (***l*-HTTP**, ***m*-HTTP** and ***t*-HTTP**) showed nearly the same field effect transistor characteristics, probably because the thin films of these materials showed nearly the same crystallinities, although the positions of the sulfur atoms are different in these molecules. In comparison with the anthracene analogues, the alkyl-substituted phenazines showed lower FET mobilities (~10^{-6} cm^2 V^{-1} s^{-1}, compared with ~10^{-2} cm^2 V^{-1} s^{-1} for the anthracene analogues). This could be due to the relatively low donor abilities and the large reorganization energies of the phenazines in comparison with the corresponding anthracenes, as discussed later.

2.2.7 Theoretical calculation on charge transport properties of thiophene-fused phenazines

To evaluate the charge transport properties of the obtained crystals, the intermolecular hopping carrier mobility was calculated on the basis of Marcus theory.[16] The calculated parameters and the evaluated intermolecular carrier mobilities along the crystal axes are listed in Table 2-5. In each case, hole mobilities of 0.5 ~ 5.0 × 10^{-1} cm^2 V^{-1} s^{-1} were predicted along π-staking directions and 10^{-3} ~ 10^{-2} cm^2 V^{-1} s^{-1} in other directions. This result suggests that these crystals have reasonable potential for organic transistors. However, the experimental results of the field effect mobilities of thin films of these molecules were much lower than that of the theoretical predictions. This could be attributed to the different packing structures of the thin films from the crystals. The other factors for decreasing the charge mobility could

Table 2-5. Calculated hopping mobilities of thiophene-fused phenazines.

Molecules	Contact[a]	*Hab*[b] /meV	*Sab*[b] /meV	*d* /Å	*V* /meV	λ^c / meV	$\mu_{hopping}$ $cm^2\ V^{-1}\ S^{-1}$
***l*-TTP**	*a*	7.7	-0.7	8.748	3.6	153	6.1×10^{-3}
***l*-TTP**	*c'*	14.5	-1.6	13.002	5.9	153	3.5×10^{-2}
***l*-TTP**	*(a+c)'*	3.2	-0.3	13.507	1.6	153	2.9×10^{-3}
***l*-TTP**	*b'*	-162.4	13.9	3.892	-91.3	153	7.6×10^{-1}
***m*-TTP**	*a*	-0.7	0.1	12.581	-0.3	169	8.9×10^{-5}
***m*-TTP**	*b*	-133.3	12.9	4.825	-66.5	169	5.0×10^{-1}
***m*-TTP**	$c_{//}$'	-1.8	-0.02	7.857	-1.9	169	1.1×10^{-3}
***m*-TTP**	$c_{\perp}$	25.9	-2.6	11.941	11.7	169	9.5×10^{-2}
***t*-TTP**	*b-a*	0.6	-0.2	12.314	-0.4	174	1.3×10^{-4}
***t*-TTP**	*b*	59.1	-7.4	5.014	20.2	174	4.7×10^{-2}
***t*-TTP**	*(a+c)'*	-24.1	2.4	9.262	-9.3	174	5.0×10^{-2}
***t*-TTP**	*a-c*	-8.3	0.9	11.862	-3.6	174	8.4×10^{-3}
***l*-HTTP**	t_1	-50.8	5.6	4.892	-25.0	155	8.7×10^{-2}
***l*-HTTP**	t_2	-3.9	0.4	12.749	-2.0	155	3.8×10^{-3}

[a] Corresponding molecular contacts are indicated in Fig. 2-28~ 32. [b] Calculated at PW91/TZ2P level. [c] Calculated at B3LYP/6-31G(d) level.

be the relatively low HOMO energy and relatively large reorganization energy for the hole transfer process. These factors relate to the charge injection at the electrode semiconductor interface, and the charge transport processes in bulk material, respectively.

2.2.8 Chemical doping effect on transport properties

Since all of the thiophene-fused phenazine derivatives afforded crystalline thin films by vapor deposition (for thin-film XRD characterization of unsubstituted derivatives, see Fig. 2-15), the conductivity of these thin films were studied as well. In all cases, the conductivities were improved several orders of magnitude by I_2 doping (Fig. 2-16 and Table 2-6). The single crystals of these (four) derivatives also showed an increase in conductivity upon I_2 doping. The change in conductivites of the iodine-doped single crystals (10^{-7}~10^{-5} Scm^{-1} to 10^{-2}~10^{-1} Scm^{-1}) were much higher than those of the thin

films (10^{-11}~10^{-8} Scm^{-1} to 10^{-7}~10^{-5} Scm^{-1}). This is reasonable because the continuous molecular π-stacking structure in the single crystals should be better for charge transport than that in the thin films with many grain boundaries.

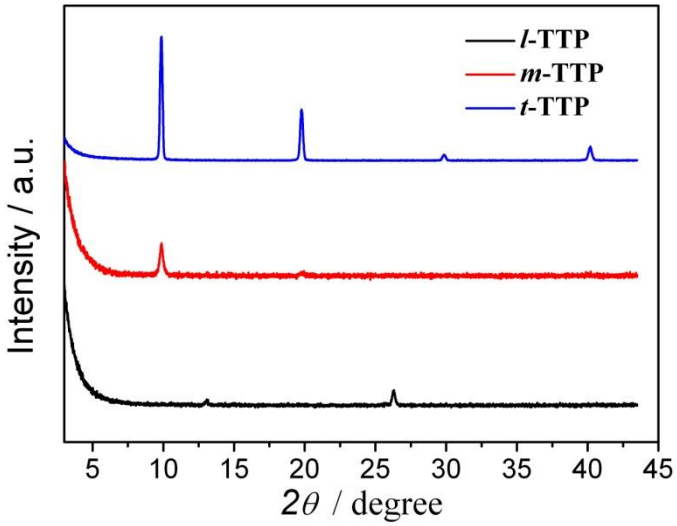

Fig. 2-15**.** Out-of-plane XRD pattern (Cu *K*α source: λ = 1.541 Å) of ***l*-TTP**, ***m*-TTP** and ***t*-TTP** vacuum-sublimed on Si substrates (no peak in in-plane spectrum) at T_{sub} = 25 ℃.

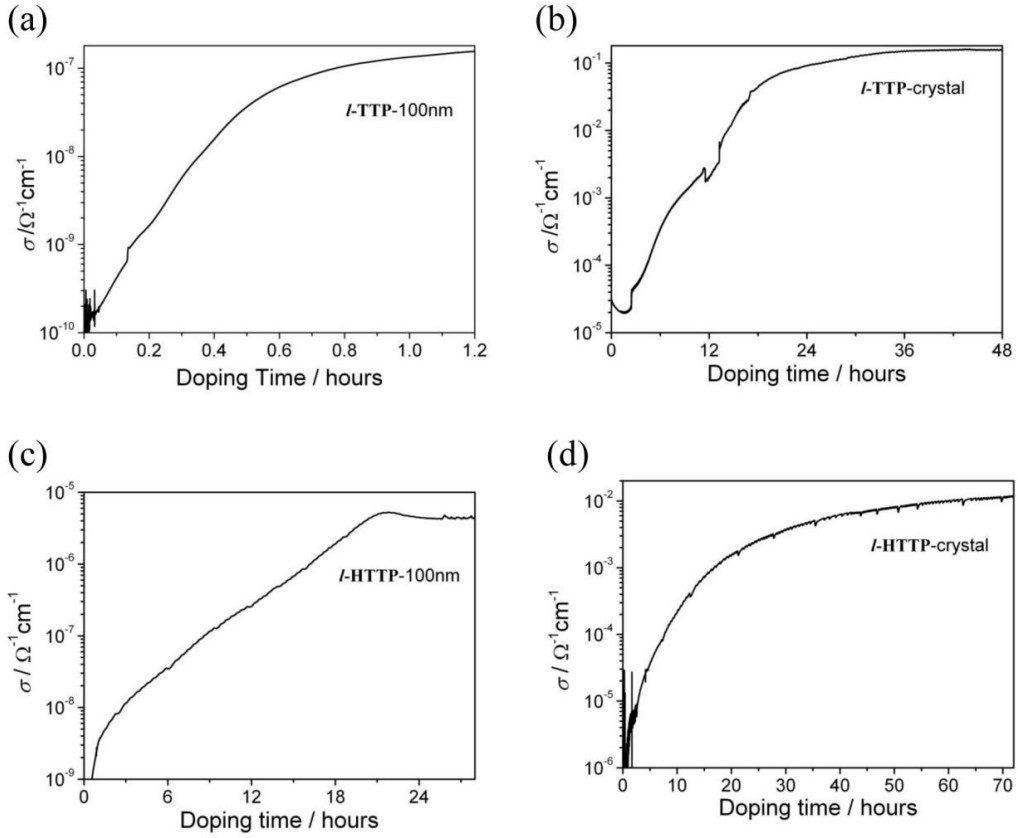

Fig. 2-16**.** Conductivity change during I_2 vapor doping in thin film (a) and crystal (b) of ***l*-TTP**; and thin film (c) and crystal (d) of ***l*-HTTP** (conductivity data of the other derivatives are listed in Table 2-6).

Table 2-6**.** Conductivity improvement of thiophene-fused phenazines doped by I_2 vapor in the crystal state and thin-film state (unit: S cm^{-1}).

	Crystal	Thin-film
***l*-TTP**	$10^{-5}\rightarrow10^{-1}$	$10^{-10}\rightarrow10^{-7}$
***m*-TTP**	$10^{-7}\rightarrow10^{-2}$	$10^{-8}\rightarrow10^{-5}$
***t*-TTP**	$10^{-7}\rightarrow10^{-2}$	$10^{-9}\rightarrow10^{-6}$
***l*-HTTP**	$10^{-6}\rightarrow10^{-2}$	$10^{-9}\rightarrow10^{-5}$
***m*-HTTP**	---	$10^{-11}\rightarrow10^{-5}$
***t*-HTTP**	---	$10^{-11}\rightarrow10^{-5}$

2.3 Conclusion

A series of novel thiophene-fused phenazines (***l*-TTP**, ***t*-TTP**, ***m*-TTP**, and their alkyl-substituted derivatives) were prepared through the formation of the phenazine skeleton by a key condensation reaction between diketones and diamines, themselves derived from the diketones without the need for expensive organometallic catalysts. Both symmetric and asymmetric molecules were obtained by this method. These materials were characterized by exact EI-MS, elemental analysis, NMR and single crystal X-ray crystallography. The hexylated derivatives showed much higher solubility than the unsubstituted derivatives in non-polar organic solvents. The optical and electronic properties of these materials were also investigated and found pronounced differences from their anthracene analogues. These materials showed two strong absorption bands, while the anthracene analogues only showed one strong absorption band in the UV-vis spectra. They also showed different fluorescence properties. Three unsubstituted derivatives (***t*-TTP**, ***m*-TTP** and ***l*-TTP**) showed light-blue fluorescence in chloroform, while ***t*-HTTP** showed green fluorescence and both ***m*-HTTP** and ***l*-HTTP** showed yellow fluorescence. The cyclic voltammograms indicated that the alkyl-substituted derivatives are weaker donors than the corresponding anthracene analogues. Thin films of these materials were prepared by sublimation, and different molecular packing structure and grains sizes were obtained when depositing at room temperature and at T_{sub} = 75 °C. Thin films of the alkyl-substituted derivatives show maxium field effect mobilities of 10^{-6} ~ 10^{-7} cm^2 V^{-1} s^{-1} when deposited at T_{sub} = 75 °C, which was significantly larger than those formed at room temperature, due to a mono-oriented phase structure and bigger grains in the thin films. The conductivity of these materials can be improved several orders of magnitude by iodine doping in the thin-film state and crystal state. The crystals and the thin films showed conductivities of 10^{-2}~10^{-1} $\Omega^{-1}cm^{-1}$ and 10^{-7}~10^{-5} $\Omega^{-1}cm^{-1}$ after chemical doping, respectively. We can conclude that these derivatives can also be utilized for organic electronics.

2.4 Experiment section

General Procedures

All chemicals and solvents purchased were used without further purification unless otherwise stated. Compound **1a**,[12] **2a**,[12] **8**[9] and **9**[9] were synthesized according to reported procedures. NMR spectra were measured using 400 MHz or 600 MHz JEOL WinAlpha A-600 using TMS as internal reference. Low resolution and high resolution EI-MS spectra were measured using JOEL JMS-T100GCV with perfluorokerosene (PFK) as matrix. Cyclic voltammetry (CV) was carried out using HOKUTO DENKO HZ-5000 under nitrogen gas. UV-vis spectra were measured by JASCO V-570. Fluorescence spectra were measured by JASCO FP-6600 and absolute fluorescence quantum yields were determined with a Hamamatsu C9920-02 calibrated integrating sphere system. Dynamic Atomic Force Microscopy (AFM) measurements for the thin films on Si substrate were carried out on SII SPI3800.

Preparation of 1b.

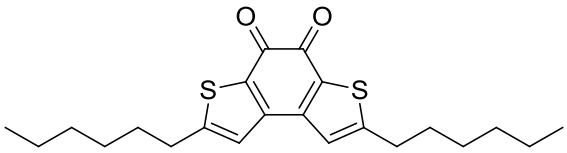

2,7-dihexylbenzo[1,2-b:4,3-b']dithiophene-4,5-dione

n-Butyllithium (48 mL, 1.6 M in hexane, 76.8 mmol) was added dropwise to a solution of compound **11** (10.6 g, 31.6 mmol) in THF (150 mL) at -78 °C under N_2 gas. The mixture was stirred at -78 °C for 1 hour and diethyl oxalate (6.2 g, 42 mmol) was added to the mixture via a syringe at -78 °C. The mixture was stirred at -78 °C for 2 hours and then the temperature was allowed to slowly rise to room temperature. After stirring overnight, the obtained dark red mixture was quenched with saturated aqueous NH_4Cl, extracted by ethyl ether (200 mL × 3), and the combined organic layers were dried over Na_2SO_4. After removing the solvent, the residue was recrystalized from methanol/ethyl acetate (2/1) at -20 °C to yield a red solid (5.24 g, yield: 43%). IR ν_{max} = 3076 (w), 2924 (s), 2850 (s), 1645 (s), 1450 (m), 1404 (s), 1298 (m), 860 (w) cm^{-1}.

High resolution EI-MS (M^+) for $C_{22}H_{28}O_2S_2$ found: 388.15234; calcd: 388.1531. ^{1}H NMR ($CDCl_3$, 400 MHz): δ 6.91 (2H, s), 2.88 ~ 2.84 (4H, t, J = 7.58 Hz), 1.76 ~ 1.68 (4H, m), 1.41 ~ 1.29 (12H, m), 0.92 ~ 0.88 (6H, t, J = 7.08 Hz); ^{13}C NMR ($CDCl_3$, 100 MHz): δ 173.56, 161.27, 143.00, 122.44, 122.29, 31.42, 31.06, 31.01, 28.64, 22.49, 14.10.

Preparation of 2b.

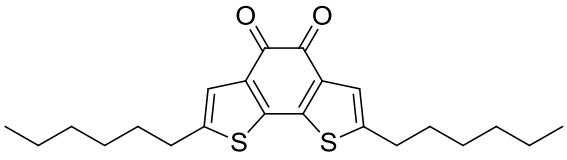

2,7-dihexylbenzo[1,2-b:6,5-b']dithiophene-4,5-dione

n-Butyllithium (67 mL, 1.6 M in hexane, 101 mmol) was added dropwise to mixture solution of compound **9** (22.95 g, 46.6 mmol) in anhydrous THF (150 mL) at -78 °C under N_2 gas. The mixture was stirred at -78 °C for 1 hour and diethyl oxalate (9.64 g, 66 mmol) was added to the mixture via a syringe at -78 °C. The mixture was stirred at -78 °C for 2 hours and then the temperature was allowed to slowly rise to 0 °C. The obtained dark blue mixture was quenched with saturated aqueous NH_4Cl, extracted with ethyl ether (300 mL × 3) and the combined organic layers were dried over Na_2SO_4. After removing the solvent, the residue was purified by chromatography, eluting with hexane/ethyl acetate (20 : 1, 10 : 1) to afford a black solid 8.06 g (yield: 44%). IR ν_{max} = 2925 (s), 2857 (m), 1653 (s), 1397 (m), 845 (w) cm^{-1}. High resolution EI-MS (M^+) for $C_{22}H_{28}O_2S_2$ found: 388.1527; calcd: 388.1531. ^{1}H NMR ($CDCl_3$, 400 MHz): δ 7.12 (2H, s), 2.78 ~ 2.74 (4H, t, J = 7.40 Hz), 1.69 ~ 1.62 (4H, m), 1.38 ~ 1.31 (12H, m), 0.91 ~ 0.88 (6H, t, J = 6.80 Hz); ^{13}C NMR ($CDCl_3$, 100 MHz): δ 174.67, 146.51, 142.63, 134.59, 124.0 (×2), 31.42, 30.94, 29.84, 28.57 (×2), 22.54 (×2), 14.09 (×2).

Preparation of 3a

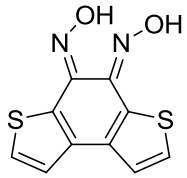

benzo[1,2-b:4,3-b']dithiophene-4,5-dione dioxime

Benzo[1,2-b:4,3-b']dithiophene-7,8-quinone (0.55 g, 2.5 mmol) and hydroxylamine hydrochloride (1.75 g, 25.0 mmol) in pyridine (3.0 mL) and ethanol (12.0 mL) were refluxed overnight. The reaction mixture was evaporated and the obtained light yellow residue was suspended in 20 mL water, followed by dropwise addition of concentrated hydrochloric acid until pH ≤ 4. The mixture was filtered, washed with water and the filter cake was dried in a desiccator to afford a red solid (0.61 g, 97%). IR ν_{max} = 3166 (s), 3105 (s), 1653 (w), 1381 (m), 1125 (w) cm^{-1}. High resolution EI-MS (M^+) for $C_{10}H_6N_2O_2S_2$ found: 249.9865; calcd: 249.9871. ^1H NMR (Acetone-d_6, 400 MHz): δ 7.97 ~ 7.96 (0.4H, d, J = 5.20 Hz), 7.81 ~ 7.80 (1H, d, J = 4.80 Hz), 7.67 ~ 7.66 (0.4H, d, J = 5.20 Hz), 7.60 ~ 7.59 (2H, d, J = 5.60 Hz); ^{13}C NMR (DMSO-d_6, 100 MHz): δ 143.25, 134.92, 131.78, 123.48, 122.70.

Preparation of 3b

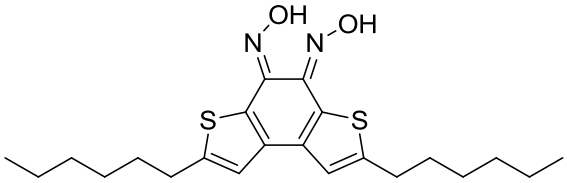

2,7-dihexylbenzo[1,2-b:4,3-b']dithiophene-4,5-dione dioxime

Compoud **1b** (0.388 g, 1.0 mmol) and hydroxylamine hydrochloride (0.7 g, 10.0 mmol) in pyridine (3.0 mL) and ethanol (15.0 mL) were stirred at 70 °C for 3 hours. The reaction mixture was evaporated and the obtained light yellow residue was suspended in 40 mL water/methanol = 2/1, followed by dropwise addition of concentrated hydrochloric acid until pH ≤ 4. The mixture was filtered, washed with water and the filter cake was dried in desiccator to afford a red solid (0.39g, 93%). IR ν_{max} = 3151 (m), 3045 (m), 2924 (s), 2857 (s), 1397 (m), 1275 (m), 821 (m) cm^{-1}. High

resolution EI-MS (M^+) for $C_{22}H_{30}N_2O_2S_2$ found: 418.1756; calcd: 418.1749. ^{1}H NMR ($CDCl_3$, 400 MHz): δ 6.94 (2H, s), 2.85 ~ 2.81 (4H, t, J = 7.58 Hz), 1.74 ~ 1.70 (4H, m), 1.38 ~ 1.31 (12H, m), 0.91 ~ 0.88 (6H, t, J = 6.60 Hz); ^{13}C NMR ($CDCl_3$, 100 MHz): δ 153.6, 138.3, 137.0, 120.7, 120.0, 31.6, 31.3, 30.3, 28.9, 22.6, 14.1.

Preparation of 4a

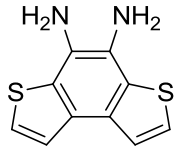

benzo[1,2-b:4,3-b']dithiophene-4,5-diamine

A solution of $SnCl_2$ (anhydrous, 1.9 g, 10.0 mmol) in concentrated hydrochloric acid (5 mL) was added to a mixture of compound **3a** (0.5 g, 2.0 mmol) in ethanol (10 mL) at 0 ^{o}C. After stirring for 10 min, the mixture was taken to reflux for 3 h. The reaction mixture was filtered and washed with water and ethanol. The filter cake was suspended in saturated aqueous $NaHCO_3$ (30 mL) and extracted with CH_2Cl_2 (30 mL × 3). The organic phases were combined and dried over Na_2SO_4. Evaporation of the solvent afforded a beige powder (0.296 g, 67%). IR ν_{max} = 3394 (m), 3325 (m), 3272 (m), 3091 (w), 1486 (s), 1443 (s), 701 (s) cm^{-1}. High resolution EI-MS (M^+) for $C_{10}H_8N_2S_2$ found: 220.0136; calcd: 220.0129. ^{1}H NMR ($CDCl_3$, 600 MHz): δ 7.64 ~ 7.63 (2H, d, J = 5.16 Hz), 7.35 ~ 7.34 (4H, 2H, d, J = 4.38 Hz), 3.66 (br, s); ^{13}C NMR ($CDCl_3$, 150 MHz): δ 130.14, 129.05, 124.74, 122.94, 122.37.

Preparation of 4b

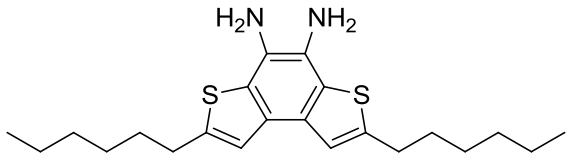

2,7-dihexylbenzo[1,2-b:4,3-b']dithiophene-4,5-diamine

A solution of $SnCl_2$ (anhydrous, 0.90 g, 4.7 mmol) in concentrated hydrochloric acid (3 mL) was added to a mixture of compound **3b** (0.387 g, 0.9 mmol) in ethanol (20 mL) at 0 ^{o}C. The yellow solution became black immediately, and then it was stirred at room

temperature overnight. The reaction mixture was filtered and washed with water and ethanol. The filter cake was suspended in saturated aqueous $NaHCO_3$ (30 mL) and extracted were CH_2Cl_2 (30 mL × 3). The organic phases were combined and dried over Na_2SO_4. Evaporation of the solvent afforded a dark yellow solid (0.287g, 80%). IR ν_{max} = 3409 (w), 3325 (w), 2924 (s), 2850 (m), 1616 (w), 1465 (m), 845 (w) cm^{-1}. High resolution EI-MS (M^+) for $C_{22}H_{32}N_2S_2$ found: 388.2006; calcd: 388.2007. ^1H NMR ($CDCl_3$, 400 MHz): δ 7.19 (2H, s), 3.46 (4H, s, br), 2.92 ~ 2.88 (4H, t, J = 7.08 Hz), 1.78 ~ 1.71 (4H, m), 1.40 ~ 1.30 (12H, m), 0.91 ~ 0.87 (6H, t, J = 7.08 Hz); ^{13}C NMR ($CDCl_3$, 100 MHz): δ 142.84, 128.63, 128.45, 124.00, 119.49, 31.61, 31.35, 30.87, 28.77, 22.56, 14.19.

Preparation of 5a

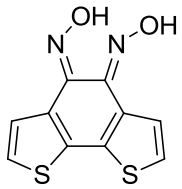

benzo[1,2-b:6,5-b']dithiophene-4,5-dione dioxime

Preparation procedure was similar to compound **3a**. Yellow solid (yield: 99%). IR ν_{max} = 3228 (s), 3182 (s), 3113 (s), 2924 (m), 1600 (m), 1291 (m), 1125 (s) cm^{-1}. High resolution EI-MS (M^+) for $C_{10}H_6N_2O_2S_2$ found: 249.9867; calcd: 249.9871. ^1H NMR (DMSO-d_6, 400 MHz): δ 14.72 (0.4H, s), 12.36 (0.7H, s), 8.19 ~ 8.17 (0.7H, d, J = 5.36 Hz), 8.02 ~ 8.01 (0.8H, d, J = 5.36 Hz), 7.60 ~ 7.59 (0.7H, d, J = 5.36 Hz), 7.59 ~ 7.57 (0.5H, d, J = 5.36 Hz), 7.53 ~ 7.52 (0.8H, d, J = 5.36 Hz), 7.48 ~ 7.46 (0.5H, d, J = 5.36 Hz); ^{13}C NMR (DMSO-d_6, 150 MHz): δ 140.93, 134.82, 132.72, 130.56, 130.21, 127.38, 126.49, 125.44, 124.16, 124.03.

Preparation of 5b

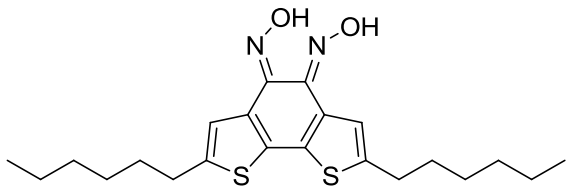

2,7-dihexylbenzo[1,2-b:6,5-b']dithiophene-4,5-dione dioxime

Preparation procedure was similar to compound **3b**. Yellow solid (yield: 95%). IR ν_{max} = 2924 (s), 2857 (s), 2691 (br, m), 1132 (m), 1055 (m), 995 (m) cm^{-1}. High resolution EI-MS (M^+) for $C_{22}H_{30}N_2O_2S_2$ found: 418.1700; calcd: 418.1749. ^1H NMR (Acetone-d_6, 600 MHz): δ 14.77 (0.5H, s), 11.94 (0.5H, s), 7.97 (1H, s), 7.22 (1H, s), 2.88 ~ 2.83 (4H, m), 1.73 ~ 1.68 (4H, m), 1.42 ~ 1.30 (12H, m), 0.90 ~ 0.88 (6H, m); ^{13}C NMR ($CDCl_3$, 100 MHz): δ 145.40, 145.13, 142.61, 141.20, 136.88, 130.73, 130.51, 127.38, 124.25, 120.72,31.61, 31.57, 31.33, 31.11, 30.28, 30.19, 28.86, 28.80, 22.63, 22.57, 14.12, 13.97.

Preparation of 6a

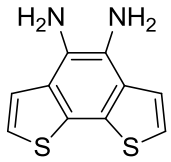

benzo[1,2-b:6,5-b']dithiophene-4,5-diamine

Preparation procedure was similar to compound **4a**. Yellow solid (yield: 71%). High resolution EI-MS (M^+) for $C_{10}H_8N_2S_2$ found: 220.0133; calcd: 220.0129. ^1H NMR (DMSO-d_6, 600 MHz): δ 7.33 ~ 7.32 (2H, d, J = 5.46 Hz), 7.31 ~ 7.30 (2H, d, J = 5.10 Hz), 3.67 (4H, br, s); ^{13}C NMR (DMSO-d_6, 150 MHz): δ 126.22, 125.36, 124.98, 123.72, 120.28.

Preparation of 6b

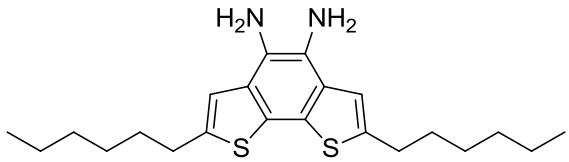

2,7-dihexylbenzo[1,2-b:6,5-b']dithiophene-4,5-diamine

Preparation procedure was similar to compound **4b**. Yellow-green solid (yield: 72%). IR ν_{max} = 2925 (s), 2857 (m), 1412 (w), 1313 (w), 836 (w) cm^{-1}. High resolution EI-MS (M^+) for $C_{22}H_{32}N_2S_2$ found: 388.2042; calcd: 388.2007. ^1H NMR ($CDCl_3$, 400 MHz): δ 6.92 (2H, s), 3.58 (4H, s, br), 2.90 ~ 2.86 (4H, t, J = 7.60 Hz), 1.77 ~ 1.70 (4H, m), 1.41

~ 1.23 (12H, m), 0.90 ~ 0.87 (6H, t, J = 6.40 Hz); ^{13}C NMR ($CDCl_3$, 150 MHz): δ 143.94, 129.59, 124.77, 124.51, 116.74, 31.58, 31.28, 30.86, 28.76, 22.55, 14.07.

Preparation of 9[17]

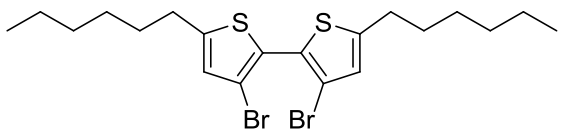

3,3'-dibromo-5,5'-dihexyl-2,2'-bithiophene

n-Butyllithium (72.4 mL, 1.6 M in hexane, 115.8 mmol) was added dropwise to the mixture of diisopropylamine (19.8 mL, 139 mmol) in anhydrous THF (80 mL) at -78 °C under N_2 gas. The mixture was stirred at -78 °C for 30 min and then the temperature was allowed to rise slowly to room temperature for 30 min. This freshly prepared LDA was added dropwise to the mixture of compound **8** (26.0 g, 105.2 mmol) in anhydrous THF (100 mL) at -78 °C under N_2 gas. The mixture was stirred at -78 °C for 1 hour and a red solution was observed. The temperature was allowed to rise slowly to -50 °C, and then $CuCl_2$ (15.6 g, 116 mmol) powder was added to the reaction, and the mixture was stirred overnight at -50 °C ~ RT. The dark green mixture was quenched with saturated aqueous NH_4Cl and a suspension was obtained. Aqueous HCl (20%) was added to the mixture until dissolution. The solution was extracted with ethyl ether (300 mL × 3) and the combined organic layers were dried over Na_2SO_4. After removing the solvent, the residue was recrystallized from methanol/ethyl acetate (2/1) at -20 °C. 22.08g of a white crystalline solid was obtained (yield: 84%). High resolution EI-MS (M^+) for $C_{20}H_{28}Br_2S_2$ found: 490.0007; calcd: 489.9999. ^{1}H NMR ($CDCl_3$, 400 MHz): δ 6.71 (2H, s), 2.76 ~ 2.72 (4H, t, J = 7.80 Hz), 1.69 ~ 1.62 (4H, m), 1.40 ~ 1.28 (12H, m), 0.89 ~ 0.87 (6H, t, J = 5.84 Hz); ^{13}C NMR ($CDCl_3$, 100 MHz): δ 147.26, 127.54, 127.37, 110.84, 31.45, 30.97, 30.13, 28.69, 22.49, 14.09.

Preparation of 11[17]

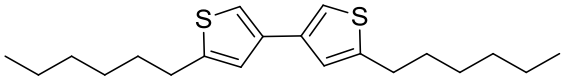

5,5'-dihexyl-3,3'-bithiophene

n-Butyllithium (84 mL, 1.6 M in hexane, 134 mmol) was added dropwise to a solution of compound **10** (26.0 g, 105.2 mmol) in anhydrous ethyl ether (200 mL) at -78 °C under N_2 gas. The mixture was stirred at -78 °C for 1 hour and then the temperature was allowed to rise slowly to -50 °C, and then $CuCl_2$ (18 g, 134 mmol) powder was added to the reaction, and the mixture was stirred overnight at -50 °C ~ RT. The dark green mixture was quenched with saturated aqueous NH_4Cl, and a suspension was obtained. Aqueous HCl (20%) was added to the mixture to dissolve the precipitate. The solution was extracted with ethyl ether (200 mL × 3) and the combined organic layers were dried over Na_2SO_4. After removing the solvent, the residue was recrystallized from methanol/ethyl acetate (2/1) at -20 °C. 10.64 g of a white solid was obtained (yield: 52%). IR ν_{max} = 2932 (s), 2857 (m), 1532 (w), 1457 (w), 792 (w) cm^{-1}. High resolution EI-MS (M^+) for $C_{20}H_{30}S_2$ found: 334.1788; calcd: 334.1789. ^1H NMR ($CDCl_3$, 400 MHz): δ 7.08 (2H, s), 6.97 (2H, s), 2.82 ~ 2.78 (4H, t, J = 7.56 Hz), 1.72 ~ 1.64 (4H, m), 1.41 ~ 1.29 (12H, m), 0.91 ~ 0.87 (6H, t, J = 7.08 Hz); ^{13}C NMR ($CDCl_3$, 100 MHz): δ 146.37, 137.11, 123.34 (× 2), 116.91 (× 2), 31.57, 30.13, 28.77, 22.56, 14.15, 13.99.

Preparation of *t*-TTP

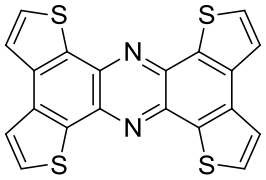

tetrathieno[2,3-a:3',2'-c:2'',3''-h:3''',2'''-j]phenazine

Benzo[1,2-b:4,3-b']dithiophene-7,8-quinone (0.29 g, 1.3 mmol) and compound **4a** (0.29 g, 1.3 mmol) in ethanol (10.0 mL) were refluxed for 16 h. The reaction mixture was cooled to RT, filtered and washed with ethanol. The filter cake was dried in the desiccator to afford an orange crude powder (0.42 g). The crude product was sublimed

(280 ^{o}C) to obtain 310 mg of an orange crystalline solid. The crystals were of suitable quality to be used for X-Ray characterization. NMR data is not available due to poor solubility. IR ν_{max} = 3097 (m), 1532 (m), 1404 (s), 1344 (m), 1214 (m), 723 (m) cm^{-1}. High resolution EI-MS (M^+) for $C_{20}H_8N_2S_4$ found: 403.9565; calcd: 403.9570. Elemental analysis (%) for $C_{20}H_8N_2S_4$ found: C 59.24, H 2.03, N 6.68; calcd: C 59.38, H 1.99, N 6.92.

Preparation of *l*-TTP

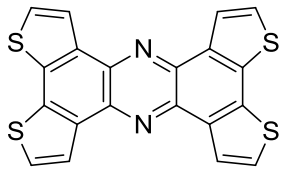

tetrathieno[3,2-a:2',3'-c:3'',2''-h:2''',3'''-j]phenazine

Preparation procedure was similar to compound ***t*-TTP**. Crystals suitable for X-Ray characterization were obtained. Red solid (yield: 53%). NMR data is not available due to poor solubility. IR ν_{max} = 3111 (m), 1495 (m), 1411 (m), 1312 (m), 1214 (m), 723 (s) cm^{-1}. High resolution EI-MS (M^+) for $C_{20}H_8N_2S_4$ found: 403.9568; calcd: 403.9570. Elemental analysis (%) for $C_{20}H_8N_2S_4$ found: C 59.30, H 1.88, N 6.51; calcd: C 59.38, H 1.99, N 6.92.

Preparation of *m*-TTP

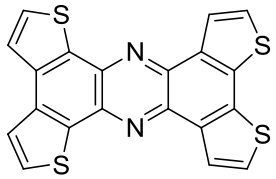

tetrathieno[2,3-a:3',2'-c:3'',2''-h:2''',3'''-j]phenazine

Preparation procedure was similar to compound ***t*-TTP**. Yellow solid (yield: 41%). NMR data was not available due to poor solubility. IR ν_{max} = 3090 (m), 1510 (m), 1404 (s), 1312 (s), 723 (s) cm^{-1}. High resolution EI-MS (M^+) for $C_{20}H_8N_2S_4$ found: 403.9567; calcd: 403.9570. Elemental analysis (%) for $C_{20}H_8N_2S_4$ found: C 59.38, H 1.81, N 6.54; calcd: C 59.38, H 1.99, N 6.92.

Preparation of *t*-HTTP

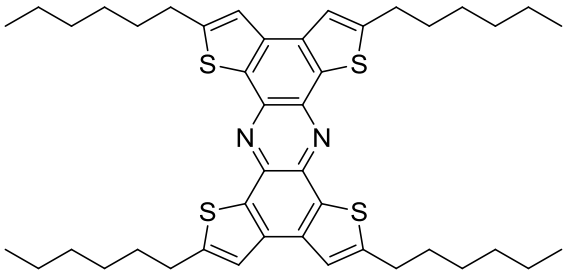

2,5,9,12-tetrahexyltetrathieno[2,3-a:3',2'-c:2'',3''-h:3''',2'''-j]phenazine

Compound **3b** (0.160 g, 0.41 mmol) and compound **4b** (0.165 g, 0.42 mmol) in ethanol (20.0 mL) were refluxed for 48 h. The reaction mixture was cooled to RT, filtered and washed with methanol (10.0 mL). The filter cake was dried in the desiccator to afford a yellow solid (0.12 g, 40%). IR ν_{max} = 2924 (s), 2857 (m), 1412 (m), 966 (w), 814 (w) cm^{-1}. High resolution EI-MS (M^+) for $C_{44}H_{56}N_2S_4$ found: 740.3322; calcd: 740.3326. ^1H NMR ($CDCl_3$, 600 MHz): δ 7.36 (4H, s), 3.06 ~ 3.03 (8H, t, J = 7.53 Hz), 1.88 ~ 1.84 (8H, m), 1.47 ~ 1.35 (24H, m), 0.92 ~ 0.90 (12H, t, J = 6.78 Hz); ^{13}C NMR ($CDCl_3$, 150 MHz): δ 150.96, 136.87, 135.94, 133.39, 119.93, 31.63, 31.54, 31.14, 28.85, 22.59, 14.10. Elemental analysis (%) for $C_{44}H_{56}N_2S_4$ found: C 70.73, H 7.49, N 3.56; calcd: C 71.30, H 7.62, N 3.78.

Preparation of *l*-HTTP

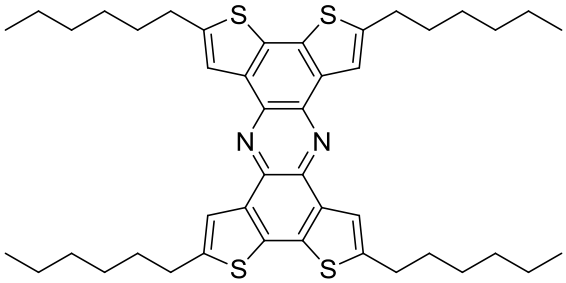

2,5,9,12-tetrahexyltetrathieno[3,2-a:2',3'-c:3'',2''-h:2''',3'''-j]phenazine

Preparation procedure was similar to compound ***t*-HTTP**. Yellow solid (yield: 75%). IR ν_{max} = 2924 (s), 2857 (m), 1419 (w), 1223 (w), 836 (w) cm^{-1}. High resolution EI-MS (M^+) for $C_{44}H_{56}N_2S_4$ found: 740.3321; calcd: 740.3326. ^1H NMR ($CDCl_3$, 600 MHz): δ 8.17 (4H, s), 3.08 ~ 3.05 (8H, t, J = 7.68 Hz), 1.90 ~ 1.85 (8H, m), 1.54 ~ 1.34 (24H, m), 0.94 ~ 0.91 (12H, t, J = 7.14 Hz); ^{13}C NMR ($CDCl_3$, 150 MHz): δ 144.93, 137.10,

134.53, 134.86, 121.24, 31.65, 31.62, 30.82, 28.89, 22.60, 14.11. Elemental analysis (%) for $C_{44}H_{56}N_2S_4$ found: C 71.11, H 7.44, N 3.59; calcd: C 71.30, H 7.62, N 3.78.

Preparation of *m*-HTTP

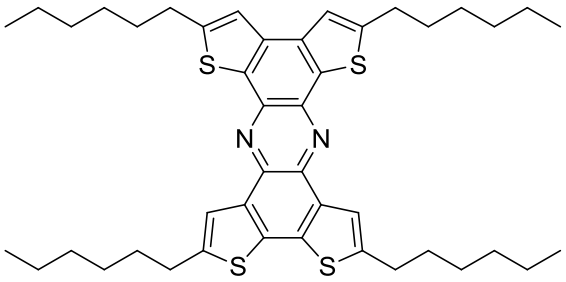

2,5,9,12-tetrahexyltetrathieno[2,3-a:3',2'-c:3'',2''-h:2''',3'''-j]phenazine

Preparation procedure was similar to compound ***t*-HTTP**. Yellow solid (yield: 56%). IR ν_{max} = 2924 (s), 2850 (m), 1518 (w), 1412 (w), 814 (w) cm^{-1}. High resolution EI-MS (M^+) for $C_{44}H_{56}N_2S_4$ found: 740.3325; calcd: 740.3326. ^1H NMR ($CDCl_3$, 400 MHz): δ 8.13 (2H, s), 7.42 (2H, s), 3.09 ~ 3.03 (8H, m), 1.90 ~ 1.84 (8H, m), 1.56 ~ 1.36 (24H, m), 0.93 ~ 0.90 (12H, m); ^{13}C NMR ($CDCl_3$, 100 MHz): δ 150.78, 144.87, 137.15, 136.81, 136.00, 134.25, 133.76, 133.67, 121.32, 120.02, 31.69, 31.64, 31.59, 31.16, 30.79, 28.90, 28.86, 22.67, 22.63, 22.60, 14.19, 14.04. Elemental analysis (%) for $C_{44}H_{56}N_2S_4$ found: C 71.19, H 7.52, N 3.61; calcd: C 71.30, H 7.62, N 3.78.

Crystal growth and X-ray analysis

Crystal of ***t*-TTP** were obtained by slowly evaporation of the DCM solution or sublimation at 280 °C ~ 290 °C, and the crystal parameters obtained by these two methods were the same. Crystals of ***m*-TTP** were grown by slow cooling saturated benzonitrile solution from 160 °C ~ 90 °C. Crystals of ***l*-TTP** were obtained by sublimation at 300 °C ~ 320 °C. Crystals of ***l*-HTTP** were grown by slowly evaporating a DCM solution. Crystals of ***m*-HTTP** and ***t*-HTTP** could not be obtained under various conditions. Crystals were mounted on a loop using oil (CryoLoop, Immersion Oil, Type B; Hampton Research Corp.) and set on a Rigaku RA-Micro007 with a Saturn CCD detector using graphite-monochromated Mo *K*α radiation (λ = 0.710690 Å) under a cold nitrogen steam. The frame data were integrated and corrected for absorption with the Rikagu/MSC CrystalClear package.[18] The structures were

solved by direct methods[19] and standard difference map techniques, and were refined with full-matrix least-square procedures on F^2 by a Rikagu/MSC CrystalStructure package. Anisotropic refinement was applied to all non-hydrogen atoms. All hydrogen atoms were placed at calculated positions and refined using a riding model.

Theoretical calculations

The molecular orbital calculations based on density functional theory were carried out using the Gaussian09, revision C.01 program package.[15] The molecular structures were optimized using HF and B3LYP[20] methods with 6-31G(d) basis sets.

Intermolecular hopping carrier mobilities were calculated on the basis of Marcus theory.[16] First, intermolecular electronic coupling matrix elements (V) were calculated with equation 1 using intermolecular charge transfer integrals (H_{ab}), overlap integrals (S_{ab}), and the energies of the two molecular orbitals (H_{aa} and H_{bb}) calculated at PW91/TZ2P level using the ADF 2012 program package.

$$V = \frac{H_{ab} - S_{ab}(H_{aa} - H_{bb})/2}{1 - S_{ab}^2} \qquad (1)$$

Then the intermolecular charge transfer rate constants (k_{ET}) were evaluated from equation 2.

$$k_{ET} = \frac{V^2}{h}\left(\frac{\pi}{\lambda k_B T}\right)^{1/2} \exp\left(-\frac{\lambda}{4k_B T}\right) \qquad (2)$$

Where, h, k_B, and T are Planck's constant, Boltzmann constant, and temperature, respectively. The reorganization energies upon intermolecular hole transfer (λ) were obtained from $\lambda = (E^{+*} - E^{+}) + (E^{*} - E)$. Where, E, E^{+}, E^{*}, and E^{+*} were the heat of formations for an optimized neutral molecule, optimized cation molecule, neutral state on cation structure, and cation state on neutral structure, respectively, calculated at B3LYP/6-31G(d) level. Intermolecular hopping mobilities (μ) were estimated from the following equation (3).

$$\mu_{hopping} = \frac{ed^2}{k_B T} k_{ET} \qquad (3)$$

Where, d is the intermolecular center-to-center distances of adjacent molecules.

Thin-film X-ray analysis

X-ray diffractions of vapor deposited thin films on bare Si substrates were obtained by Rikagu Smartlab X-ray diffractometer with a Cu *K*α source (λ = 1.541 Å) in air. The calculated inter-layer distances (*d*-spacing) are listed in Table 2-4 in the main text.

Fabrication of the thin-film transistors

Thin films were deposited on Pt electrode with a gap of 2 μm over a 2 × 2mm area (corresponding to 2 μm gap and 1 m width) as source/drain electrodes (bottom-contact) patterned on n-doped silicon substrates covered with 300nm-thick SiO_2 layer. Prior to deposition, the substrates were cleaned by sonication in acetone and isopropyl alcohol followed by exposure to O_2 plasma. Films were deposited by vacuum sublimation (pressure ~ 5×10^{-4} Pa) at a deposition rate 0.2 ~ 1.2 Å/s until a thickness of 100 nm was reached. Organic field-effect transistor measurements were carried out in a vacuum with a Keithley 2636A dual channel source meter. The field-effect mobility (μ_{FET}) was calculated in the linear region of transfer curves.

Conductivity measurements upon chemical doping

The electrical conductivity of the thin-films was measured by dc two-probe method utilizing the substrates from FET measurements. The conductivity measurements on crystalline samples were carried out by connecting gold wires at the opposed edges of the crystal with gold paste. The sample was placed in a glass chamber with a nitrogen atmosphere and iodine vapor was gradually introduced into the chamber through a valve. In each case, 1V of constant voltage was applied to the sample and the current was recorded with Keithley 487 picoammeter upon iodine doping.

2.5 Appendix

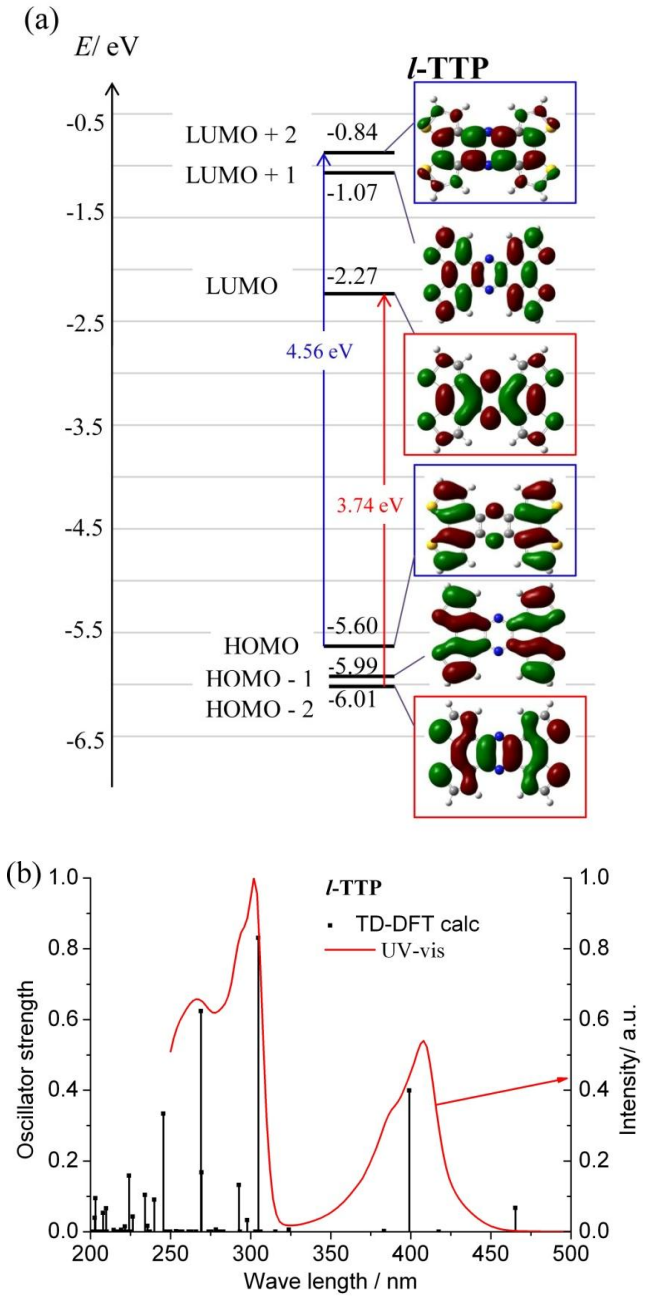

Observed absorption band (λ_{max})	Calculated by TD-DFT	Assigned transition	Energy difference	Contribution	Oscillator strength (f)
302 nm	286 nm	HOMO→LUMO + 2	4.56 eV	0.24	0.831
		HOMO - 2→LUMO	3.74 eV	0.64	
408 nm	375 nm	HOMO→LUMO + 2	4.56 eV	0.62	0.399
		HOMO - 2→LUMO	3.74 eV	-0.16	

Fig. 2-17. (a) Energy diagram and distributions of frontier orbitals of ***l*-TTP** accompanied with the assignment of optical transitions. (b) UV-vis spectrum of ***l*-TTP** (red line) in $CHCl_3$ accompanied with a simulated transitions (black line) calculated by TD-DFT method (B3LYP/6-31G (d)). Scalling factor is 0.94.

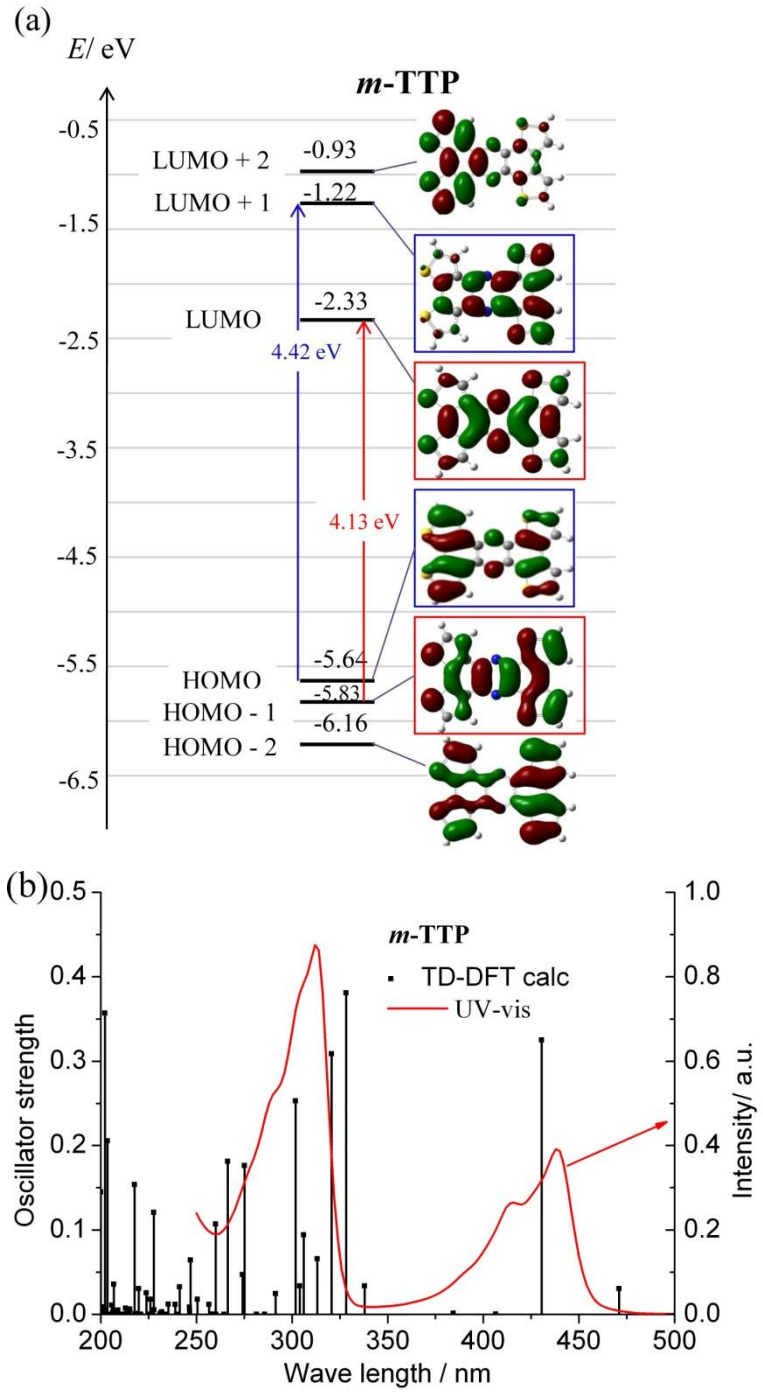

Observed absorption band (λ_{max})	Calculated by TD-DFT	Assigned transition	Energy difference	Contribution	Oscillator strength (*f*)
312 nm	309 nm	HOMO→LUMO + 1	4.42 eV	0.58	0.381
		HOMO - 1→LUMO	4.13 eV	-0.12	
439 nm	405 nm	HOMO→LUMO + 1	4.42 eV	0.22	0.325
		HOMO - 1→LUMO	4.13 eV	0.64	

Fig. 2-18**.** (a) Energy diagram and distributions of frontier orbitals of ***m*-TTP** accompanied with the assignment of optical transitions. (b) UV-vis spectrum of ***m*-TTP** (red line) in $CHCl_3$ accompanied with a simulated transitions (black line) calculated by TD-DFT method (B3LYP/6-31G (d)). Scalling factor is 0.94.

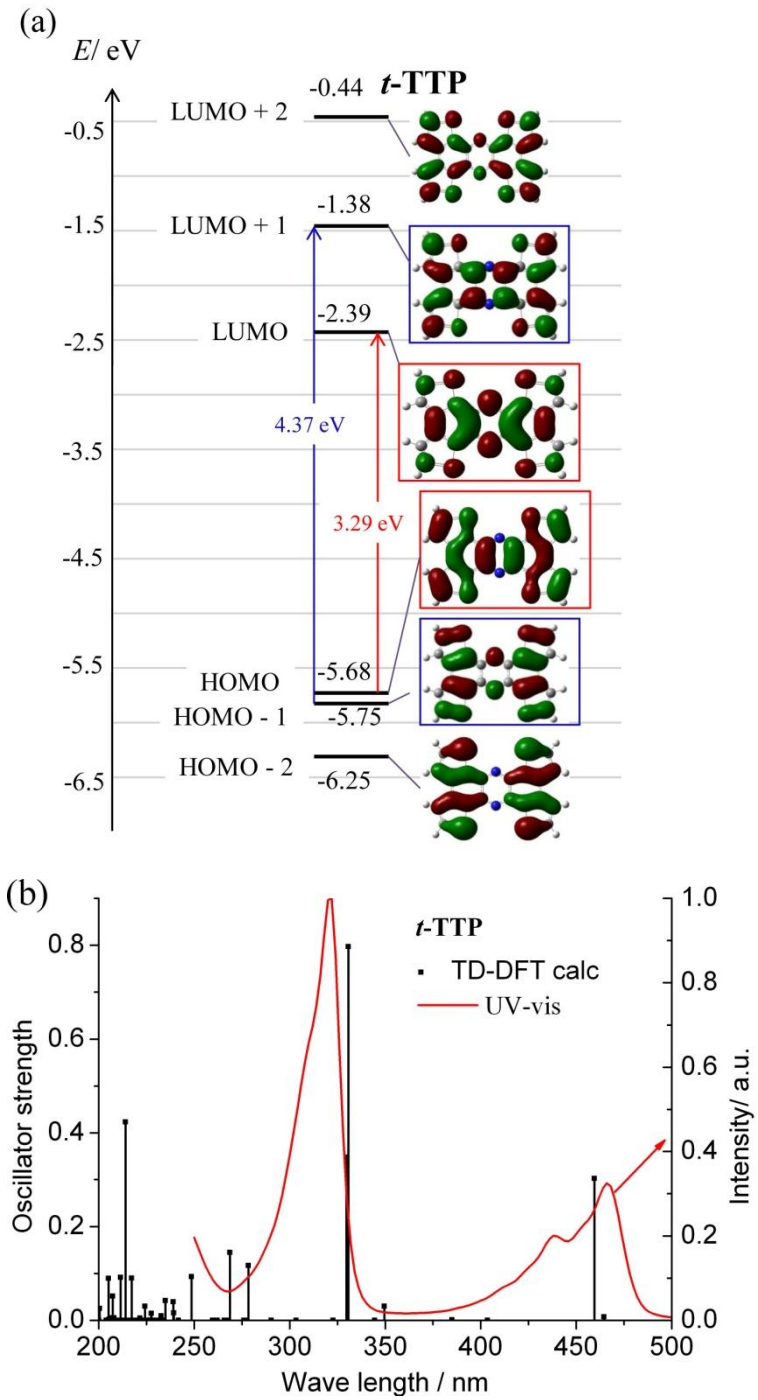

Observed absorption band (λ_{max})	Calculated by TD-DFT	Assigned transition	Energy difference	Contribution	Oscillator strength (*f*)
320 nm	311 nm	HOMO - 1→LUMO + 1	4.37 eV	0.63	0.797
		HOMO→LUMO	3.29 eV	0.13	
467 nm	432 nm	HOMO - 1→LUMO + 1	4.37 eV	-0.22	0.302
		HOMO→LUMO	3.29 eV	0.64	

Fig. 2-19**. *t*-TTP**: (a) Energy diagram and distributions of frontier orbitals of ***t*-TTP** accompanied with the assignment of optical transitions. (b) UV-vis spectrum of ***t*-TTP** (red line) in $CHCl_3$ accompanied with a simulated transitions (black line) calculated by TD-DFT method (B3LYP/6-31G (d)). Scalling factor is 0.94.

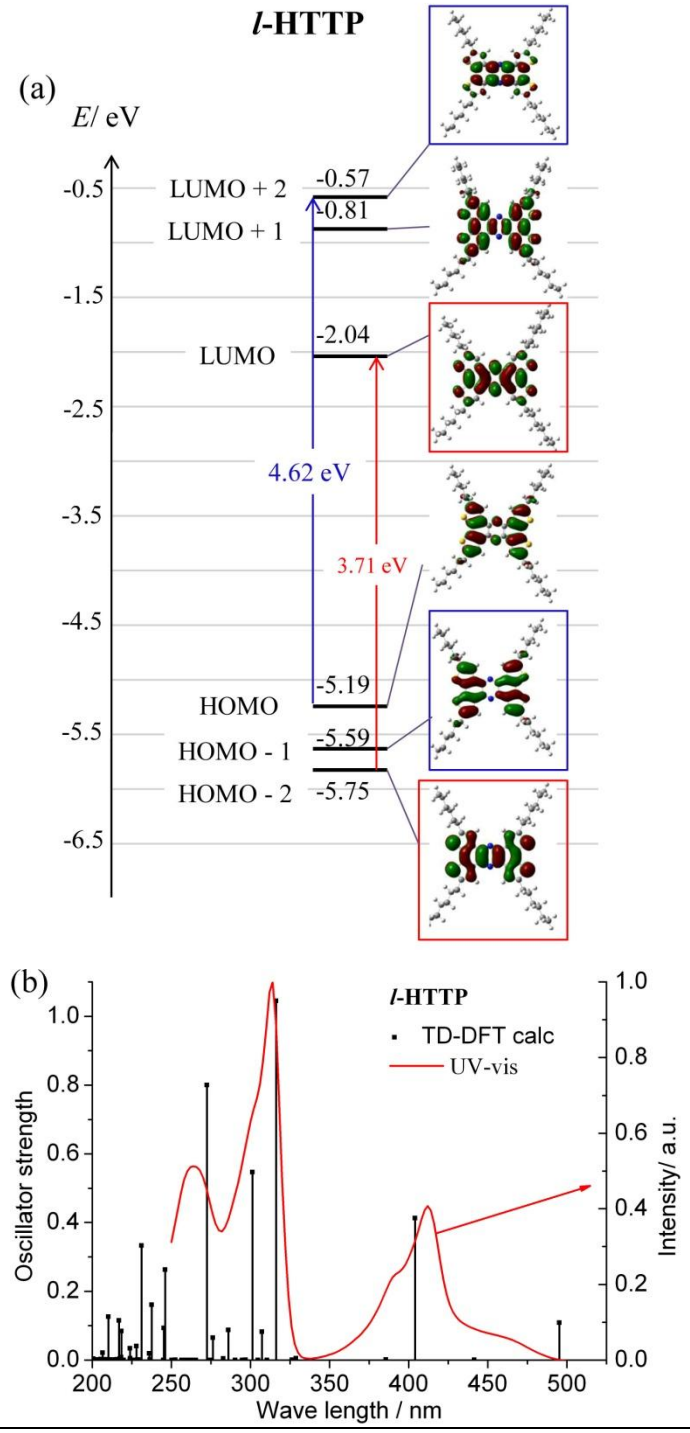

Observed absorption band (λ_{max})	Calculated by TD-DFT	Assigned transition	Energy difference	Contribution	Oscillator strength (*f*)
313 nm	296 nm	HOMO→LUMO + 2	4.62 eV	0.61	0.900
		HOMO - 2→LUMO	3.71 eV	0.17	
422 nm	380 nm	HOMO→LUMO + 2	4.62 eV	-0.25	0.378
		HOMO - 2→LUMO	3.71 eV	0.64	

Fig. 2-20**.** (a) Energy diagram and distributions of frontier orbitals of ***l*-HTTP** accompanied with the assignment of optical transitions. (b) UV-vis spectrum of ***l*-HTTP** (red line) in $CHCl_3$ accompanied with a simulated transitions (black line) calculated by TD-DFT method (B3LYP/6-31G (d)). Scalling factor is 0.94.

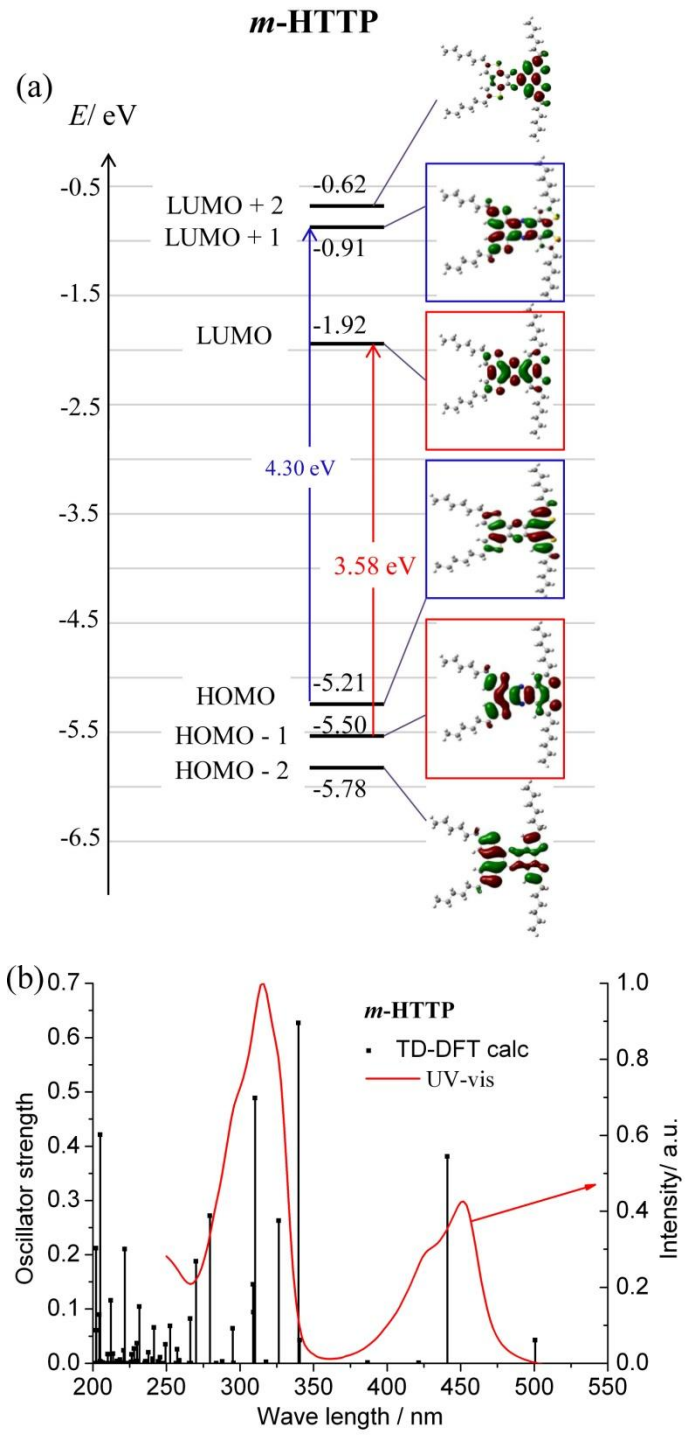

Observed absorption band (λ_{max})	Calculated by TD-DFT	Assigned transition	Energy difference	Contribution	Oscillator strength (*f*)
315 nm	319 nm	HOMO→LUMO + 1	4.30 eV	0.62	0.627
		HOMO - 1→LUMO	3.58 eV	0.13	
451 nm	414 nm	HOMO→LUMO + 1	4.30 eV	-0.21	0.381
		HOMO - 1→LUMO	3.58 eV	0.64	

Fig. 2-21. (a) Energy diagram and distributions of frontier orbitals of ***m*-HTTP** accompanied with the assignment of optical transitions. (b) UV-vis spectrum of ***m*-HTTP** (red line) in $CHCl_3$ accompanied with a simulated transitions (black line) calculated by TD-DFT method (B3LYP/6-31G (d)). Scalling factor is 0.94.

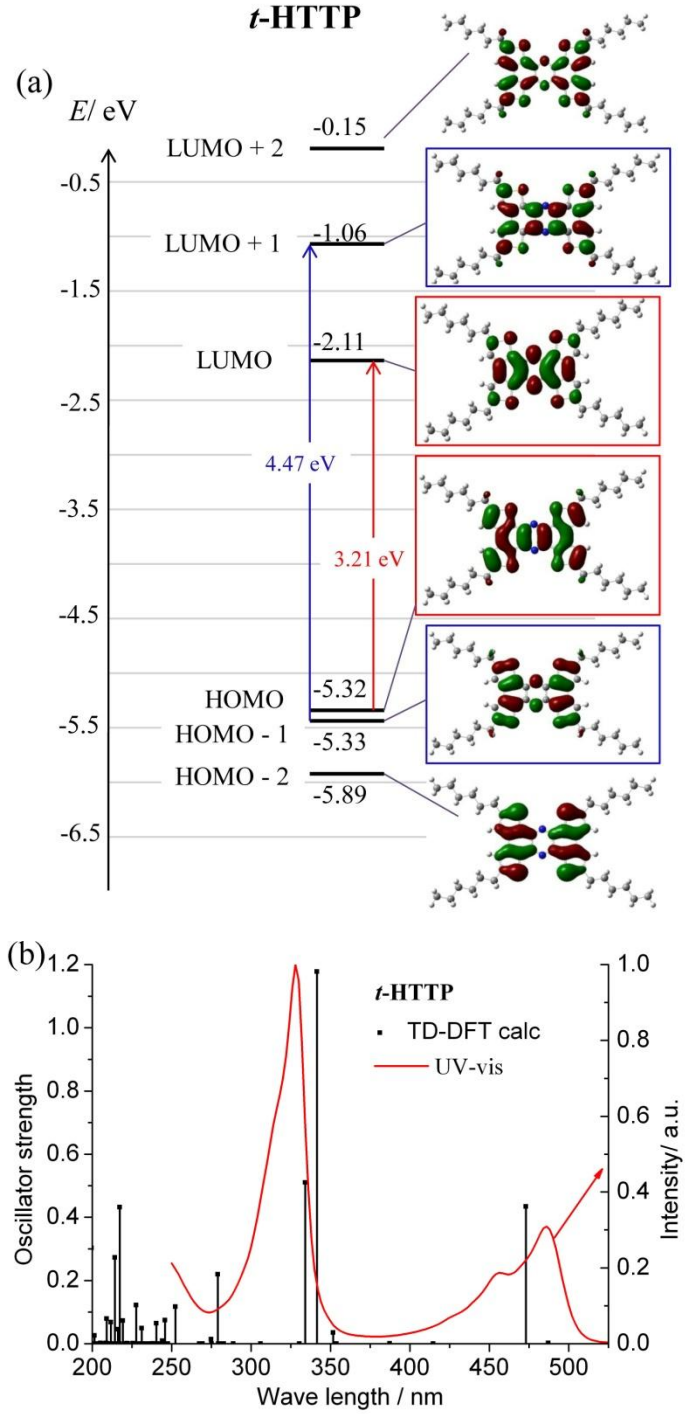

Observed absorption band (λ_{max})	Calculated by TD-DFT	Assigned transition	Energy difference	Contribution	Oscillator strength (*f*)
328 nm	321 nm	HOMO - 1→LUMO + 1	4.47 eV	0.64	1.178
		HOMO→LUMO	3.21 eV	0.13	
486 nm	445 nm	HOMO - 1→LUMO + 1	4.47 eV	-0.21	0.434
		HOMO→LUMO	3.21 eV	0.64	

Fig. 2-22. (a) Energy diagram and distributions of frontier orbitals of ***t*-HTTP** accompanied with the assignment of optical transitions. (b) UV-vis spectrum of ***t*-HTTP** (red line) in $CHCl_3$ accompanied with a simulated transitions (black line) calculated by TD-DFT method (B3LYP/6-31G (d)). Scalling factor is 0.94.

***l*-TTA**

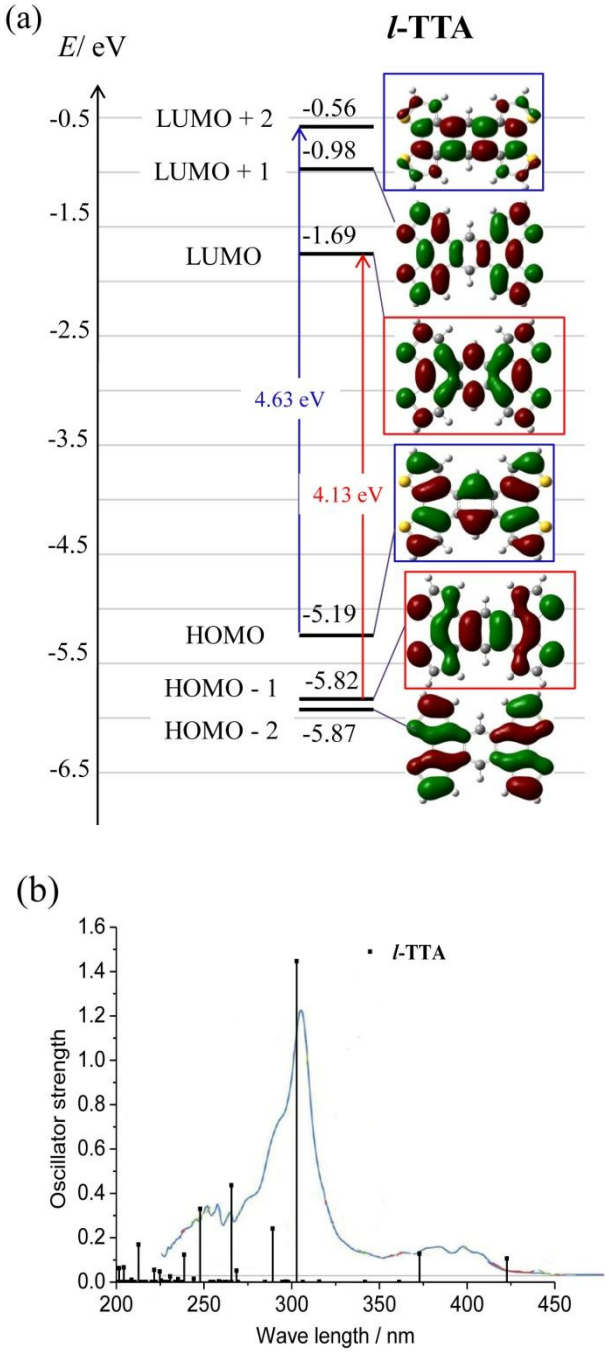

Observed absorption band (λ_{max})	Calculated by TD-DFT	Assigned transition	Energy difference	Contribution	Oscillator strength (*f*)
300 nm(strong)	286 nm	HOMO→LUMO + 2	4.63 eV	0.59	1.446
		HOMO - 1→LUMO	4.13 eV	0.35	
479 nm(weak)	350 nm	HOMO→LUMO + 2	4.63 eV	-0.35	0.127
		HOMO - 1→LUMO	4.13 eV	0.61	

Fig. 2-23**. *l*-TTA**: (a) Energy diagram and distributions of frontier orbitals of ***l*-TTA** accompanied with the assignment of optical transitions. (b) UV-vis spectrum of ***l*-TTA** (blue line: reference 8) in DCM accompanied with a simulated transitions (black line) calculated by TD-DFT method (B3LYP/6-31G (d)). Scalling factor is 0.94.

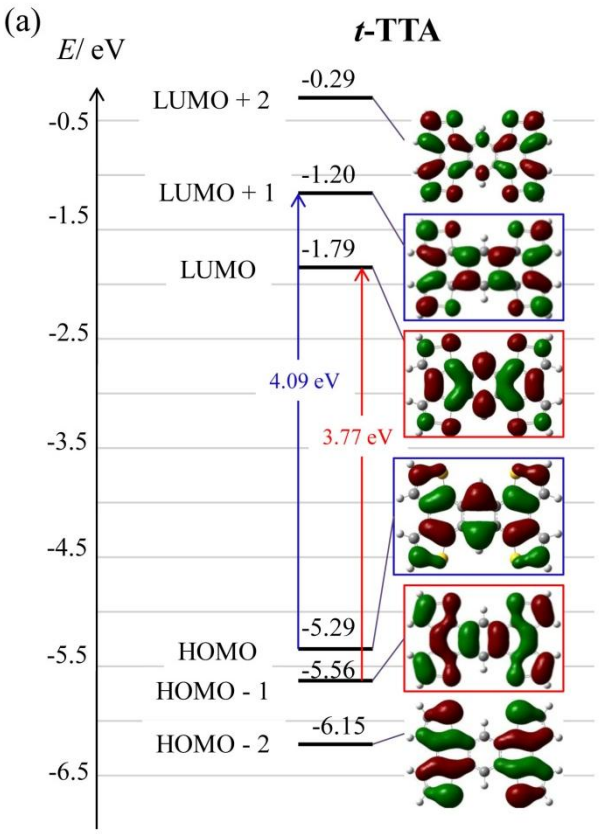

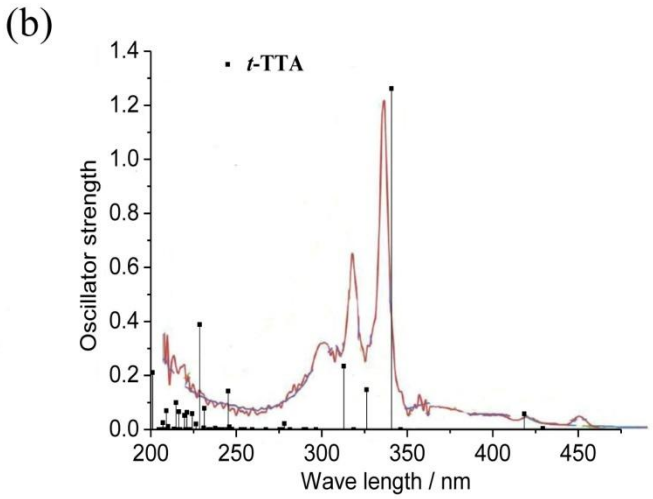

Observed absorption band (λ_{max})	Calculated by TD-DFT	Assigned transition	Energy difference	Contribution	Oscillator strength (f)
310 nm (strong)	320 nm	HOMO→LUMO + 1	4.09 eV	0.60	1.262
		HOMO - 1→LUMO	3.77 eV	-0.37	
418 nm (weak)	393 nm	HOMO→LUMO + 1	4.09 eV	0.37	0.058
		HOMO - 1→LUMO	3.77 eV	0.60	

Fig. 2-24. ***t*-TTA**: (a) Energy diagram and distributions of frontier orbitals of ***t*-TTA** accompanied with the assignment of optical transitions. (b) UV-vis spectrum of ***t*-TTA** (purple line: reference 8) in DCM accompanied with a simulated transitions (black line) calculated by TD-DFT method (B3LYP/6-31G (d)). Scalling factor is 0.94.

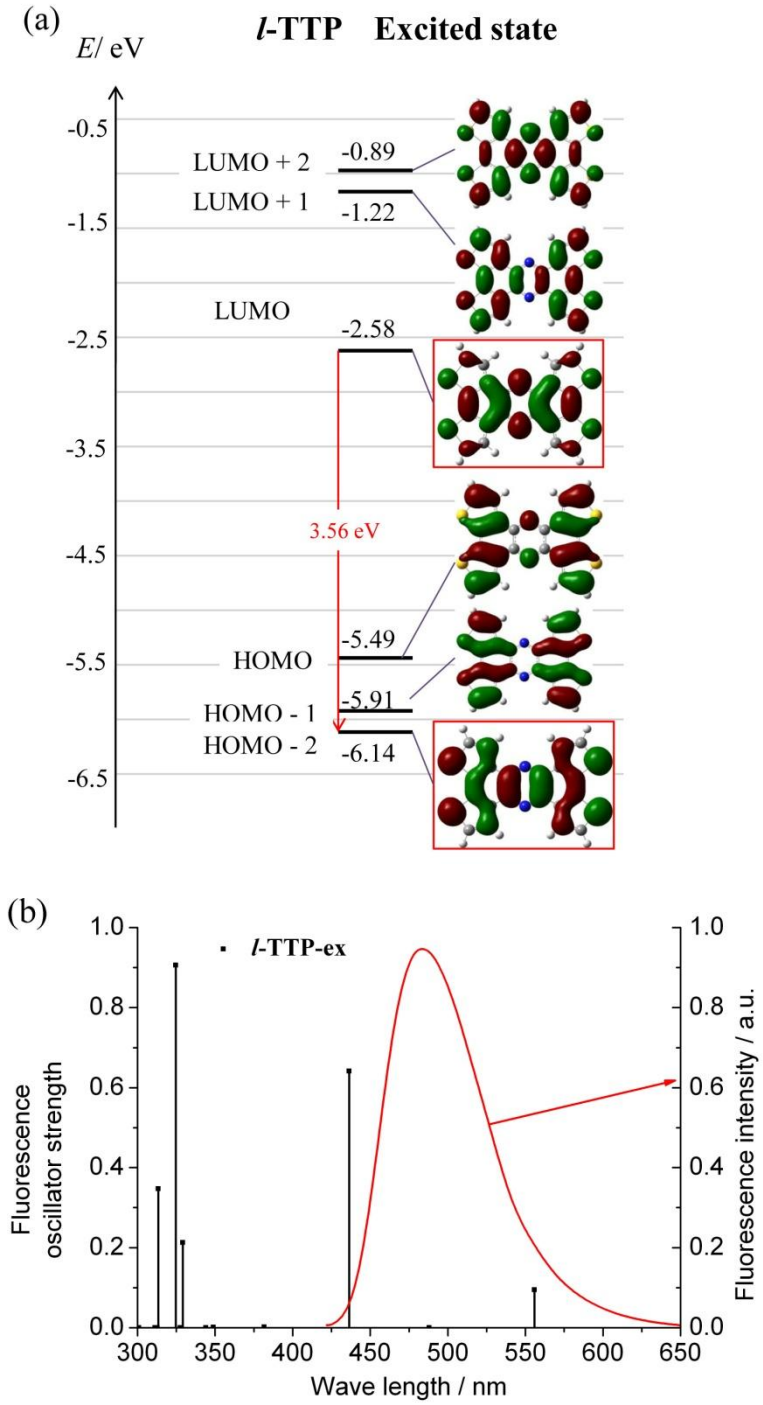

Observed absorption band (λ_{max})	Calculated by TD-DFT	Assigned transition	Energy difference	Contribution	Oscillator strength (*f*)
480 nm	410 nm	LUMO→HOMO - 2	3.56 eV	0.69	0.642
		LUMO + 3→HOMO	---	-0.15	

Fig. 2-25. (a) Energy diagram and spatial distributions of frontier orbitals of an excited state of ***l*-TTP** accompanied with the assignment of photoluminescence transition. (b) Observed fluorescence spectrum (red line) of in CHCl3 solution (λ_{ex} = 303 nm) and simulated spectrum (black line) with TD-DFT method (B3LYP/6-31G (d)). Scalling factor is 0.94.

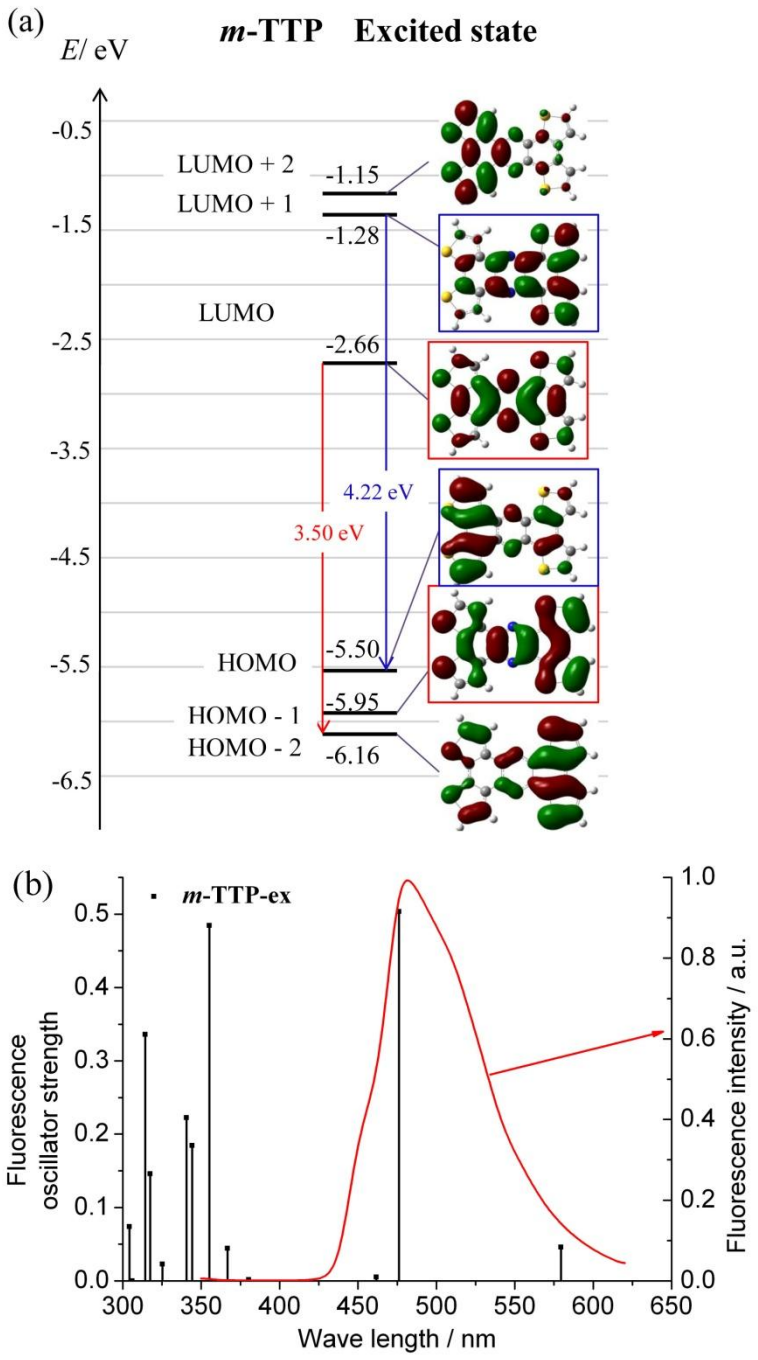

Observed absorption band (λ_{max})	Calculated by TD-DFT	Assigned transition	Energy difference	Contribution	Oscillator strength (f)
481 nm	448 nm	LUMO→HOMO - 1	3.50 eV	0.69	0.503
		LUMO + 1→HOMO	4.22 eV	-0.12	

Fig. 2-26**.** (a) Energy diagram and spatial distributions of frontier orbitals of an excited state of ***m*-TTP** accompanied with the assignment of photoluminescence transition. (b) Observed fluorescence spectrum (red line) of in $CHCl_3$ solution (λ_{ex} = 316 nm) and simulated spectrum (black line) with TD-DFT method (B3LYP/6-31G (d)). Scalling factor is 0.94.

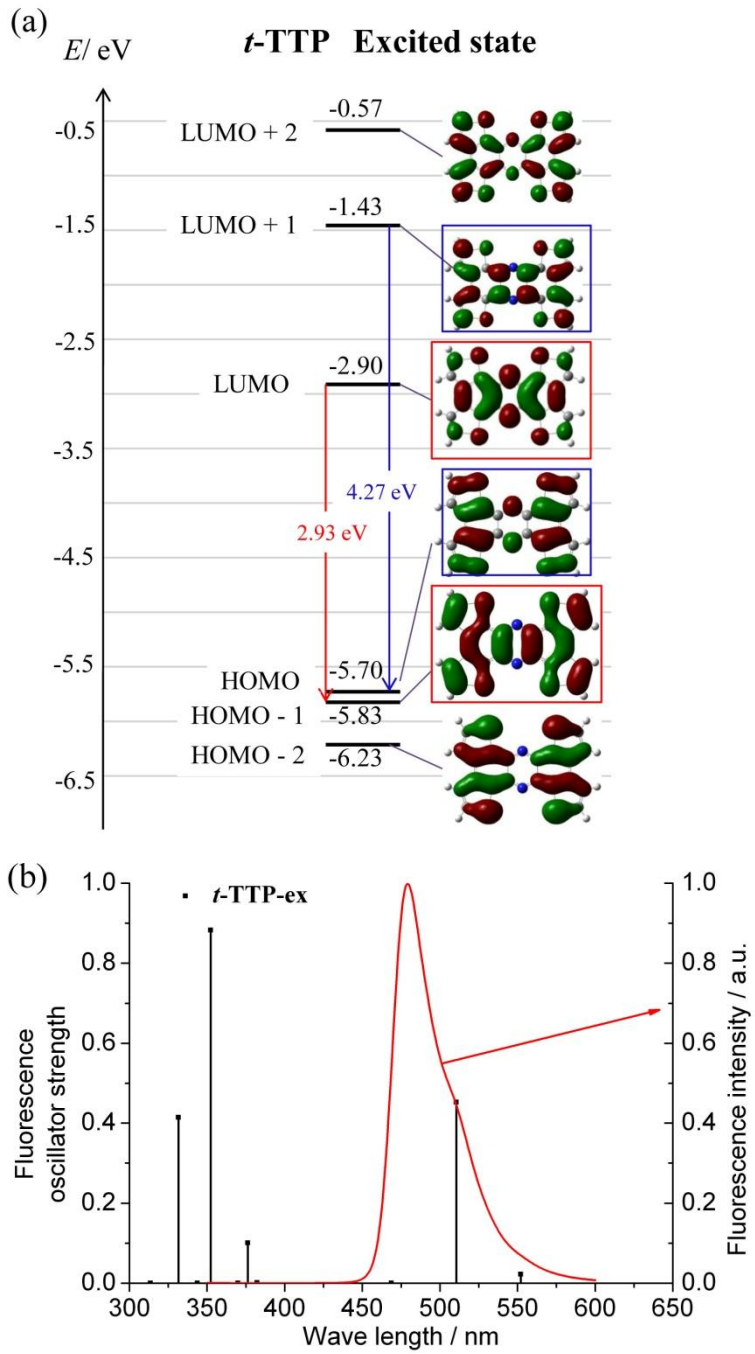

Observed absorption band (λ_{max})	Calculated by TD-DFT	Assigned transition	Energy difference	Contribution	Oscillator strength (*f*)
481 nm	480 nm	LUMO→HOMO - 1	2.93 eV	0.70	0.453
		LUMO + 1→HOMO	4.27 eV	-0.12	

Fig. 2-27. (a) Energy diagram and spatial distributions of frontier orbitals of an excited state of ***t*-TTP** accompanied with the assignment of photoluminescence transition. (b) Observed fluorescence spectrum (red line) of in $CHCl_3$ solution (λ_{ex} = 322 nm) and simulated spectrum (black line) with TD-DFT method (B3LYP/6-31G (d)). Scalling factor is 0.94.

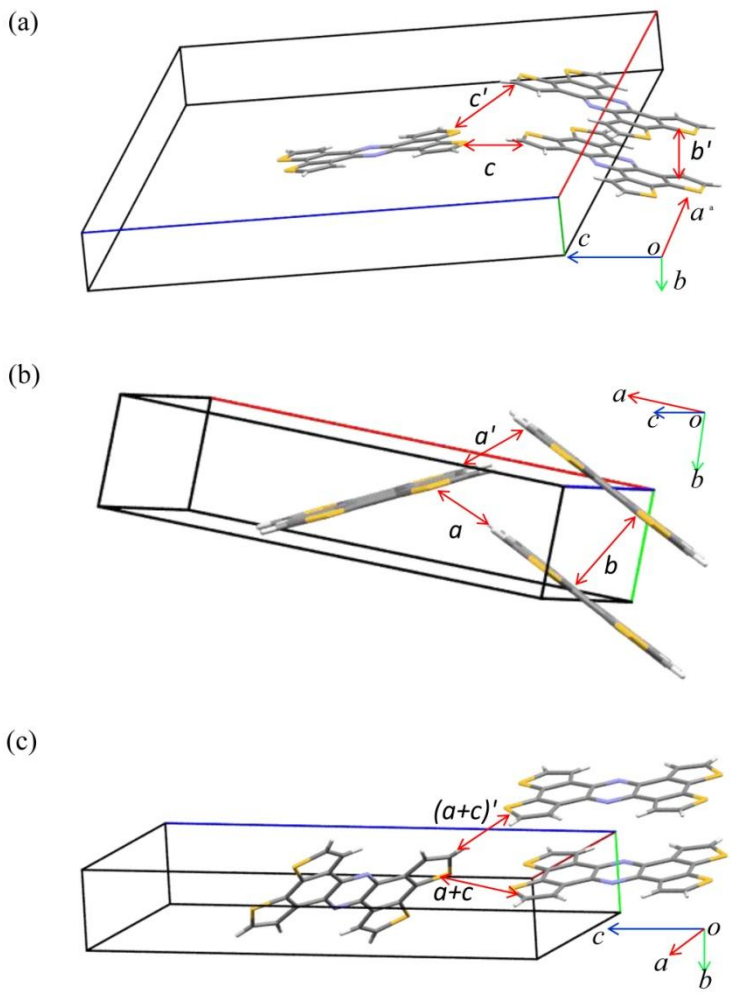

Fig. 2-28**.** Effective intermolecular contacts in ***l*-TTP** crystal along *b*-axis (a), *b*-axis (b) and a + c direction (c).

Table 2-7. Theoretically estimated intermolecular transfer intergrals (*Hab*), overlap intergrals (*Sab*), center-to-center distances (*d*), orbital interaction energy (*V*), reorganization energy (λ) and hopping mobilities for each molecular contact.

	Contact[a]	*Hab*[b] /meV	*Sab*[b]	*d* /Å	*V* /meV	λ [c] / meV	$\mu_{hopping}$ / $cm^2\ V^{-1}\ S^{-1}$
***l*-TTP**	*b*	-135.4	11.2	3.892	-76.5	153	5.3×10^{-1}
***l*-TTP**	*a*	7.7	-0.7	8.748	.3.6	153	6.1×10^{-3}
***l*-TTP**	*c*	-8.9	-0.9	13.001	-.4.0	153	1.7×10^{-2}
***l*-TTP**	*c'*	14.47	-1.6	13.002	.5.9	153	3.5×10^{-2}
***l*-TTP**	*a+c*	-1.5	0.2	12.934	-.0.6	153	4.0×10^{-4}
***l*-TTP**	*(a+c)'*	3.2	-0.3	13.507	.1.6	153	2.9×10^{-3}
***l*-TTP**	*b'*	-162.4	13.9	3.892	-.91.3	153	7.6×10^{-1}

[a] Corresponding molecular contacts are indicated in Fig. 2-28. [b] Calculated in PW91/TZ2P level. [c] Calculated in B3LYP/6-31G(d) level.

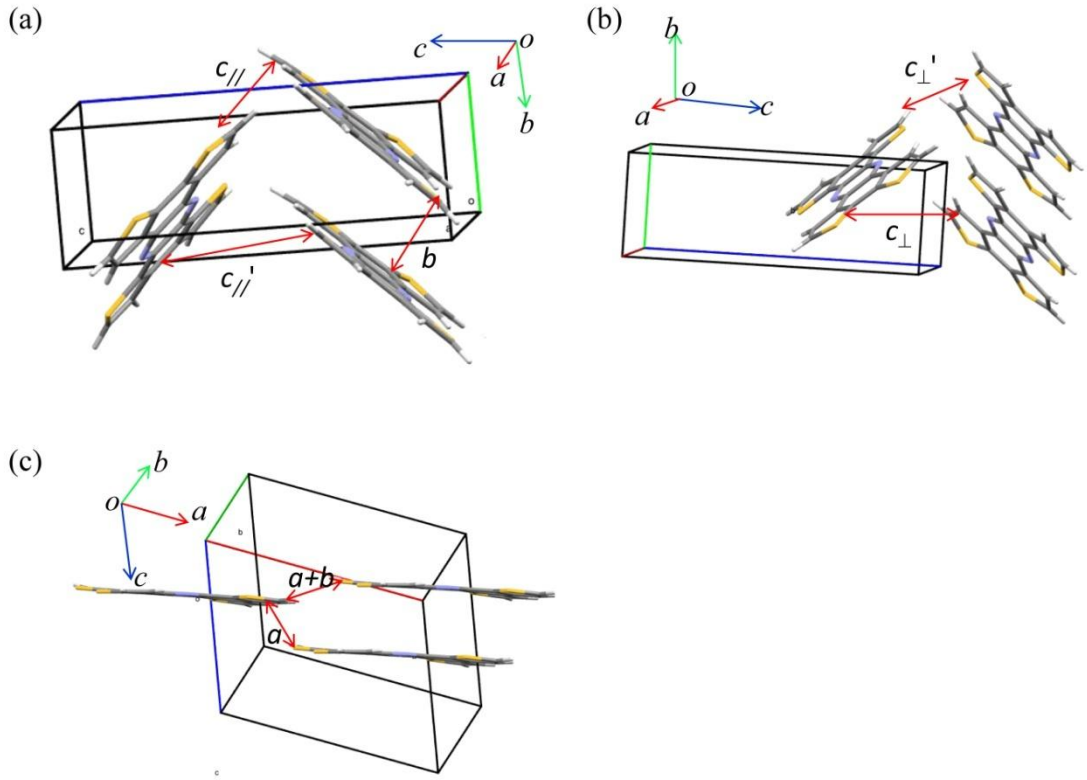

Fig. 2-29**.** Effective intermolecular contacts in ***m*-TTP** crystal along *c*-axis (a), *a*-axis (b) and a + c direction (c).

Table 2-8. Theoretical estimated intermolecular transfer intergrals (*Hab*), overlap intergrals (*Sab*), center-to-center distances (*d*), orbital interaction energy (*V*), reorganization energy (λ) and hopping mobilities for each molecular contact.

	Contac	Hab^b /meV	Sab^b	*d* /Å	*V*	λ^c / meV	$\mu_{hopping}$ / $cm^2\ V^{-1}\ S^{-1}$
***m*-TTP**	*a*	-0.7	0.1	12.581	-0.3	169	8.9×10^{-5}
***m*-TTP**	*a*+*b*	0.4	0	13.474	0.2	169	4.0×10^{-5}
***m*-TTP**	*b*	-133.3	12.9	4.825	-66.5	169	5.0×10^{-1}
***m*-TTP**	$c_{//}$	-1.0	0	7.857	-1.1	169	3.7×10^{-4}
***m*-TTP**	$c_{//}$'	-1.8	0	7.857	-1.9	169	1.1×10^{-3}
***m*-TTP**	$c_{\perp}$	25.9	-2.6	11.941	11.7	169	9.5×10^{-2}
***m*-TTP**	$c_{\perp}$'	25.7	-2.7	11.941	11.5	169	9.2×10^{-2}

[a] Corresponding molecular contacts are indicated in Fig. 2-29. [b] Calculated in PW91/TZ2P level. [c] Calculated in B3LYP/6-31G(d) level.

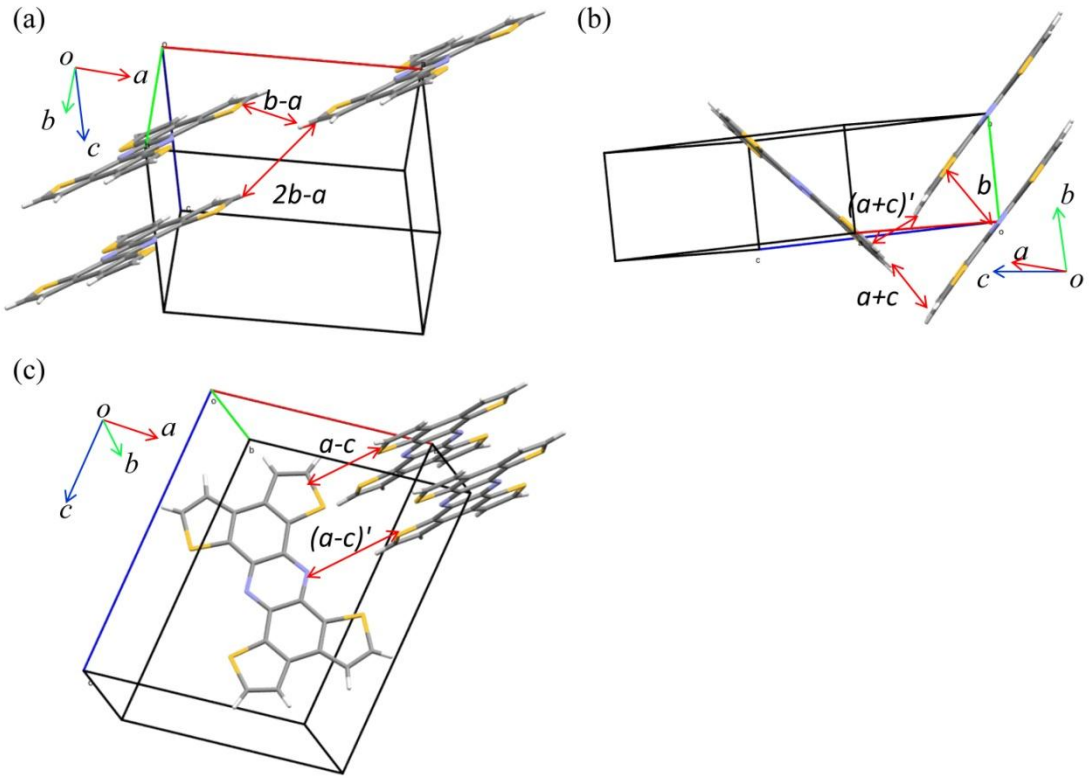

Fig. 2-30**.** Effective intermolecular contacts in ***t*-TTP** crystal along *c*-axis (a), *b*-axis (b) and a - c direction (c).

Table 2-9. Theoretical estimated intermolecular transfer intergrals (*Hab*), overlap intergrals (*Sab*), center-to-center distances (*d*), orbital interaction energy (*V*), reorganization energy (λ) and hopping mobilities for each molecular contact.

	Contact[a]	*Hab*[b] /meV	*Sab*[b]	*d* /Å	*V* /meV	λ [c] /m eV	$\mu_{hopping}$ / $cm^2\ V^{-1}\ S^{-1}$
***t*-TTP**	*2b-a*	0.2	-0.02	15.069	0	174	1.9×10^{-6}
***t*-TTP**	*b-a*	0.6	-0.2	12.314	-0.4	174	1.3×10^{-4}
***t*-TTP**	*b*	59.1	-7.4	5.014	20.2	174	4.7×10^{-2}
***t*-TTP**	*a+c*	-21.9	2.4	9.262	-9.3	174	3.4×10^{-2}
***t*-TTP**	*(a+c)'*	-24.1	2.4	9.262	-9.3	174	5.0×10^{-2}
***t*-TTP**	*a-c*	-8.3	0.9	11.862	-3.6	174	8.4×10^{-3}
***t*-TTP**	*(a-c)'*	5.0	-0.4	9.509	3.0	174	3.7×10^{-3}

[a] Corresponding molecular contacts are indicated in Fig. 2-30. [b] Calculated in PW91/TZ2P level. [c] Calculated in B3LYP/6-31G(d) level.

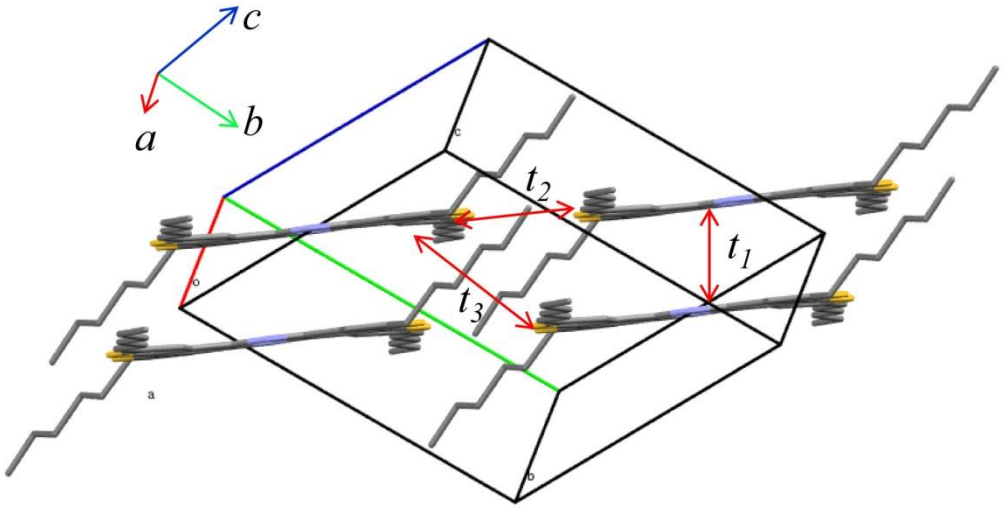

Fig. 2-31**.** Effective intermolecular contacts in ***l*-HTTP** crystal

Table 2-10. Theoretical estimated intermolecular transfer intergrals (*Hab*), overlap intergrals (*Sab*), center-to-center distances (*d*), orbital interaction energy (*V*), reorganization energy (λ) and hopping mobilities for each molecular contact.

	Contact[a]	*Hab*[b] /meV	*Sab*[b] /meV	*d* /Å	*V* /meV	λ [c] /m eV	$\mu_{hopping}$ / $cm^2\ V^{-1}\ S^{-1}$
***l*-HTTP**	t_1	-50.8	5.6	4.892	-25.0	155	8.7×10^{-2}
***l*-HTTP**	t_3	-0.4	0	14.988	0	155	6.3×10^{-5}
***l*-HTTP**	t_2	-3.9	0.4	12.749	-2.0	155	3.8×10^{-3}

[a] Corresponding molecular contacts are indicated in Fig. 2-31. [b] Calculated in PW91/TZ2P level. [c] Calculated in B3LYP/6-31G (d) level.

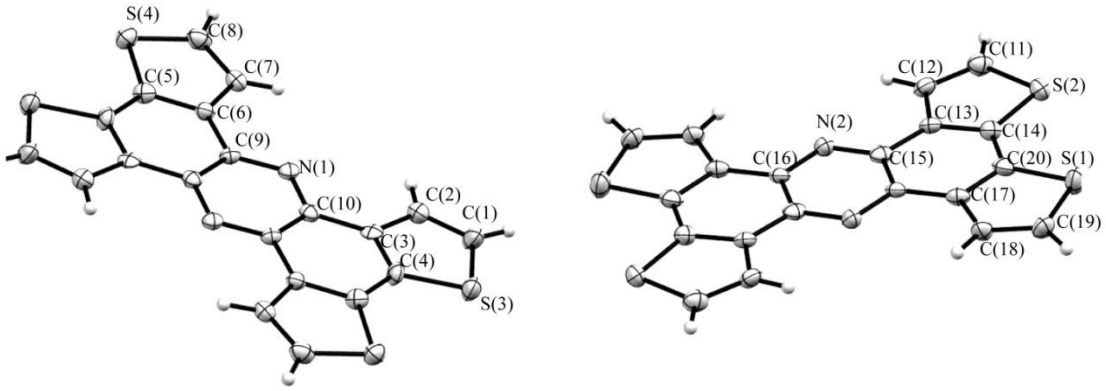

Fig. 2-32. ORTEP drawing of molecular structure of ***l*-TTP** with atomic numbering scheme

Table 2-11. Positional parameters and equivalent isotropic thermal parameters of ***l*-TTP**

atom	*x*	*y*	*z*	B_{eq} (Å^2)
S(1)	0.65346(15)	0.2078(8)	0.71068(9)	2.59(5)
S(2)	0.21057(14)	0.2043(6)	0.34970(9)	1.91(4)
S(3)	0.05697(15)	0.3591(7)	0.21204(9)	2.26(4)
S(4)	-0.13967(15)	0.7506(6)	0.15038(9)	1.96(4)
N(1)	-0.0779(4)	0.667(2)	-0.0242(2)	1.59(12)
N(2)	0.4456(4)	0.166(2)	0.5236(2)	1.70(13)
C(1)	0.1417(5)	0.185(3)	0.1984(3)	2.50(19)
C(2)	0.1329(5)	0.203(2)	0.1447(3)	1.97(16)
C(3)	0.0580(5)	0.357(2)	0.1117(3)	1.48(14)
C(4)	0.0098(5)	0.465(2)	0.1441(3)	1.77(15)
C(5)	-0.0680(5)	0.623(2)	0.1195(3)	1.69(15)
C(6)	-0.0970(5)	0.696(2)	0.0636(3)	1.52(14)
C(7)	-0.1758(5)	0.852(2)	0.0464(3)	1.63(14)
C(8)	-0.2060(5)	0.888(2)	0.0893(3)	2.20(17)
C(9)	-0.0473(5)	0.598(2)	0.0294(3)	1.36(14)
C(10)	-0.0291(5)	0.572(2)	-0.0539(3)	1.47(14)
C(11)	0.2042(6)	0.369(2)	0.4108(3)	2.25(17)
C(12)	0.2769(5)	0.338(2)	0.4528(3)	1.94(16)
C(13)	0.3397(5)	0.174(2)	0.4359(3)	1.53(14)
C(14)	0.3118(5)	0.086(2)	0.3807(3)	1.92(16)
C(15)	0.4221(5)	0.089(2)	0.4706(3)	1.69(15)
C(16)	0.5241(5)	0.086(2)	0.5541(3)	1.56(14)
C(17)	0.5526(5)	0.162(2)	0.6113(3)	1.59(15)
C(18)	0.5086(5)	0.330(2)	0.6434(3)	1.93(16)
C(19)	0.5541(6)	0.360(2)	0.6966(3)	2.33(18)
C(20)	0.6334(5)	0.084(2)	0.6432(3)	2.10(16)

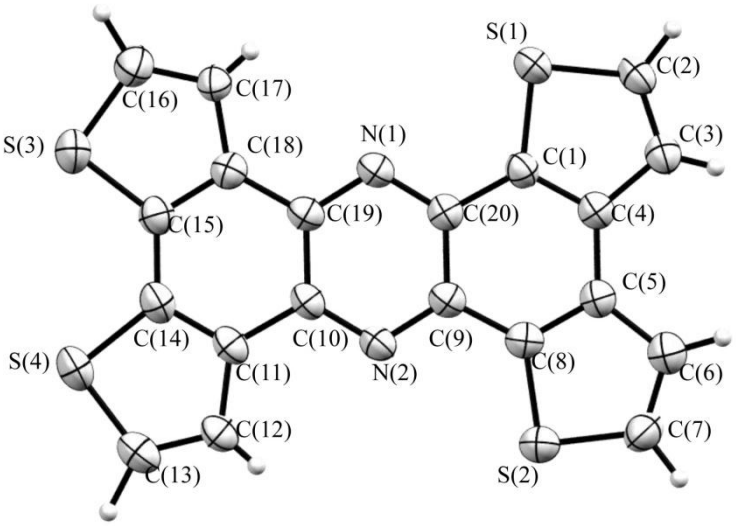

Fig. 2-33. ORTEP drawing of molecular structure of ***m*-TTP** with atomic numbering scheme

Table 2-12. Positional parameters and equivalent isotropic thermal parameters of ***m*-TTP**

atom	*x*	*y*	*z*	B_{eq} (Å^2)
S(1)	0.11817(6)	0.01158(18)	0.42182(6)	4.02(2)
S(2)	0.14158(7)	0.87587(18)	0.09091(6)	4.17(2)
S(3)	0.70820(7)	-0.1418(2)	0.34033(7)	5.04(2)
S(4)	0.71721(7)	0.3132(2)	0.13883(7)	4.96(3)
N(1)	0.3266(2)	0.1323(6)	0.32915(19)	3.56(6)
N(2)	0.3374(2)	0.5217(6)	0.17601(19)	3.66(6)
C(1)	-0.0155(3)	0.0980(8)	0.4096(2)	4.21(8)
C(2)	0.0074(3)	0.9179(8)	0.1004(3)	4.77(8)
C(3)	0.1406(2)	0.2408(7)	0.3302(2)	3.38(6)
C(4)	0.1516(3)	0.6262(7)	0.1810(2)	3.59(6)
C(5)	-0.0421(3)	0.2954(8)	0.3412(2)	4.11(7)
C(6)	-0.0300(3)	0.7516(8)	0.1682(3)	4.34(8)
C(7)	0.0487(2)	0.3798(7)	0.2934(2)	3.49(6)
C(8)	0.0539(2)	0.5801(7)	0.2162(2)	3.52(6)
C(9)	0.2420(2)	0.2820(7)	0.2935(2)	3.36(6)
C(10)	0.2466(2)	0.4787(7)	0.2162(2)	3.44(6)
C(11)	0.4179(3)	0.1743(7)	0.2887(2)	3.44(6)
C(12)	0.4223(2)	0.3707(8)	0.2111(2)	3.45(6)
C(13)	0.5115(2)	0.0181(7)	0.3250(2)	3.62(6)
C(14)	0.5225(2)	0.4054(7)	0.1696(2)	3.71(7)
C(15)	0.5239(3)	-0.1846(8)	0.4033(2)	3.80(7)
C(16)	0.5432(3)	0.5925(7)	0.0916(2)	3.95(7)
C(17)	0.6061(3)	0.0580(7)	0.2827(2)	3.86(7)
C(18)	0.6107(3)	0.2469(7)	0.2038(3)	3.99(7)
C(19)	0.6250(3)	-0.2808(9)	0.4184(3)	4.97(9)
C(20)	0.6450(3)	0.5612(9)	0.0689(3)	4.91(9)

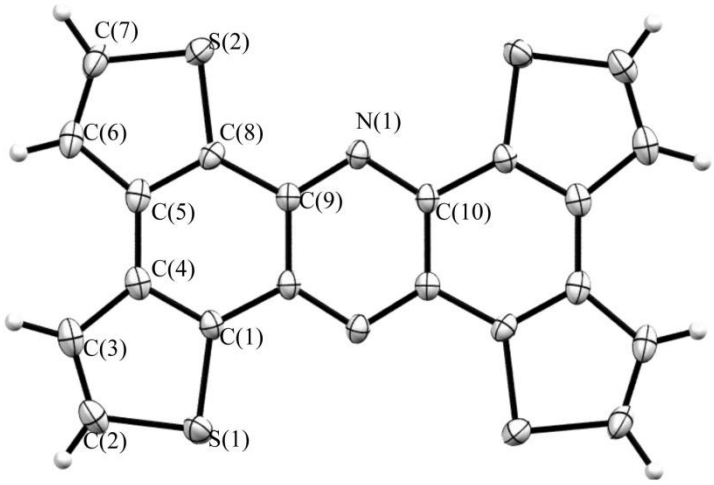

Fig. 2-34. ORTEP drawing of molecular structure of ***t*-TTP** with atomic numbering scheme

Table 2-13. Positional parameters and equivalent isotropic thermal parameters of ***t*-TTP**

atom	x	y	z	Beq
S(1)	0.80819(6)	0.91773(14)	0.48475(5)	2.060(15)
S(2)	0.36651(6)	0.83526(14)	0.73419(5)	2.142(15)
N(1)	0.39831(18)	0.4817(3)	0.55756(14)	1.46(3)
C(1)	0.6780(2)	0.8675(4)	0.54385(17)	1.49(3)
C(2)	0.8492(2)	1.1713(5)	0.56183(19)	2.14(4)
C(3)	0.7686(2)	1.2150(5)	0.62845(19)	2.04(4)
C(4)	0.6684(2)	1.0401(4)	0.61980(17)	1.57(4)
C(5)	0.5666(2)	1.0214(4)	0.67743(17)	1.61(4)
C(6)	0.5367(2)	1.1734(5)	0.75889(19)	2.02(4)
C(7)	0.4332(2)	1.0932(5)	0.7957(2)	2.31(4)
C(8)	0.4806(2)	0.8305(4)	0.65597(17)	1.53(3)
C(9)	0.4867(2)	0.6562(4)	0.57652(16)	1.36(3)
C(10)	0.4115(2)	0.3259(4)	0.48155(16)	1.40(3)

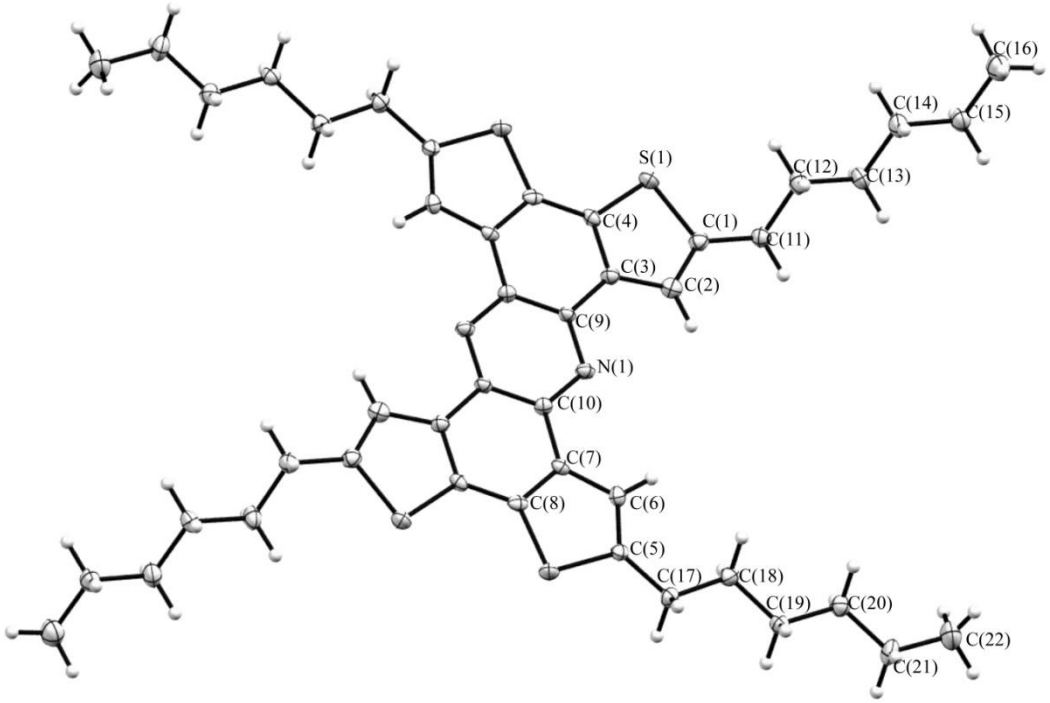

Fig. 2-35. ORTEP drawing of molecular structure of ***l*-HTTP** with atomic numbering scheme

Table 2-14. Positional parameters and equivalent isotropic thermal parameters of ***l*-HTTP**

atom	x	y	z	Beq
S(1)	1.3351(2)	0.75171(9)	0.71321(6)	1.63(2)
S(2)	1.2419(2)	0.15183(9)	0.44770(6)	1.59(2)
N(1)	1.3261(7)	0.4611(2)	0.56522(18)	1.28(7)
C(1)	1.1491(8)	0.6518(3)	0.7510(2)	1.51(9)
C(2)	1.1789(8)	0.5818(3)	0.7007(2)	1.48(8)
C(3)	1.3564(8)	0.6033(3)	0.6310(2)	1.34(8)
C(4)	1.4558(8)	0.6960(3)	0.6296(2)	1.20(8)
C(5)	1.0781(8)	0.1751(3)	0.5405(2)	1.26(8)
C(6)	1.1250(8)	0.2656(3)	0.5582(2)	1.36(8)
C(7)	1.2945(8)	0.3183(3)	0.4997(2)	1.17(8)
C(8)	1.3730(8)	0.2663(3)	0.4343(2)	1.27(8)
C(9)	1.4310(8)	0.5480(3)	0.5641(2)	1.09(8)
C(10)	1.3957(8)	0.4132(3)	0.5011(2)	1.14(8)
C(11)	0.9804(8)	0.6572(3)	0.8280(2)	1.60(9)
C(12)	1.1474(8)	0.6548(3)	0.8998(2)	1.85(9)
C(13)	0.9623(8)	0.6659(3)	0.9762(2)	1.77(9)
C(14)	1.1355(9)	0.6576(3)	1.0488(2)	2.12(10)
C(15)	0.9521(9)	0.6702(3)	1.1256(2)	2.09(10)
C(16)	1.1298(10)	0.6590(3)	1.1980(2)	2.75(11)
C(17)	0.9192(8)	0.0950(3)	0.5855(2)	1.54(9)
C(18)	0.7846(8)	0.1220(3)	0.6653(2)	1.64(9)
C(19)	0.6358(8)	0.0338(3)	0.7097(2)	1.53(9)
C(20)	0.4950(8)	0.0562(3)	0.7904(2)	1.84(9)
C(21)	0.3578(9)	-0.0333(3)	0.8346(2)	2.09(10)
C(22)	0.2072(10)	-0.0101(3)	0.9142(2)	3.38(13)

References

(1) (a) Deng, L. J.; Wang, X. Z.; Zhang, Z. C.; Li, J. Y. *J. Mater. Chem.* **2012**, *22*, 19700-19708; (b) Heckmann, A.; Lambert, C. *Angew. Chem. Int. Edit.* **2012**, *51*, 326-392; (c) Heimel, G.; Salzmann, I.; Duhm, S.; Koch, N. *Chem. Mater.* **2011**, *23*, 359-377; (d) Lo, S. C.; Burn, P. L. *Chem. Rev.* **2007**, *107*, 1097-1116; (e) Usluer, O.; Demic, S.; Egbe, D. A. M.; Birckner, E.; Tozlu, C.; Pivrikas, A.; Ramil, A. M.; Sariciftci, N. S. *Adv. Funct. Mater.* **2010**, *20*, 4152-4161; (f) Yan, B. P.; Cheung, C. C. C.; Kui, S. C. F.; Xiang, H. F.; Roy, V. A. L.; Xu, S. J.; Che, C. M. *Adv. Mater.* **2007**, *19*, 3599-3603; (g) Yu, Y. J.; Solomeshch, O.; Chechik, H.; Goryunkov, A. A.; Tuktarov, R. F.; Choi, D. H.; Jin, J. I.; Eichen, Y.; Tessler, N. *J. Appl. Phys.* **2008**, *104*; (h) Zhang, Q. S.; Li, J.; Shizu, K.; Huang, S. P.; Hirata, S.; Miyazaki, H.; Adachi, C. *J. Am. Chem. Soc.* **2012**, *134*, 14706-14709.

(2) (a) Holcombe, T. W.; Woo, C. H.; Kavulak, D. F. J.; Thompson, B. C.; Frechet, J. M. J. *J. Am. Chem. Soc.* **2009**, *131*, 14160-14161; (b) Li, C.; Liu, M. Y.; Pschirer, N. G.; Baumgarten, M.; Mullen, K. *Chem Rev* **2010**, *110*, 6817-6855; (c) Li, C.; Wonneberger, H. *Adv. Mater.* **2012**, *24*, 613-636; (d) Lim, E.; Lee, S.; Lee, K. K. *Mol. Cryst. Liq. Cryst.* **2012**, *565*, 98-105; (e) Wurthner, F.; Meerholz, K. *Chem-Eur J.* **2010**, *16*, 9366-9373; (f) Zhan, X. W.; Zhu, D. B. *Polym. Chem-Uk* **2010**, *1*, 409-419.

(3) (a) Huang, H.; Chen, Z. H.; Ortiz, R. P.; Newman, C.; Usta, H.; Lou, S.; Youn, J.; Noh, Y. Y.; Baeg, K. J.; Chen, L. X.; Facchetti, A.; Marks, T. J. *J. Am. Chem. Soc.* **2012**, *134*, 10966-10973; (b) Kanibolotsky, A. L.; Perepichka, I. F.; Skabara, P. J. *Chem. Soc. Rev.* **2010**, *39*, 2695-2728; (c) Saeki, A.; Koizumi, Y.; Aida, T.; Seki, S. *Acc. Chem. Res.* **2012**, *45*, 1193-1202; (d) Tang, M. L.; Bao, Z. A. *Chem. Mater.* **2011**, *23*, 446-455; (e) Tang, M. L.; Okamoto, T.; Bao, Z. N. *J. Am. Chem. Soc.* **2006**, *128*, 16002-16003; (f) Usta, H.; Facchetti, A.; Marks, T. J. *Acc. Chem. Res.* **2011**, *44*, 501-510; (g) Wu, W. P.; Liu, Y. Q.; Zhu, D. B. *Chem. Soc. Rev.* **2010**, *39*, 1489-1502; (h) Xiao, K.; Liu, Y. Q.; Qi, T.; Zhang,

W.; Wang, F.; Gao, J. H.; Qiu, W. F.; Ma, Y. Q.; Cui, G. L.; Chen, S. Y.; Zhan, X. W.; Yu, G.; Qin, J. G.; Hu, W. P.; Zhu, D. B. *J. Am. Chem. Soc.* **2005**, *127*, 13281-13286.

(4) (a) Kang, M. J.; Doi, I.; Mori, H.; Miyazaki, E.; Takimiya, K.; Ikeda, M.; Kuwabara, H. *Adv. Mater.* **2011**, *23*, 1222-1225; (b) Nakayama, K.; Hirose, Y.; Soeda, J.; Yoshizumi, M.; Uemura, T.; Uno, M.; Li, W. Y.; Kang, M. J.; Yamagishi, M.; Okada, Y.; Miyazaki, E.; Nakazawa, Y.; Nakao, A.; Takimiya, K.; Takeya, J. *Adv. Mater.* **2011**, *23*, 1626-1629; (c) Niimi, K.; Shinamura, S.; Osaka, I.; Miyazaki, E.; Takimiya, K. *J. Am. Chem. Soc.* **2011**, *133*, 8732-8739; (d) Uno, M.; Tominari, Y.; Yamagishi, M.; Doi, I.; Miyazaki, E.; Takimiya, K.; Takeya, J. *Appl. Phys. Lett.* **2009**, *94*; (e) Yamamoto, T.; Takimiya, K. *J. Am. Chem. Soc.* **2007**, *129*, 2224-2225.

(5) Takimiya, K.; Kunugi, Y.; Toyoshima, Y.; Otsubo, T. *J. Am. Chem. Soc.* **2005**, *127*, 3605-3612.

(6) Ebata, H.; Izawa, T.; Miyazaki, E.; Takimiya, K.; Ikeda, M.; Kuwabara, H.; Yui, T. *J. Am. Chem. Soc.* **2007**, *129*, 15732-15733.

(7) Xie, Y. F.; Fujimoto, T.; Dalgleish, S.; Shuku, Y.; Matsushita, M. M.; Awaga, K. *J. Mater. Chem. C.* **2013**, *1*, 3467-3481.

(8) (a) Hussain, H.; Specht, S.; Sarite, S. R.; Saeftel, M.; Hoerauf, A.; Schulz, B.; Krohn, K. *J. Med. Chem.* **2011**, *54*, 4913-4917; (b) Putala, M.; Kastner-Pustet, N.; Mannschreck, A. *Tetrahedron: Asymmetry* **2001**, *12*, 3333-3342.

(9) Brusso, J. L.; Hirst, O. D.; Dadvand, A.; Ganesan, S.; Cicoira, F.; Robertson, C. M.; Oakley, R. T.; Rosei, F.; Perepichka, D. F. *Chem. Mater.* **2008**, *20*, 2484-2494.

(10) Liu, W. J.; Zhou, Y.; Ma, Y. G.; Cao, Y.; Wang, J.; Pei, J. *Org. Lett.* **2007**, *9*, 4187-4190.

(11) Carlier, L.; Baron, M.; Chamayou, A.; Couarraze, G. *Tetrahedron Lett.* **2011**, *52*, 4686-4689.

(12) Meyer, A.; Sigmund, E.; Luppertz, F.; Schnakenburg, G.; Gadaczek, I.; Bredow, T.; Jester, S. S.; Hoger, S. *Beilstein J. Org. Chem.* **2010**, *6*, 1180-1187.

(13) Arroyave, F. A.; Richard, C. A.; Reynolds, J. R. *Org. Lett.* **2012**, *14*, 6138-6141.

(14) D'Andrade, B. W.; Datta, S.; Forrest, S. R.; Djurovich, P.; Polikarpov, E.; Thompson, M. E. *Org. Electron.* **2005**, *6*, 11-20.

(15) Frisch, M. J.; Trucks, G. W.; Schlegel, H. B.; Scuseria, G. E.; Robb, M. A.; Cheeseman, J. R.; Montgomery, J. A. J.; Vreven, T.; Kudin, K. N.; Burant, J. C.; Millam, J. M.; Iyengar, S. S.; Tomasi, J.; Barone, V.; Mennucci, B.; Cossi, M.; Scalmani, G.; Rega, N.; Petersson, G. A.; Nakatsuji, H.; Hada, M.; Ehara, M.; Toyota, K.; Fukuda, R.; Hasegawa, J.; Ishida, M.; Nakajima, T.; Honda, Y.; Kitao, O.; Nakai, H.; Klene, M.; Li, X.; Knox, J. E.; Hratchian, H. P.; Cross, J. B.; Bakken, V.; Adamo, C.; Jaramillo, J.; Gomperts, R.; Stratmann, R. E.; Yazyev, O.; Austin, A. J.; Cammi, R.; Pomelli, C.; Ochterski, J. W.; Ayala, P. Y.; Morokuma, K.; Voth, G. A.; Salvador, P.; Dannenberg, J. J.; Zakrzewski, V. G.; Dapprich, S.; Daniels, A. D.; Strain, M. C.; Farkas, O.; Malick, D. K.; Rabuck, A. D.; Raghavachari, K.; Foresman, J. B.; Ortiz, J. V.; Cui, Q.; Baboul, A. G.; Clifford, S.; Cioslowski, J.; Stefanov, B. B.; Liu, G.; Liashenko, A.; Piskorz, P.; Komaromi, I.; Martin, R. L.; Fox, D. J.; Keith, T.; Al-Laham, M. A.; Peng, C. Y.; Nanayakkara, A.; Challacombe, M.; Gill, P. M. W.; Johnson, B.; Chen, W.; Wong, M. W.; Gonzalez, C.; Pople, J. A. *Gaussian 03, revision C.02* **2004**, Gaussian, Inc.: Wallingford, CT.

(16) (a) Newton, M. D. *Chem. Rev.* **1991**, *91*, 767-792; (b) Senthilkumar, K.; Grozema, F. C.; Bickelhaupt, F. M.; Siebbeles, L. D. A. *J. Chem. Phys.* **2003**, *119*, 9809-9817; (c) Senthilkumar, K.; Grozema, F. C.; Guerra, C. F.; Bickelhaupt, F. M.; Lewis, F. D.; Berlin, Y. A.; Ratner, M. A.; Siebbeles, L. D. A. *J. Am. Chem. Soc.* **2005**, *127*, 14894-14903.

(17) Getmanenko, Y. A.; Tongwa, P.; Timofeeva, T. V.; Marder, S. R. *Org. Lett.* **2010**, *12*, 2136-2139.

(18) (a) CrystalClear, R. C., 1999;; CrystalClear Software User's Guide, M. s. C., 2000;; Pflugrath, J. W. *Acta Crystallogr., Sect. D,* **1999**, *55*, 1718-1725; (b) Structure, C. C.; Analysis Package, R. a. R. A., 9009 New; Trails Dr., T. W., TX, USA, **2000-2007**.

(19) Sheldrick, G. M. *SHELX97* **1997**.

(20) (a) Becke, A. D. *Phys. Rev. A: At., Mol., Opt. Phys.*, **1988**, *38*, 3098-3100; (b) Becke, A. D. *J. Chem. Phys.* **1993**, *98*, 5648-5652; (c) Lee, C.; Yang, W.; Parr, R. G. *Phys. Rev. B: Condens. Matter Mater. Phys.*, **1988**, *37*, 785-789; (d) Stephens, P. J.; Devlin, F. J.; Chabalowski, C. F.; Frisch, M. J. *J. Phys. Chem.* **1994**, *98*, 11623-11627.

Chapter 3 Synthesis, structures and electronic properties of novel acceptors: thiadiazole-fused aromatics

3.1 Introduction

Nowadays, various types of organic electron donor molecules have been investigated for the organic electronics, optics, and magnetism. On the other hand, in comparison with the donor molecules, only a few types of organic electron acceptor molecules have been developed for organic electronics. However, electron acceptors can act as n-type semiconductors which are indispensable for constructing principal electronic devices such as p-n junction diodes, bipolar transitors, OLEDs, and solar cells. Therefore, development of novel organic acceptor materials with high electron mobility and stability is still very important and interesting topic.

For designing organic electron acceptor materials, one effective approach is to convert known donor materials into acceptors by introducing electron-withdrawing group for lowering the LUMO energy. Various types of organic acceptors which applied for n-type semiconductor materials have been realized via functionalization of acene, arylene, thiophene, phenylene, and fluorene-based π-skeleton with electron-difficient subsituents such as perfluoroakyl, －CN, －F, perfluoroaryl, carbonyl (－C=O), and imide (－C(O)NHC(O)－) groups.

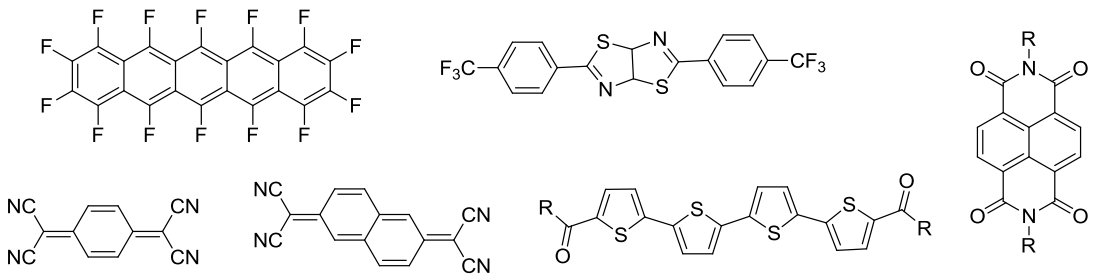

Scheme 3-1. N-type materials with electron-difficient substituents.

Thiadiazole, which is a five-memberd ring having N-S-N moiety, is also known as an electron-withdrawing unit contained in various acceptor molecules reported so far.[1] In those molecules, thiadiazole is fused with π-conjugated rings, such as benzo,[2] quino,[3] thieno,[4] etc, to extend π-conjugating skeleton. Extention of π-conjugation system can contribute to increase intermolecular π-stacking interaction as well as for increasing the acceptor ability. Furthermore, thiadiazole rings often show short intermolecular contacts each other perpendicular to the π-staking direction due to the polarized S-N bonds. These features are favorable for increasing carrier mobility in molecular crystals. On the other hand, thiadiazoledioxide, which is an oxidized form of thiadiazole, has much stronger acceptor ability than that of the thiadiazole itself. The introduction of dioxide moiety can also contribute to improve the solubility in organic solvents as well as ehancing the acceptor ability.

Thiadiazole could also be fused on poly-aromatic systems such as phenanthrene, pyrene and phenanthroline to form various acceptors as shown in Scheme 3-2 (**1**, **2**, **3** and **4**).[5] Moreover, their acceptor abilities can be tuned by the oxidation state on the thiadiazole ring which is important for the material application. Reduction potential of dioxide compound (**2c**: -0.66 V vs Fc/Fc^+) is much higher than that of monoxide compound (**2b**: -0.88 V vs Fc/Fc^+) and bare thiadiazole compound (**2a**: -2.08 V vs Fc/Fc^+).[5a] Recently, [1,2,5]thiadiazolo[3,4-f][1,10] phenanthroline 2,2-dioxide (**tdapO$_2$**) (**4b**) was prepared which showed good acceptor ability for affording stable anion radical crystal.[5b] Furthermore, **tdapO$_2$** showed enough thermal stability for the preparation of thin film through vapor deposition process. This result prompted us to develop n-type organic semiconductor materials derivatized with thiadiazoledioxide.

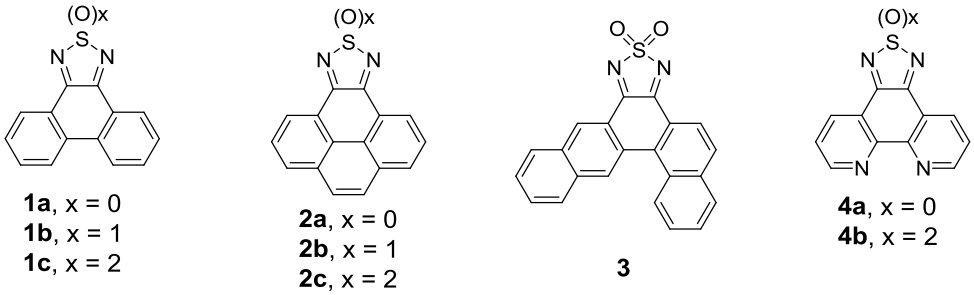

Scheme 3-2. Molecular structures of thiadiazole-fused materials.

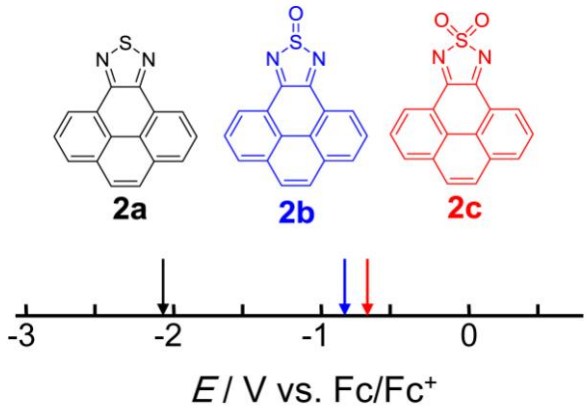

Fig. 3-1. First reduction potentials of **2a-c** in CH_3CN containing 0.1 *n*-Bu_4PF_6 as electrolyte.[5a]

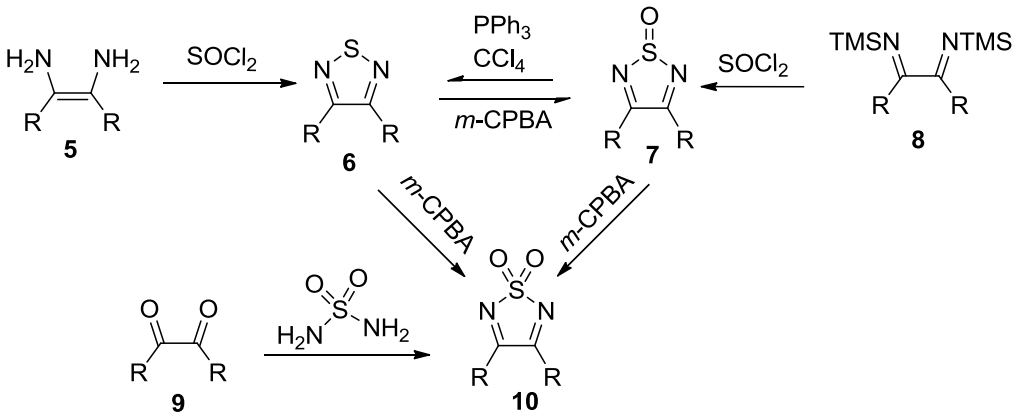

Scheme 3-3. Syntheses of thiadiazole derivatives.

There are several methods to synthesize these thiadiazole derivatives as shown in Scheme 3-3. Thiadiazole derivatives **6** can be prepared from diamine **5**,[6] and it can be oxidized into thiadiazole-monoxide derivatives **7**[7] or thiadiazole-dioxide derivatives **10**[7a] by meta-chloroperoxybenzoic acid (*m*-CPBA). Thiadiazole derivatives **7** can be synthesized from **8**, and it can be reduced into thiadiazole derivatives **10** and oxidized into thiadiazole-dioxide derivatives **10**.[5a] Thiadiazole-dioxide derivatives **10** can be also obtained by the condensation between diketone **9** and sulfuric diamide.[5d] These simple synthetic methods and inter-conversion of the thiadiazole derivatives provide us the possibilities to develop a series of thiadiazole-fused materials.

In this chapter, a series of aromatic materials fused with thiadiazole moiety with different oxidation states were developed. The thiadiazole was fused on phenanthrene to form phenanthro[9,10-c][1,2,5]thiadiazole derivatives (Scheme 3-4). In order to

improve the π-conjugation of the molecules, thiadiazole moiety was also fused on the picene skeleton. Picene consists of five annulated-benzene rings in a W-arrangement, attracting much attention in terms of high carrier mobility in neutral crystal and superconductivity upon alkali metal doping.[8] The p-channel charge transport characteristics are observed in picene-based FET device with the highest field-effect mobilities up to 1 ~ 3 cm^2 V^{-1} s^{-1}.[9] Due to the π-extended structure and the high transistor performace of picene, reasonable electron charge transport characteristic was obtained in the prepared material, **$PTDAO_2$**. The anion radical salts of **$PTDAO_2$** could be also obtained upon electrochemical reduction. Through these approaches, the potential application of the thiadiazole-fused aromatics for organic electronics was investigated.

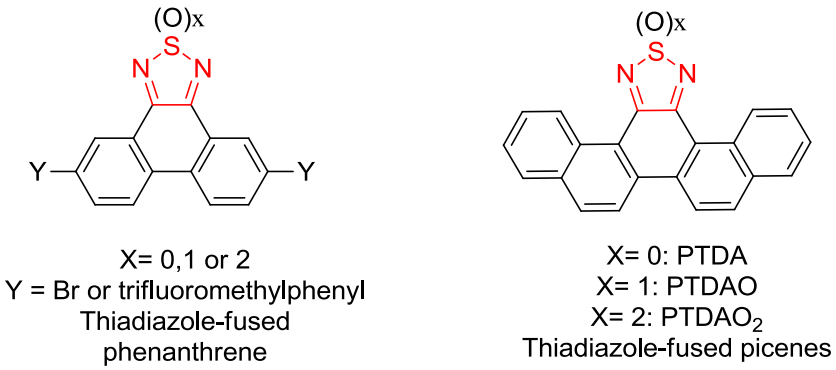

Scheme 3-4. Molecular structure of thiadiazole-fused aromatics.

3.2 Results and discussion

3.2.1 Syntheses

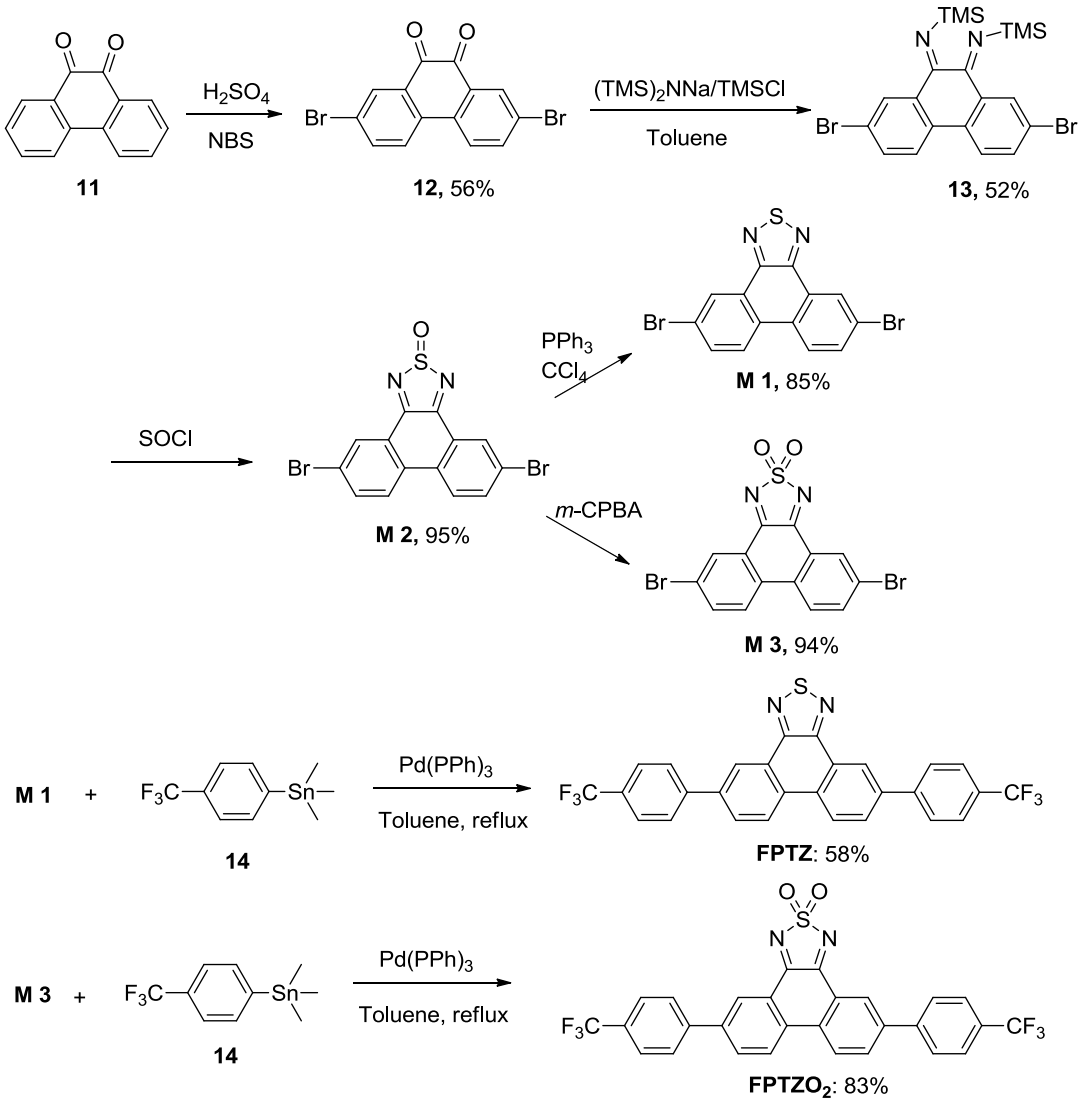

Scheme 3-5. Syntheses of thiadiazole-fused phenanthrenes

As shown in Scheme 3-5, the thiadiazole-fused phenanthrene derivatives were synthesized from the diketone **11**. After bromization of diketone **11**, the obtained compound **12** was reacted with sodium bis(trimethylsilyl)amide ($(TMS)_2NNa$) and chlorotrimethylsilane (TMSCl) in toluene to get compound **13**. **M2** was obtained by refluxing with sulfurous dichloride and **13**. **M2** was further reduced with PPh_3 in CCl_4 to give bromized thiadiazole phenanthrene (**M1**) or, alternatively, oxidized with

peroxy acid to give bromized thiadiazole dioxide phenanthrene (**M3**). The advantage of this method is to provide easy synthetic route to each oxidation state of thiadiazole aromatics. The oxidation states of the thiadiazole aromatics could tune the acceptor abilities of them. **M1** and **M3** were coupled with compound **14** to give **FPTZ** and **$FPTZO_2$**, respectively. The structures of these materials were confirmed by NMR, MS, and IR etc. **FPTZ** is a white powder and its solubility in common organic solvents such as dichloromethane, chloroform, and toluene is much higher than that of **$FPTZO_2$**. Crystal of **$FPTZO_2$** was obtained from the chloroform solution.

In order to improve the π-π stacking structure in the cyrstal, thiadiazole moiety was also fused on picene skeleton which has planar structure. As illustrated in Scheme 3-6, **$PTDAO_2$** was synthesized via four steps from a comercially available starting material, 1-naphthaldehyde (**15**), with reasonable yields: 1-naphtoaldehyde (**15)** was converted to corresponding pinacol **20**[10] via reductive coupling reaction with sec-BuMgCl and Cp_2TiCl_2, and then the pinacol **20** was oxidized with NBS to afford diketone **17**.[11] Compound **17** was reacted with sulfamide to form 3,4-bis-(1-naphthalenyl)-1,2,5-thiadiazole 1,1-dioxide (**18**) as a yellow solid, followed by the the oxidative cyclization reaction with anhydrous $AlCl_3$ to afford **$PTDAO_2$** as a brown solid. Compound **18** exihbits good solubility in dichloromethane(> 10 mg/mL), while the solubility of the recation product, **$PTDAO_2$** was very low (< 0.1 mg/mL). Compound **18** was purified by recrystallization from saturated dichloromethane solution, and the molecular structure was comfirmed by NMR and single crystal X-ray

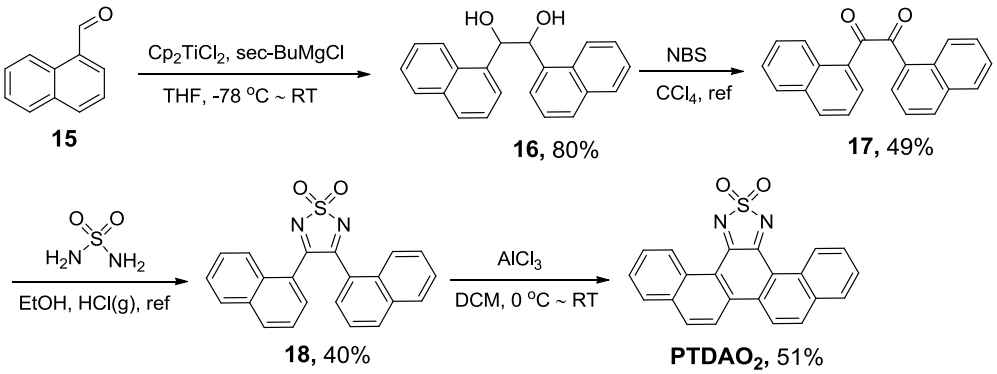

Scheme 3-6. Synthesis of thiadiazole-fused picenes

diffraction. Crystals of **$PTDAO_2$** were obtained by recrystallization from dichloromethane solution or sublimation, and the structure was comfirmed by single crystal X-ray diffraction.

3.2.2 Molecular orbital calculation

Fig. 3-2 shows the calculated spatial distributions and energy levels of frontier molecular orbitals of picene and thiadizole-dioxide fused aromatics. The thiadiazole-fused aromatics (-2.34 eV, -3.67 eV and -3.54 eV for **FPTZ**, **$FPTZO_2$** and **$PTDAO_2$**, respectively) exhibit low LUMO energeries because of the thiadiazole moiety. Especially, **$FPTZO_2$** and **$PTDAO_2$** have much lower LUMO energies which probably can be easily reduced to afford anion radicals. Molecular orbital distribution of **FPTZ**, **$FPTZO_2$** don't delocalize the whole molecules which could be a disadvantage for the intermolecular charge transport. However, **$PTDAO_2$** with delocalized molecular orbital distribution for the whole molecule can enhance the intermolecular overlap which would be an advantage for the intermolecular charge transport. On the other hand, the energy of LUMO in **$PTDAO_2$** (-3.54 eV) is much lower than that of picene (-1.27 eV) as the result of the introduction of thiadiazole dioxide moiety. This low energy level is close to the work functions of nomally used electrode materials such as Au, Pt, and Al, and suitable for the electron injection from those electrodes. For these reasons, **$PTDAO_2$** also could be n-type organic semiconductor besides the stabilization of forming the anion raidcal species.

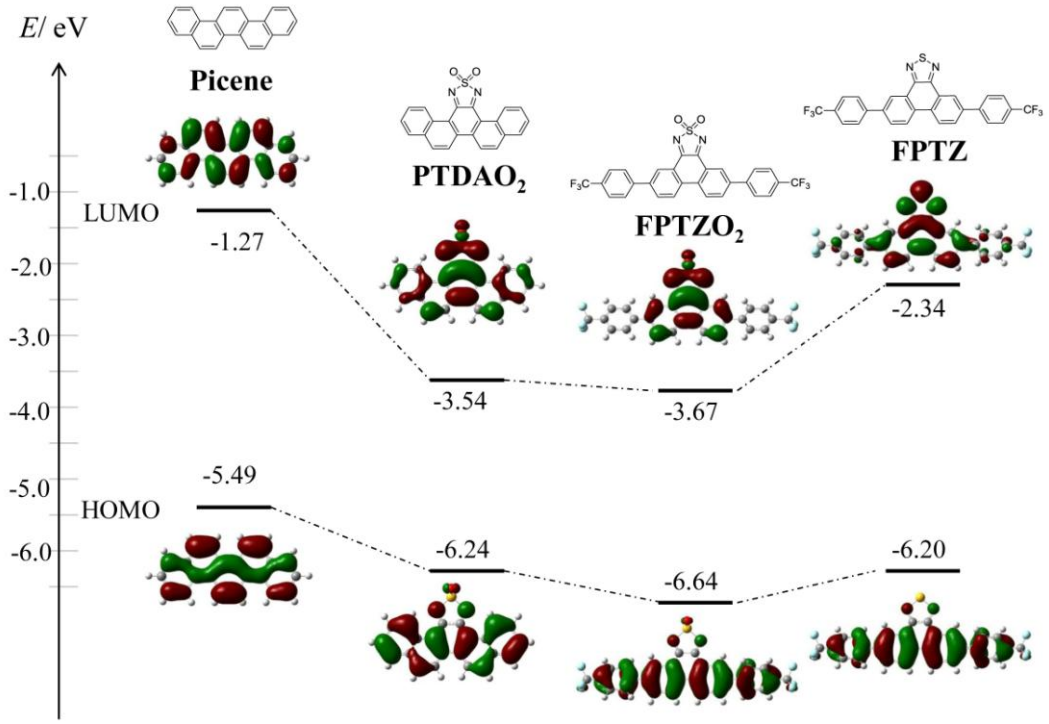

Fig. 3-2. Calculated frontier orbitals of Picene and thiadiazole-fused aromatics at DFT B3LYP/6-31g(d) level.

3.2.3 Electrochemical and optical properties

Electrochemical properties of thiadiazole-fused aromatics were investigated by cyclic voltammetry (CV) (Fig. 3-3). Thiadiazole-dioxided aromatics (**FPTZO$_2$**, **PTDAO$_2$** and compound **22**) showed reduction peaks at lower potential than that of thiadiazole molecule (**FPTZ**) (Table 3-1) which is consistent with the DFT calculation (Fig. 3-2). The voltammogram of compound **18** showed one reversible peak at $E_{1/2}$ = -0.93 V (vs Fc/Fc$^+$) and another irreversible peak with E_{pa} = -1.80 V (vs Fc/Fc$^+$) within the electrochemical window. **PTDAO$_2$** showed two reversible redox peaks at $E_{1/2}$ = -0.69 and -1.30 V vs Fc/Fc$^+$, similar to other reported thiadiazole dioxide derivatized molecules.[5a,5b,5e] In reference to the first reduction potential, the acceptor ability of **PTDAO$_2$** was improved in comparison with that of compound **18**. LUMO energy of **PTDAO$_2$** estimated from the half wave potential was - 4.1 eV, which is close to the theoretical value (- 3.54 eV) whereas much lower than that of picene (- 2.04 eV).[12] This also evidences that the acceptor ability of **PTDAO$_2$** was largely improved after

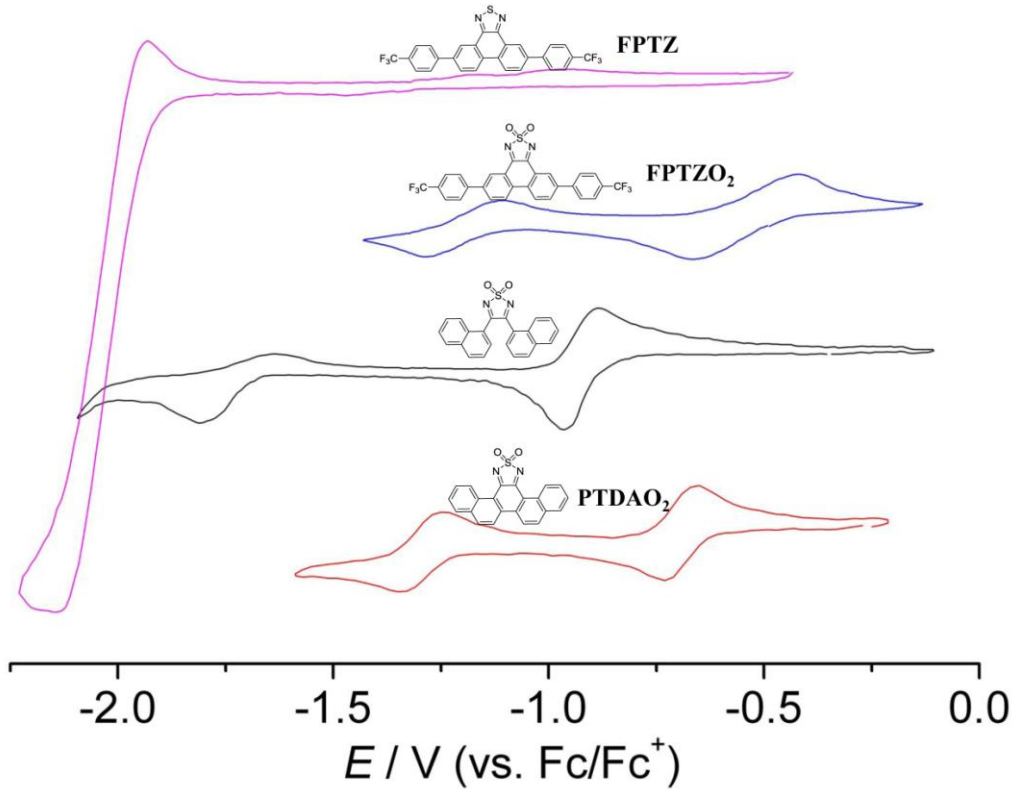

Fig. 3-3. Cyclic valtammograms (scan rate 100 mV S^{-1}) of thiadiazole-fused aromatics record in DCM solution containing Bu_4NClO_4 (0.1 M) as electrolyte. Pt electrode was used for working electrode and counter electrode. Potentials referenced to Fc/Fc^+.

fusing thiadiazole dioxide on picene. The UV-vis absorption spectra of thiadiazole-fused aromatics recorded in dichloromethane or chloroform solution and thin film state are shown in Fig. 3-4. Thiadiazole-dioxide moiety (**$FPTZO_2$**, **$PTDAO_2$** and compound **18**) usually causes a longer absorption band in comparison with the thiadiazole moiety (**FPTZ**) as shown in Fig. 3-4. **$FPTZO_2$** showed a strong absorption band around 300nm and another weak absorption band around 500 nm. Thin film absorption can't be obtained due to the decomposition of **$FPTZO_2$** at the sublimation temperature. Compound **18** has absportions around 411 nm and 263 nm, and showed red shift of 14 nm in the thin-film state. **$PTDAO_2$** showed absorption peaks at 256 nm, 306 nm and 448 nm in dichloromethane. In thin-film, the longest absorption peak showed red shift by 30 nm from that in solution, while there was no significant change in the vibronic structure. The larger red shift of **$PTDAO_2$** thin film in comparison with that of compound **18** probably indicates the π-π stacking structure in the thin-film state due to the planar picene skeleton of **$PTDAO_2$**.

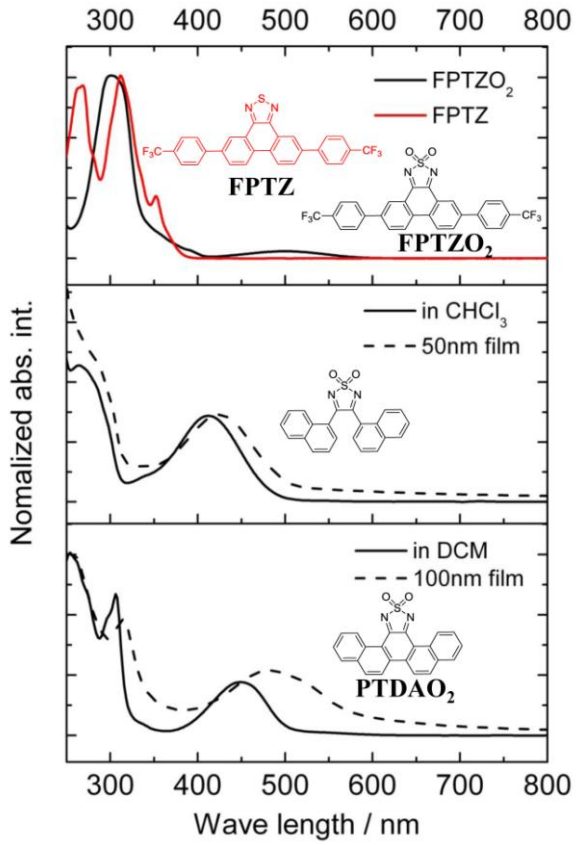

Fig. 3-4. UV-vis absorption spectra of thiadiazole-fused aromatics in the solution and in thin film state.

Table 3-1**.** Electrochemical, and Optical Properties of thiadiazole-fused aromatics and Picene.

	FPTZ	**FPTZO2**	**18**	**PTDAO2**	**Picene**[f]
$(E_{1/2})_1$ ^{exp} **(V)** [a]	-2.05	-0.54	-0.93	-0.69	-2.76
$(E_{1/2})_2$ ^{exp} **(V)** [a]	---	-1.20	-1.80	-1.30	-3.16
E_{LUMO} ^{exp} **(eV)** [b]	-2.75	-4.26	-3.87	-4.11	-2.04
E_{LUMO} ^{calcd} **(eV)** [c]	-2.34	-3.67	---	-3.54	-1.27
E_{HOMO} ^{calcd} **(eV)** [c]	-6.20	-6.64	---	-6.24	-5.49
λ_{max} ^{abs} **(nm)** [d]	312	500	411	448	---
λ_{max} ^{abs} **(nm)** [e]	---	---	425	481	---

[a] Measured in DCM, TBAP (0.1M) as supporting electrolyte, and referenced to Fc/Fc^+. [b] Estimated from the CV measurement according to the empirical formula $E_{HOMO} = -4.8 - (E_{1/2})_1$ ^{exp} eV from reference 12a. [c] B3LYP/6-31G(d). [d] Measured in $CHCl_3$. [e] In thin-film state. [f] See reference 12b, c.

3.2.4 X-ray crystal structures

Crystals of thiadiazole-dioxide fused aromatics were obtained by recrystallization and sublimation. Cell parameters are summarized in Table 3-2. Crystal of **FPTZO$_2$** obtained by recrystallization from chloroform solution contains three **FPTZO$_2$** molecules and two solvent molecules in one crystal cell, and the trifluorophenyl group and thiadiazole phenanthrene plane are twisted slightly (Fig. 3-5). Crystal of compound **18** was obtained from the dichloromethane solution. Naphthalene rings in the molecules showed close π-π distance (3.329 Å) (Fig. 3-6). Crystals of **PTDAO$_2$** were obtained by recrystallization and sublimation. Crystals obtained form these two methods are different in space group and molecular packing. Crystal obtained by sublimation with a space group *Pbca* was assigned as α-phase. Molecules in the α phase crystal have slightly twisted structure (Fig. 3-7(b)) and packed not in parallel π-staking manner with each other: the dihedral angle between adjacent molecule is 6.03 degree (Fig. 3-7(c)). Crystal obtained by slow evaporation of dichloromethane solution with a space group $P\bar{1}$ was assigned as the β-phase. Molecules in β-phase are planar, and they are packing along *a* axis with a π-π distance of 3.412 Å and a large area of intermolecular overlap (Fig. 3-8). Those features in the β-phase crystal is advantagous to the intermolecular charge transport. Since thiadiazole dioxide moiety has strong dipole moment, molecules pack alternately to compensate the dipole moment in π-π stacking column along *a* axis in the β-phase. The distance of the SO_2 moieties between the cloumns is relatively far from each other because of the electrostatic repulsion of negatively charged oxygens.

Table 3-2**.** Crytal cell parameters of thiadiazole-fused aromatics.

	$FPTZO_2$	**18**	**$PTDAO_2$ (α)**	**$PTDAO_2$ (β)**
Crystal system	*Triclinic*	*Monoclinic*	*Orthorhombic*	*Triclinic*
Space group	*P*1	*C*2/c	*P*bca	$P\bar{1}$
a (Å)	9.829(2)	19.248(4)	15.334(6)	7.175(4)
b (Å)	14.817(3)	11.102(2)	8.423(3)	10.612(5)
c (Å)	15.273(3)	8.5467(2)	23.954(1)	10.682(5)
α (deg)	68.991(10)	---	---	97.969(9)
β (deg)	73.975(11)	106.658(3)	---	92.937(8)
γ (deg)	74.696(11)	---	---	97.683(9)
R, R_w ($I > 2\sigma$)	0.1416,0.2493	0.0396, 0.0977	0.0848, 0.0530	0.0783, 0.1603
δ(Å)[a]	---	3.329	---	3.412

[a] π-π distance in the packing structure.

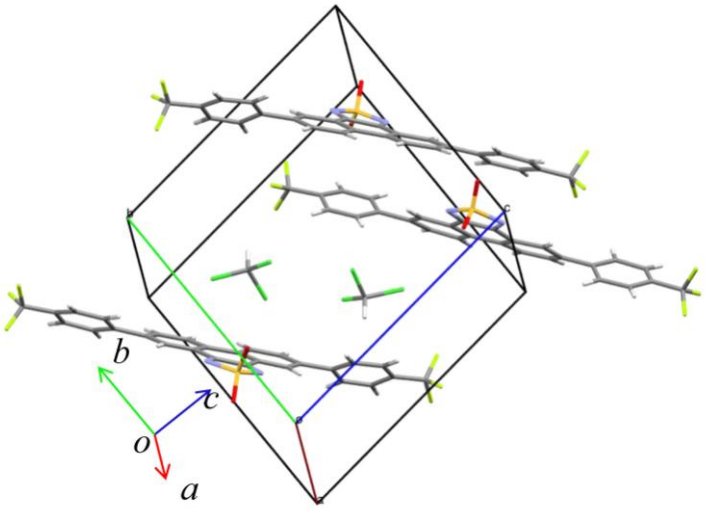

Fig. 3-5. Crystal structure of **$FPTZO_2$**.

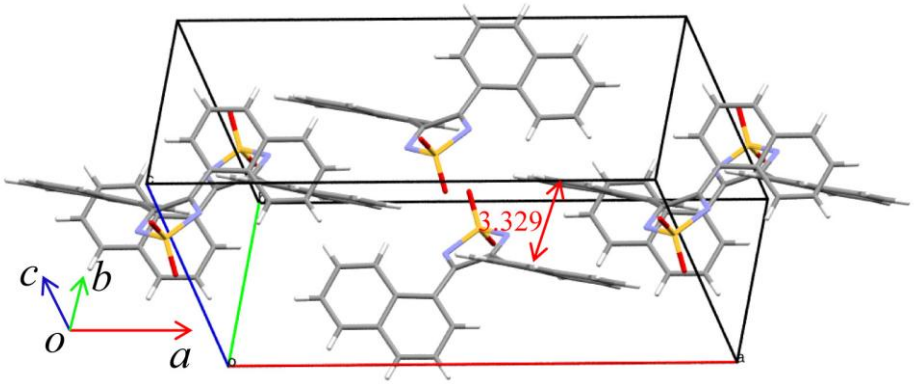

Fig. 3-6. Crystal structure of compound **18**.

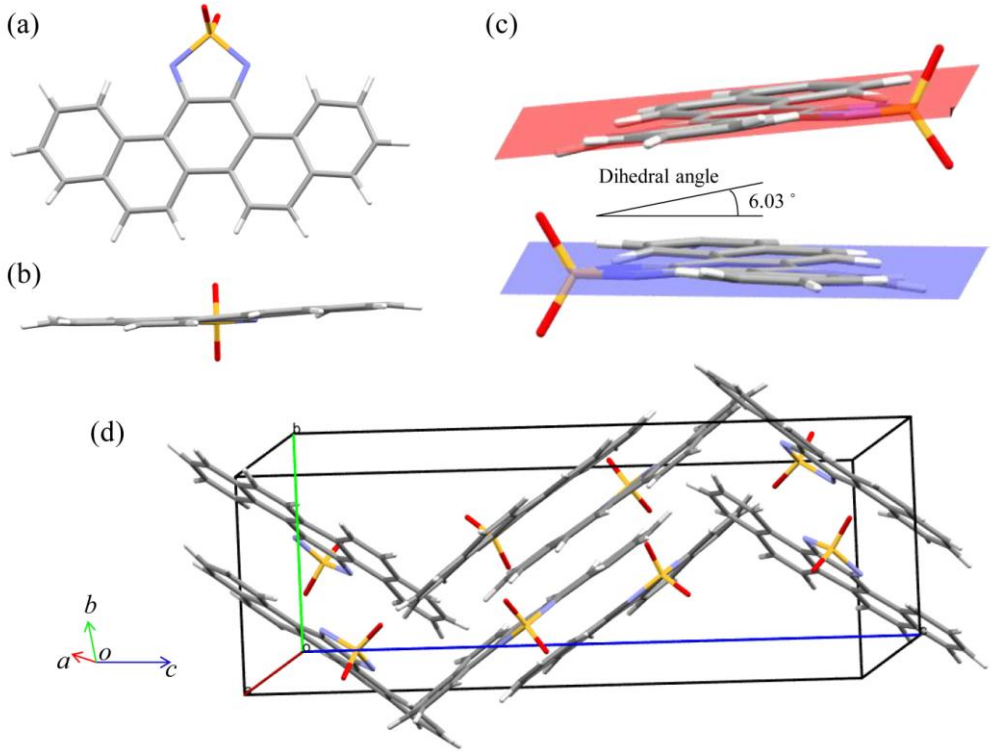

Fig. 3-7. Crystal structure of **PTDAO$_2$ (α)**. Top view (a) and side view (b). Intermolecular overlaps (c). Crystal structure (d).

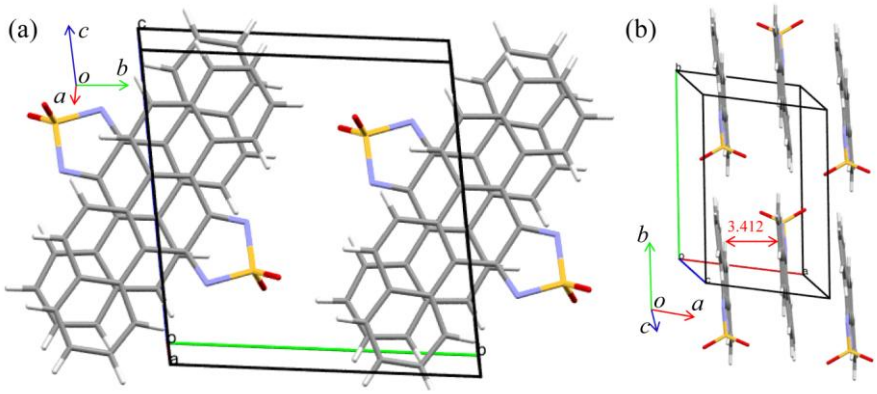

Fig. 3-8. Crystal structure of **PTDAO$_2$(β)**. (a) Intermolecular overlap. View along *a* axis. (b) π···π distance between the molecules (unit: Å). View along *c* axis.

3.2.5 Preparation, characterization, and FET performance of thin films

Thin film of **$FPTZO_2$** could not be prepared via vapor deposition due to its unstability at high temprepture. Thin film of compound **18** and **$PTDAO_2$** were prepared by vapor deposition on Si substrates (with SiO_2 on the surface) for investigating the information on the molecular arrangements. Thin-film X-ray diffraction of compound **18** doesn't show any peaks that indicates the amorphous molecular structure in the thin film (Fig. 3-9), while thin-film X-ray diffraction of **$PTDAO_2$** shows sharply resolved peaks assignable to multiple reflections, indicating crystalline order in the direction of substrate nomal (Fig. 3-10). Interestingly, the crystal phase of the thin film is the same with the β-phase single crystal of **$PTDAO_2$**, comparing with the simulated powder pattern from the β-phase crystal structure. The interlayer spacing (*d*) determined from the first layer line of the thin-film XRD is 10.4 Å which is close to the length of both *b* and *c* axes in the β phase crystal, so it is difficult to assign the molecular orientation on the substrate: The first sharp peak of the thin-film XRD is assignable for both reflection planes (001) and (010) as shown Fig. 3-10(a). The possible two kinds of molecular orientation on the substate are illustated in Fig. 3-10(b). However, the π-π stacking direction of either (00*l*) reflection planes or (0*l*0) is parellel to the substrate(Fig. 3-10(b)). This is one of the important feature for resonable charge transport performance in the thin-film state.

Thin film OFETs of **$PTDAO_2$** were prepared by vacuum deposition on a microstructured Pt electrodes with different channel lengths, 2 μm, 5 μm, 10 μm, 20 μm and 50 μm fabricated on Si/SiO_2 substrates with a bottom-contact, bottom-gate configration. All of the devices with different channel lengths showed electron mobilties around 10^{-4} $cm^2 V^{-1} s^{-1}$, threshold voltage 27 ~ 39 V, and high current on/off ratios, as shown in Table 3-3 and Fig. 3-11. In order to improve the charge transport performance, thermal annealing was also studied. The OFET device with channel geometry, W/L = 1m/2μm, was annealed at different temperature, and the electron

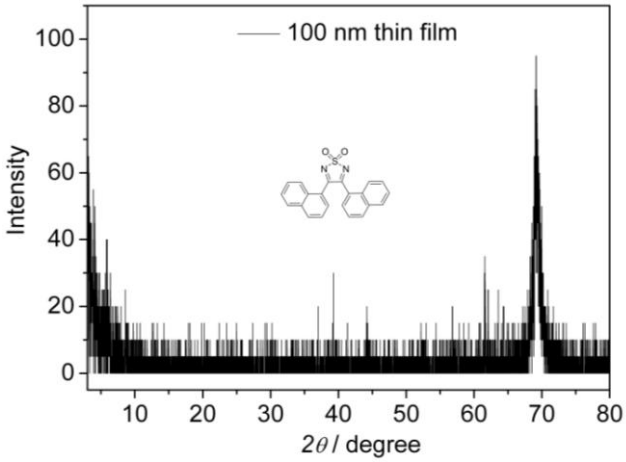

Fig. 3-9. Out-of-plane XRD pattern of **compound 22** thin film (100nm). The peak around 70^{o} is the peak of Si.

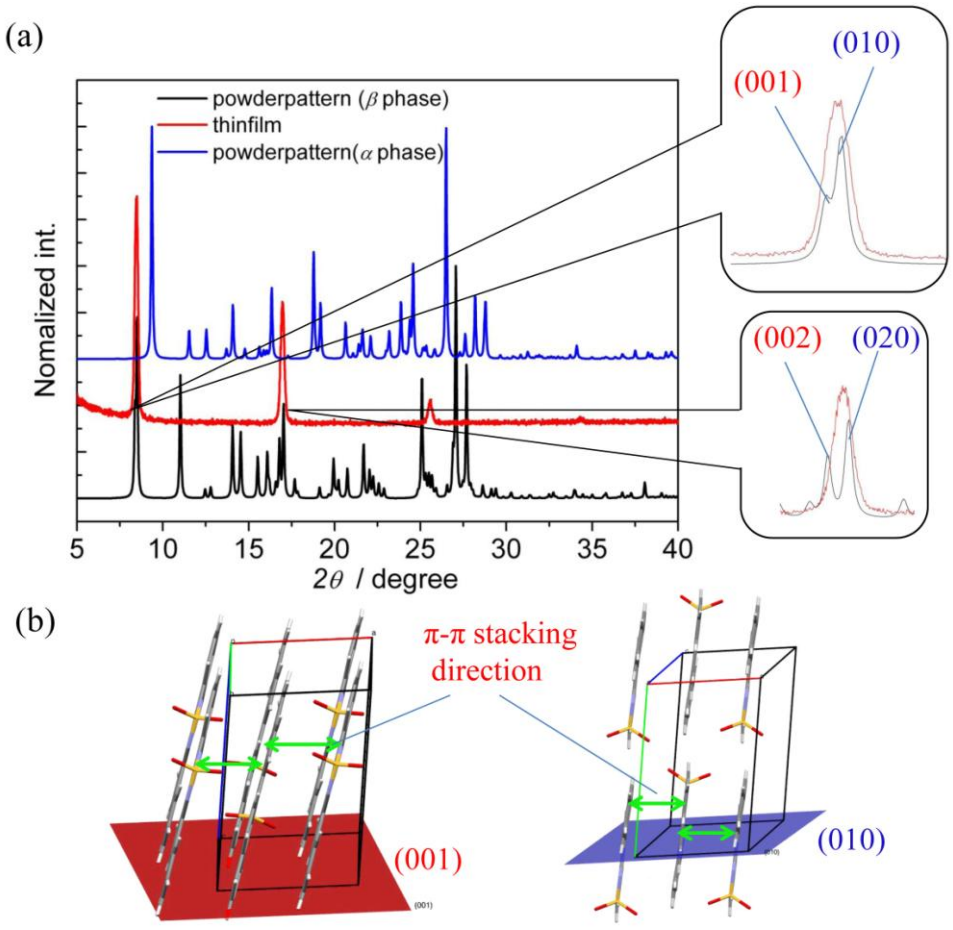

Fig. 3-10. (a) Powder-pattern simulation of **$PTDAO_2$** crystal recrystallized from DCM solution in black line; Out-of-plane XRD pattern of **$PTDAO_2$** thin film (100nm) in red line; Powder-pattern simulation of **$PTDAO_2$** crystal obtained by sublimation in blue line. Comparation of the thin-film XRD pattern and powder pattern is indicated by the enlarged Fig.s. (b) Molecular orientation on (001) and (010) planes.

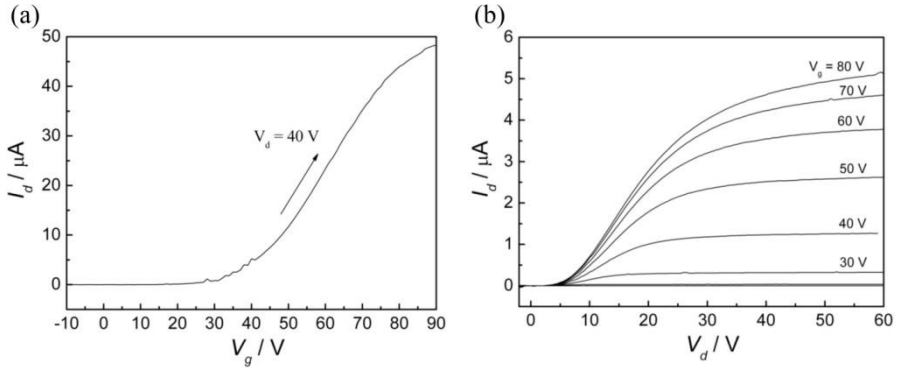

Fig. 3-11. Transfer (a) and output (b) characteristics of thin film (60nm) of **$PTDAO_2$** vacuum-deposited on SiO_2/Si at T_{sub} = rt with Pt electrodes, channel W/L = 0.2m/10μm. μ_e = 1.2×10^{-4} cm^2 $v^{-1}s^{-1}$ is calculated from the transfer characteristic.

Table 3-3**.** Electron mobilities (μ_e), current on/off ratios (I_{on}/I_{off}), and threshold voltage (V_T) for OFET devices based on **$PTDAO_2$**.

Bottom contact, bottom gate, Pt electrode, 60nm thin film						
Channel	1m/2μm	0.4m/5μm	0.2m/10μm	0.1m/20μm	0.04m/50μm	
μ_e / cm^2	1.0×10^{-4}	0.7×10^{-4}	1.2×10^{-4}	1.5×10^{-4}	0.3×10^{-4}	
V_T / V	34	29	27	28	39	
I_{on}/I_{off}	10^5	10^4	10^6	10^6	10^3	
Bottom contact, bottom gate, Pt electrode, 60nm thin film, channel W/L = 1m/2μm						
T^a / ℃	r.t.	100	140	180	220	260
μ_e / cm^2	1.0×	1.4×10^{-4}	1.8×10^{-4}	1.6×10^{-4}	1.2×10^{-4}	---
Top contact, bottom gate, 100 nm thin film, Al electrode						
Channel W/L	5cm/100μm	0.75cm/30μm				
μ_e / cm^2 $v^{-1}s^{-1}$	0.3×10^{-4}	1.0×10^{-4}				
V_T / V	36	31				
I_{on}/I_{off}	10^6	10^4				

[a] Annealing temperature of the OFET devices.

mobility was slightly improved when annealed below 220 ℃, probably because of the slight change of the thin film structure after annealing (Table 3-3). The top-contact, bottom-gate-type FET devices of **$PTDAO_2$** OFETs were preparered as well, and they showed similar charge transport performance with the bottonm-contact ones, as shown in Table 3-3.

N-type semiconductor properties in picene derivative **PTDAO$_2$** were achieved in its thin-film OFET devices, but the obtained electron mobility was not so high even after applying sevaral methods for thin-film preparation. In order to figure out the reason for the low moblity, the intermolecular hopping carrier mobility of the obtained crystal was calculated on the basis of Marcus theory.[13] The calculated parameters and the evaluated intermolecular carrier mobilities along the selected crystal axes are listed in Table 3-4. In each case, electron mobilities of 6.0 ~ 6.9 $\times 10^{-2}$ $cm^2 V^{-1} s^{-1}$ were predicted along π-stacking directions and 10^{-5} ~ 10^{-3} $cm^2 V^{-1} s^{-1}$ in the other directions (Fig. 3-12 and Table 3-4). A major reason for the lower mobility than that in the parental picene crystal could be attributed to the relatively large reorganization energy (λ). Although the thiadiazole dioxide moiety is good at stablizing anionic species, it increases the reorganization energy as well. Another reason would be the different orbital symetries of frontier molecular orbitals of **PTDAO$_2$** in comparison with that of picene. The orbital symmetries were not kept through the introduction of thiadiazole dioxide moiety. Although the experimentally obtained electron mobilities on the thin film device are still lower than the theoretical evaluation, the packing structure in thin-film would not be perfectly the same with that in the single crystal utlized for the theoretical calculation, and thin-film should contain many grain boundaries which can act as traps for charge carriers. These problems could be solved by improving the thin film crystallinity.

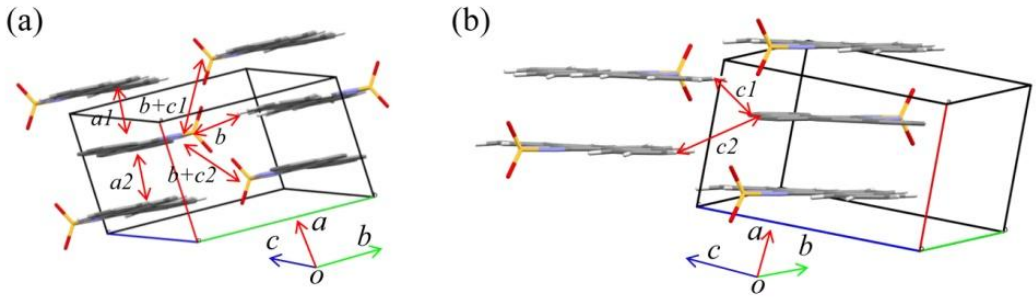

Fig. 3-12. Effective intermolecular contacts in **PTDAO$_2$** crystal along each axis.

Table 3-4**.** Theoretical estimated intermolecular transfer intergrals (*Hab*), overlap intergrals (*Sab*), center-to-center distances (*d*), orbital interaction energy (*V*), reorganization energy (λ) and hopping mobilities for each molecular contact.

Contact[a]	*Hab*[b] /meV	*Sab*[b] /meV	*d* /Å	*V* /meV	λ[c] /m eV	$\mu_{hopping}$ / $cm^2\ V^{-1}\ S^{-1}$
a_1	-150.6	15.8	4.120	-82.3	348.6	6.9×10^{-2}
a_2	-140.1	14.7	4.118	-76.8	348.6	6.0×10^{-2}
b	-14.4	1.7	10.235	7.4	348.6	3.4×10^{-3}
c_1	-3.5	0.4	10.682	-2.0	348.6	2.7×10^{-4}
c2	2.0	-0.1	10.270	1.7	348.6	1.9×10^{-4}
$b+c_1$	-2.6	0.3	14.863	-1.2	348.6	1.8×10^{-4}
$b+c_2$	1.7	-0.2	13.975	0.9	348.6	9.1×10^{-5}

[a] Corresponding molecular contacts are indicated in Fig. 3-12. [b] Calculated in PW91/TZ2P level. [c] Calculated in B3LYP/6-31G(d) level.

3.2.6 Preparation, crystal structures, and magnetic properties of anion radical salts

As described above, **$FPTZO_2$** and **$PTDAO_2$** have low LUMO energies (-4.26 eV and -4.11 eV, respectively) indicating the good acceptor abilities. They could be easily reduced to afford anion radicals by electrochemical reduction or by chemical reducing reagents. Fig. 3-13 shows an EPR spectrum of anion radical of **$PTDAO_2$** in DCM solution obtained by electrochemical reduction, and a simulated EPR spectrum. The EPR spectrum showed seven peaks. The existence of these peaks is due to the coupling of nitrogens and hydrogens. By applying the hyperfine coupling constants for the simulation, it is known that two nitrogens and eight hydrogens mainly affected the spin of this molecule. The spin densities obtained from hyperfine coupling constants (***a***) of EPR spectrum were compared with the spin densities calculated by DFT computation (Table 3-5). They have much difference (Fig. 3-15), so the experimental spin densities were arranged to the atoms according to the tendency of the theoretical values. These spin densities indicate the delocalization of spin in the whole molecule. The negative spin densities in the theoretical result indicate the spin polarization of this molecule.

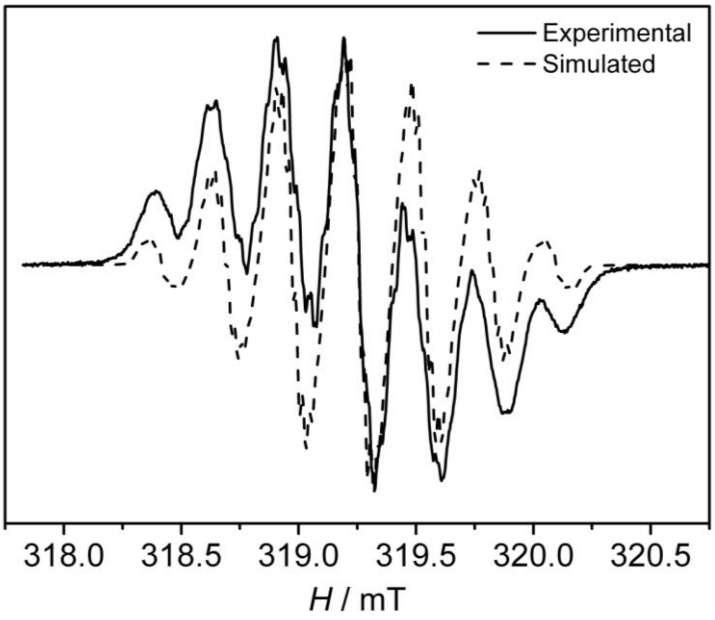

Fig. 3-13. Solution EPR spectrum of reduced **PTDAO$_2$** in DCM at room temperature

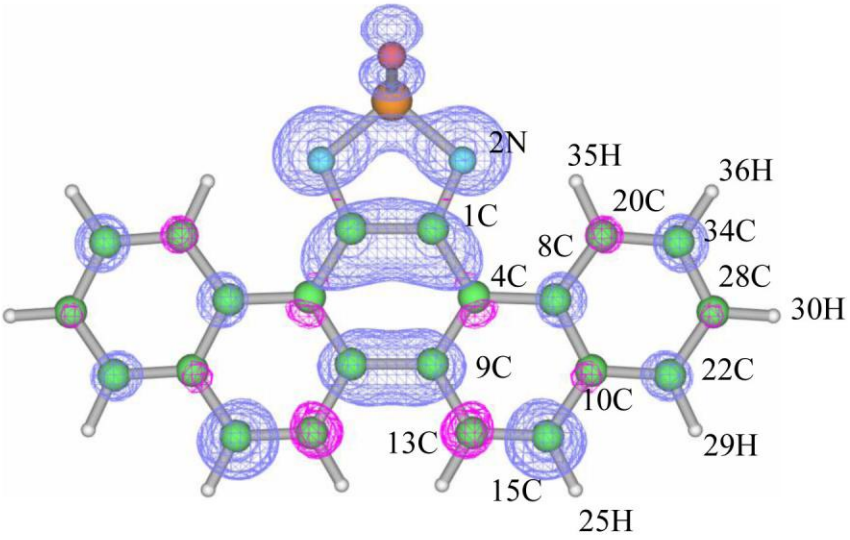

Fig. 3-14. Calculated spin densities of **PTDAO$_2$** molecule with number scheme.

Table 3-5. Spin densities of **$PTDAO_2$** radical obtained from the hyperfine coupling constants (***a***) of the EPR spectrum and the theoretical calculation.

a (hyperfine)		Experimental values [a]			Theoretical values [b]		
N	H	N	C	H	N	C	H
0.29	---	0.116	---	---	0.245(2N)	---	---
	0.26		0.106	0.0051		0.044(1C)	-0.001(35H)
	0.055		0.022	0.0011		0.023(4C)	-0.0014(36H)
	0.025		0.01	0.0005		0.012(8C)	0.0001(30H)
	0.023		0.01	0.0005		-0.008(20C)	-0.0013(29H)
						0.026(34C)	-0.0041(25H)
						-0.007(28C)	0.0014(23H)
						0.026(22C)	
						-0.014(10C)	
						0.085(15C)	
						-0.041(13C)	
						0.064(9C)	

[a] Spin densities were calculated from the hyperfine coupling constants according to the McConnell equation $a = Q\rho$ (Q (N) = 2.5 mT, Q (C) = 2.5 mT and Q (H) = 50.8 mT). [b] Theoretical spin densities were calculated by DFT method (B3LYP/6-31G (d)). The corresponding atoms' numbers are shown in Fig. 3-14.

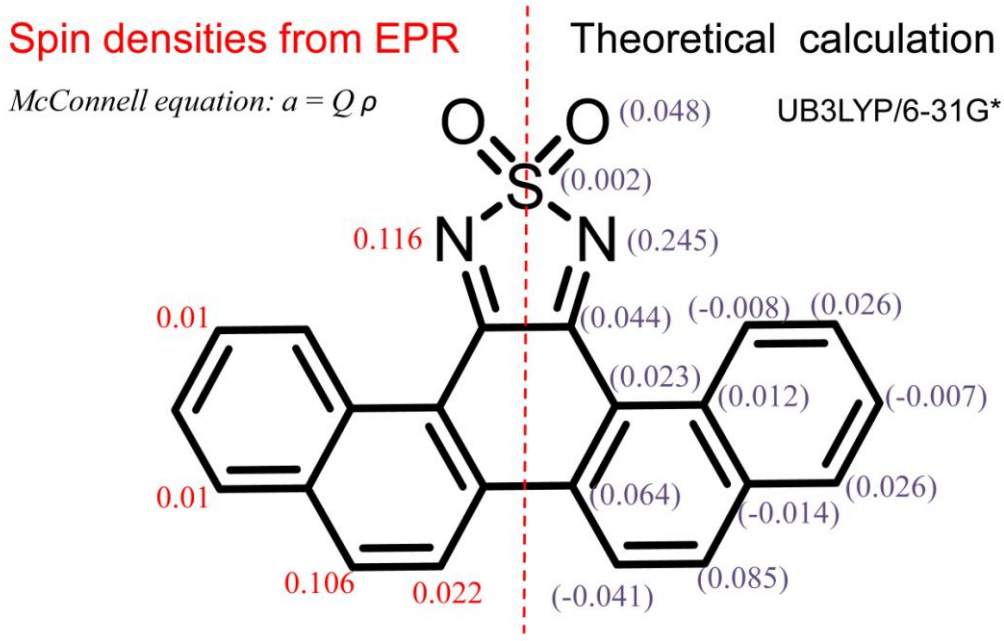

Fig. 3-15. Comparison of experimental spin densities and theoretical spin densities of **$PTDAO_2$** radical.

Since the experimental spin densities and theoretical spin densities were not agree well (Fig. 3-15), solvent and counter cation for electrochemical reduction were changed to get the crystal. Finally, the anion radical salt of **PTDAO$_2$** was obtained as black crystals in the presence of tetraethylammonium (TEA) ions as counter cations. In the crystal, cation and anion are 1:1 ratio, and **PTDAO$_2$** anion molecule has bent structure as shown in Fig. 3-16(b). **PTDAO$_2$** molecules formed dimers in the crystal (Fig. 3-16) divided by the tetraethylammonium (TEA) cations.

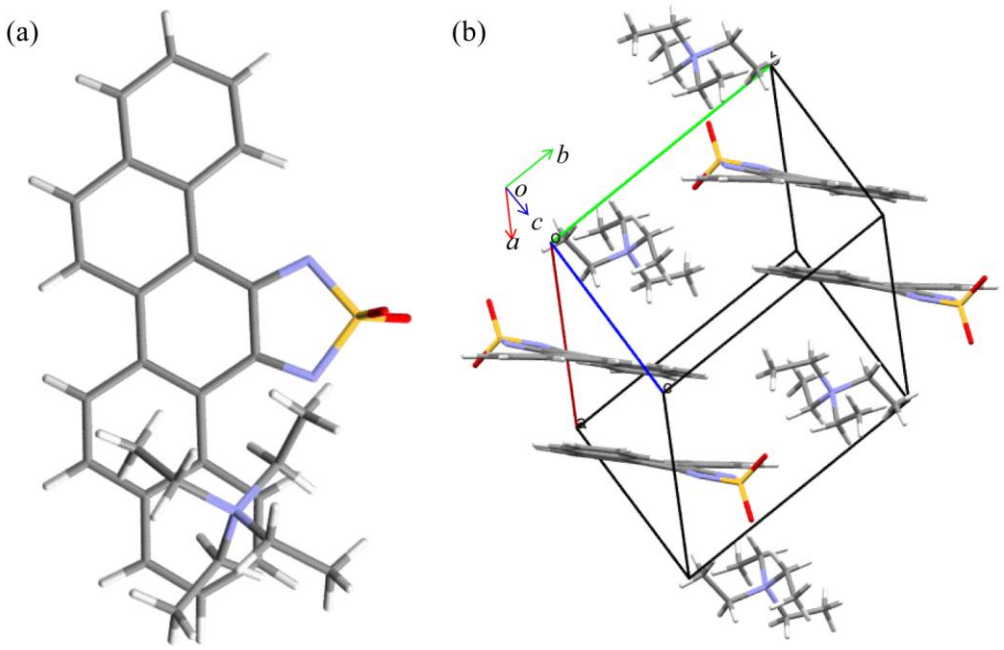

Fig. 3-16. Crystal structure of [TEA][PTDAO$_2$]. Top view (a) and molecules in one crystal cell (b). $C_{30}H_{32}N_3O_2S$; *triclinic*; $P\bar{1}$; a = 10.225(2) Å, b= 11.270(3) Å, c = 12.198(3) Å, α = 109.706(3)^o, β = 105.9272(2)^o, γ = 92.218 (2)^o, V = 1259.1(5) Å^3. Z =2, T=173K, R_1 =0.0429 (I>2.00s(I)), GOF = 1.010.

The bond lengths of **PTDAO$_2$** radical were compared with those of neutral **PTDAO$_2$** (β-phase) molecule (Table 3-6). Red values indicated the elongated bonds of **PTDAO$_2$** radical in comparison with those of neutral **PTDAO$_2$** (β-phase) molecule. Blue values indicated the shortened bonds of **PTDAO$_2$** radical in comparison with those of neutral **PTDAO$_2$** (β-phase) molecule. The change of the bond lengths were also illustrated in Fig. 3-17. In the LUMO orbital of **PTDAO$_2$**, the bonds with the same sign of coefficients should be shortened, while the bonds with opposite signs of coefficients should be elongated by gaining an electron. The tendency of change of

bond lengths in **$PTDAO_2$** radical is consistent with the distribution of LUMO of **$PTDAO_2$** which indicates the distribution of LUMO was demonstrated experimentally.

Table 3-6. Bond lengths of **$PTDAO_2$** radical and bond lengths of neutral **$PTDAO_2$** (β-phase) molecule. Red values indicated the elongated bonds of **$PTDAO_2$** radical in comparison with those of neutral **$PTDAO_2$** (β-phase) molecule. Blue values indicated the shortened bonds of **$PTDAO_2$** radical in comparison with those of neutral **$PTDAO_2$** (β-phase) molecule.

Bonds	[$PTDAO_2$] Anion radical	$PTDAO_2$ (β) Neutral
S-O1	1.445(1)	1.425(2)
S-N1	1.640(2)	1.670(2)
N1-C1	1.337(2)	1.292(2)
C1-C2	1.438(2)	1.450(2)
C2-C3	1.457(2)	1.444(2)
C3-C4	1.412(2)	1.421(3)
C4-C5	1.376(2)	1.373(2)
C5-C6	1.399(2)	1.402(3)
C6-C7	1.362(3)	1.359(3)
C7-C8	1.418(2)	1.415(2)
C8-C9	1.418(2)	1.410(3)
C3-C8	1.427(2)	1.430(3)
C9-C10	1.357(3)	1.365(3)
C10-C11	1.430(2)	1.419(3)
C2-C11	1.408(2)	1.402(2)
C11-C12	1.466(2)	1.490(2)
C1-C13	1.470(2)	1.527(2)

The corresponding atoms' numbers are shown in Fig. 3-17.

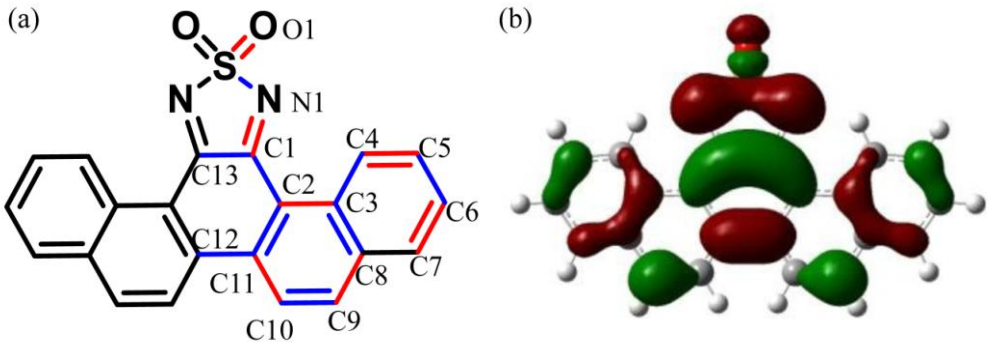

Fig. 3-17. Tendency of the change of bond lengths of **$PTDAO_2$** radical, red bonds indicated the elongated ones, blue bonds indicated the shortened ones (a). molecular orbital distribution of LUMO of **$PTDAO_2$** (b).

The EPR spectrum of [TEA][$PTDAO_2$] showed broad peak at g = 2.0093 indicates that the existence of radical species in the crystals (Fig. 3-18). Small shoulder peaks in the EPR spectrum illustrates the anisotropy of the radical molecule in the crystal. The anisotropy was further investigated in terms of the angler dependence of single crystal EPR measurement (Fig. 3-19 and Fig. 3-20).

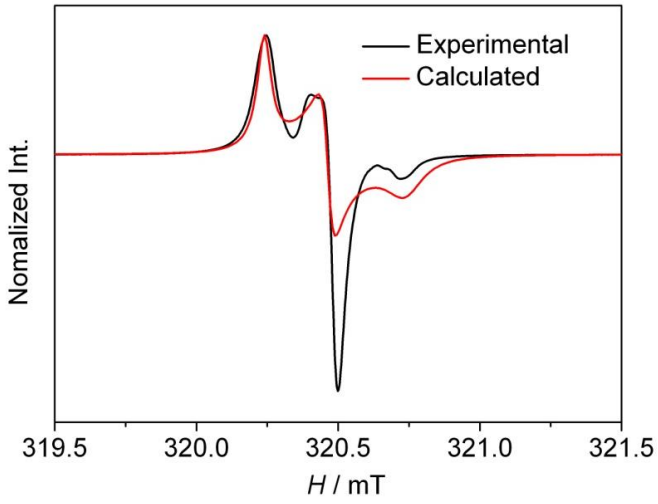

Fig. 3-18. EPR spectrum of powdered crystals of [TEA][$PTDAO_2$]. Black line is experimental data measured at room temperature. Red line is theoretical calculation with anisotropic g_x = 2.0066, g_y = 2.0052, g_z = 2.0035.

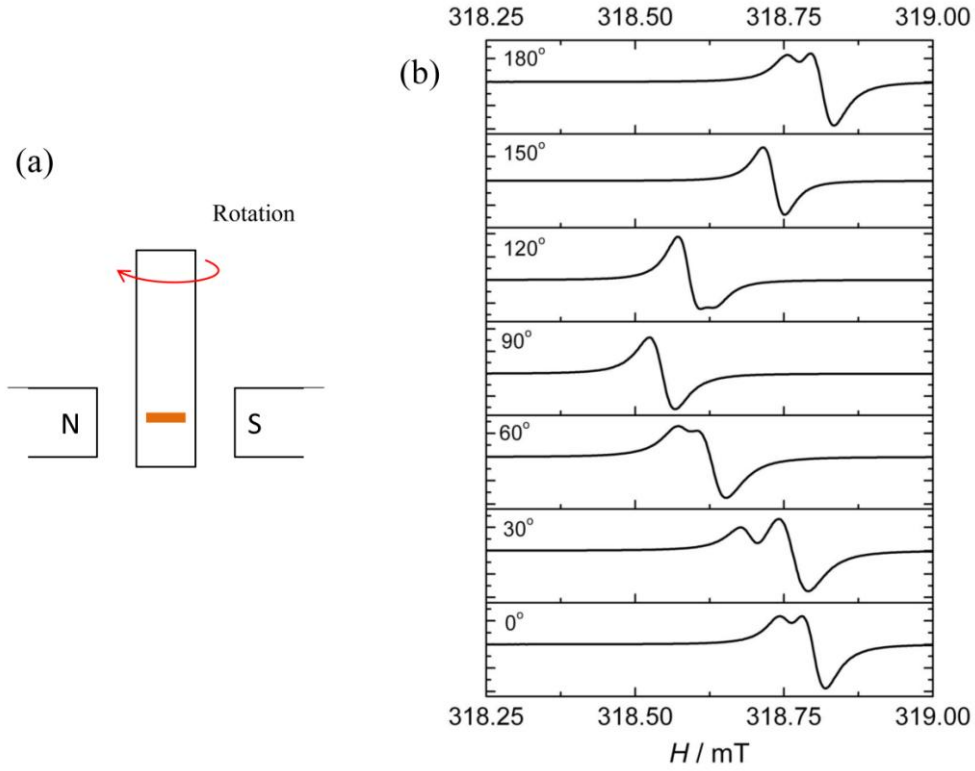

Fig. 3-19. Diagram of single crystal (horizontal direction) measurement (a) anisotropic effect of EPR (b).

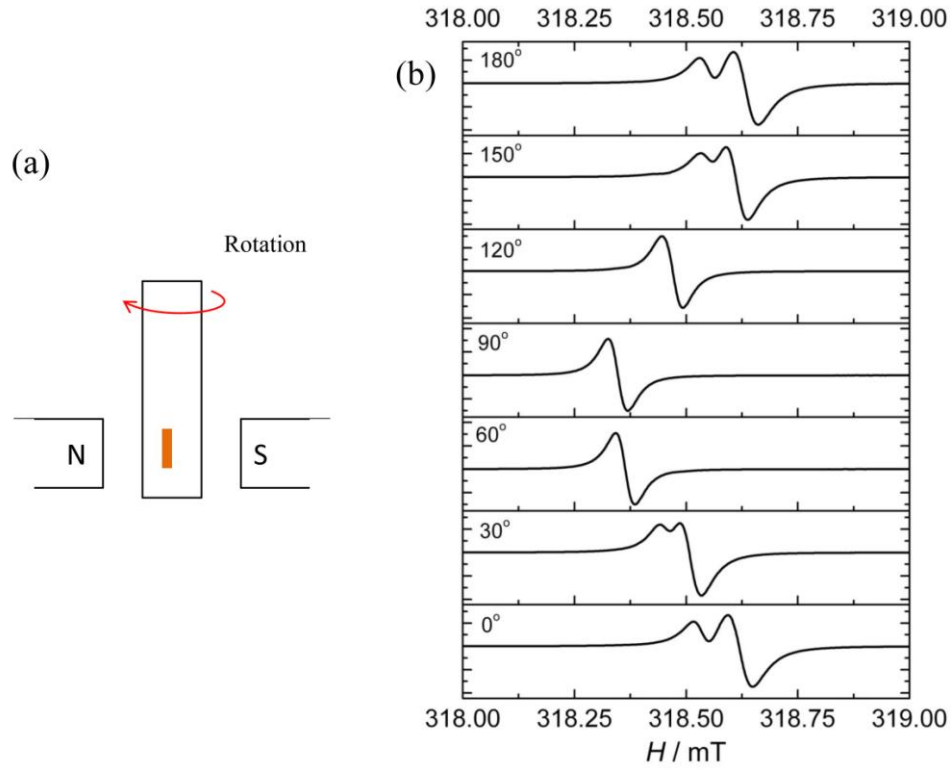

Fig. 3-20. Diagram of single crystal (vertical direction) measurement (a) anisotropic effect of EPR (b).

The magnetic susceptibility of [TEA][PTDAO$_2$] was measured on a SQUID magnetometer in the range of 2-300 K. The molar paramagnetic susceptibility (χ_p) showed a broad maximum at 62 K, and decreased in lower temperature (Fig. 3-21). The magnetic susceptibility was well reproduced (Fig. 3-21) with theoretical model on the basis of the antiferromagnetic dimer with a negative Weiss temperature of $\theta = -5.0$ K containing of 2.3% of Currie impurity (eq.1). This magnetic structure is consistent with the dimeric crystal packing. In the χ_pT vs. T plot (Fig. 3-21b), the χ_pT value at room temperature is around the curie constant (0.375) of 1/2 spin. That indicates the crystal has unpaired electron in each molecule. The decrease of the χ_pT indicated antiferromagnetic interaction attributed to the dimer molecules in the crystal. However, the inter-dimer interaction is not so strong due to the large size cation between the dimmers. If small cations such as metal ions can be introduced in the crystal, probably stronger interaction of radicals will produce interesting magnetic properties.

$$\chi = \frac{N_A g^2 \mu_B{}^2}{k_B(T-\theta)} \frac{3\exp(-2J/k_BT)}{1+3\exp(-2J/k_BT)} \quad (1)$$

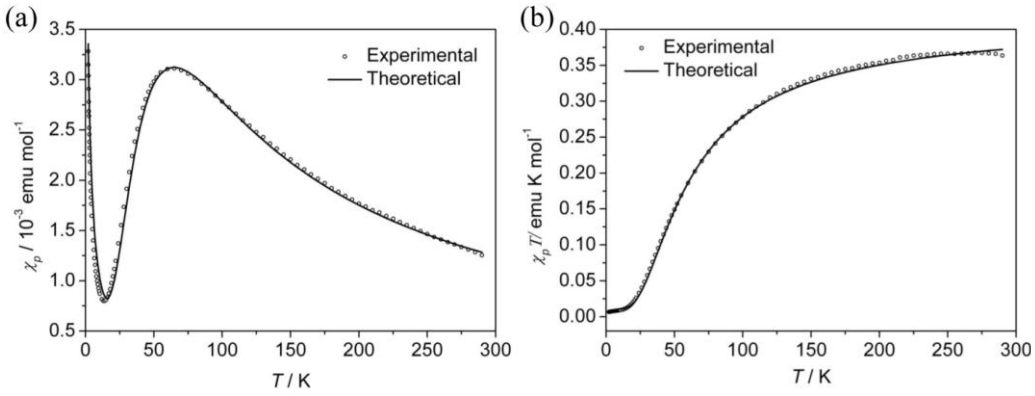

Fig. 3-21. Temperature dependence of the paramagnetic susceptibilities of crystals of [TEA][PTDAO$_2$] (solid line) and theoretical values (circled line). The dimer model fitting data gives values of $2J/k_B$ = -103K and $\theta = -5$ K.

3.3 Conclusion

In this chapter, a sereis of thiadiazole-fused aromatics were designed and synthesized, and their structures were comfirmed by NMR, EI-MS, single crystal X-ray diffraction and et al. These materials showed relatively high acceptor abilities due to the electron-withdrawing thiadiazole moiety, illustrated by the theoretical calculation and their cyclic voltammograms. Interestingly, the acceptor abilities of the thiadiazole derivatives could be tuned according to the oxidatin states of the thiadiazole ring indicated by the CV of **FPTZ**, **FPTZO$_2$** and the reported materials. By introducing the thiadiazole moiety onto π-conjugated skelton could achieve n-channel charge transport properties. The obtained material, **PTDAO$_2$** is one of the examples. The anion radical salt of **PTDAO$_2$** was also obtained with tetraethylammonium (TEA) cation which showed antiferromagnetic property due to the dimerized structures in the crystal. In conclusion, polyaromatic materials fused with thiadiazole moiety could exhibit strong acceptor ability, and they are applicable for organic electronics and magnetic materials.

3.4 Experimental section

General Procedures

All chemicals and solvents purchased were used without further purification unless otherwise stated. NMR spectra were measured using 400 MHz or 600 MHz JEOL WinAlpha A-600 using TMS as internal reference. Low resolution and high resolution EI-MS spectra were measured using JOEL JMS-T100GCV with perfluorokerosene (PFK) as matrix. Cyclic voltammetry (CV) was carried out using HOKUTO DENKO HZ-5000 under nitrogen gas. UV-vis spectra were measured by JASCO V-570. Electron paramagnetic resonance (EPR) was measured by JOEL JES-FA 200 ESR spectrometer.

Preparation of 16

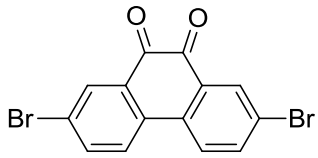

2,7-dibromophenanthrene-9,10-dione (12)

NBS (3.91g, 22 mmol) was slowly added to the a mixture of phenanthrene-9,10-dione (**11**) (2.08g, 10 mmol) in concentrated H_2SO_4 (98%) (40 mL) at room temperature. The mixture became dark blue suspension. Then the mixture was stirred for 2 hours at room temperature. The reaction mixture was poured into crushed ice and left for 1 hour with stirring. The orange product was filter off and washed by water. Finally, the filter cake was recrystallized in DMSO to yield an orange solid (2.05g, yield: 56%). The HNMR data is consistent with the literature.[14]

Preparation of M2

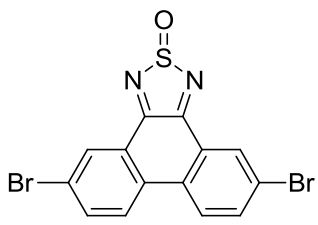

5,10-dibromophenanthro[9,10-c][1,2,5]thiadiazole 2-oxide (M2)

$NaN(SiMe_3)_2$ (1.08g, 10.0 mmol) was dissolved in toluene (100 mL) under N_2 atmosphere. Compound **12** (1.61g, 4.4 mmol) was added at 0 ^oC and stirred at room temperature for 0.5 hour. Then the mixture was heated to 60 ^oC for overnight. The volatile products were removed under reduced pressure and red crystals (compound **13**) were afforded from toluene (1.16g, 52%). Then the product compound **13** was added in thionyl chloride (15 mL) and the mixture was refluxed for overnight. After cooling to room temperature, the mixture was poured into crushed ice. The mixture was filtered, and a crude orange solid was obtained. The orange solid was dissolved in hot toluene. After cooling to room temperature, the orange precipitate was collected by filteration and washed by ethyl ether yielded an orange solid (0.89g, yield: 95%). ^1H NMR ($CDCl_3$, 400 MHz): δ 8.67 (2H, d, J = 2.0 Hz), 8.07~ 8.05 (2H, d, J = 8.4 Hz), 7.95~ 7.92 (2H, dd, J_1 = 8.2 Hz, J_2 = 2.2 Hz).

Preparation of M1

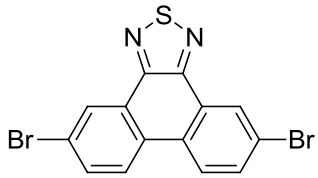

5,10-dibromophenanthro[9,10-c][1,2,5]thiadiazole (M1)

Compound **M2** (0.41g, 1.0 mmol) was added to chlorobenzene (100 ml). The mixture was heated to 130 ^oC for 2 hours. After cooling to 90 ^oC, a mixture of triphenylphosphine (0.83g, 3.2 mmol) and carbontetrachloride (1.56g, 10 mmol) in dehydrated DCM was added to the mixture. The reaction mixture was stirred at 90 ^oC overnight. Then the mixture was cooled to room temperature and evaporated in vacuum. The obtained residue was purified by chromatography, eluting with hexane/dichloromethane (3 : 1) to afford a white solid (0.33g, yield: 85%). EI-MS (M^+) for $C_{14}H_6Br_2N_2S$ calcd: 391.8; found: M^+ 391.8 (48%), $(M+2)^+$ 393.8 (100%), $(M+4)^+$ 395.8 (51%). ^1H NMR ($CDCl_3$, 600 MHz): δ 8.85 (2H, d, J = 2.4 Hz), 8.32~ 8.30 (2H, d, J = 8.4 Hz), 7.85~ 7.83 (2H, dd, J_1 = 9.0 Hz, J_2 = 2.4 Hz).

Preparation of M3

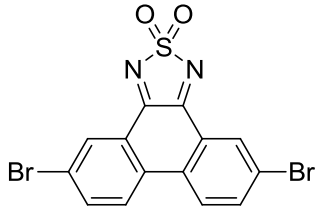

5,10-dibromophenanthro[9,10-c][1,2,5]thiadiazole 2,2-dioxide (M3)

Compound **M2** (1.23g, 3.0 mmol) was added to chlorobenzene (300 ml). The mixture was heated to 100 ^{o}C for 2 hours. After cooling to room temperature, *m*-chloroperoxybenzoic acid (3.2g, 18.0 mmol) was added to the mixture and the mixture was stirred at 80 ^{o}C overnight. Then the mixture was cooled to room temperature. The red precipitate was collected by filtration and washed by ethyl ether yielded a red solid (1.2g, yield: 94%). Crystals were obtained by recrystallization from the $CHCl_3$ solution. EI-MS (M^+) for $C_{14}H_6Br_2N_2O_2S$ calcd: 423.8; found: M^+ 423.8 (48%), $(M+2)^+$ 425.8 (100%), $(M+4)^+$ 427.8 (51%). NMR could not be obtained due to its low solubility.

Preparation of FPTZ

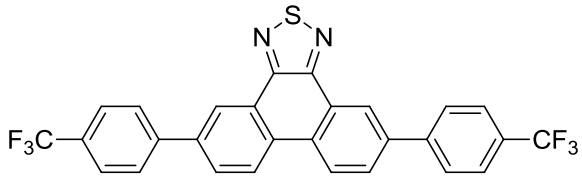

5,10-bis(4-(trifluoromethyl)phenyl)phenanthro[9,10-c][1,2,5]thiadiazole (FPTZ)

Compound **14** (0.38 g, 1.22 mmol), compound **M1** (0.21g, 0.53 mmol) and $Pd(PPh_3)_4$ (30 mg, 5%) were added to dehydrated toluene (90 ml) under N_2 atmosphere. The mixture was refluxed overnight. After cooling to room temperature, all volatiles were removed in vacuo and the residue was purified by chromatography, eluting with hexane/dichloromethane (1 : 2) to afford a light red solid (0.16 g, yield: 58%). ^{1}H NMR ($CDCl_3$, 400 MHz): δ 8.96 (2H, d, J = 2.2 Hz), 8.62~ 8.60 (2H, d, J = 8.5 Hz), 8.02~ 7.99 (2H, dd, J_1 = 8.5 Hz, J_2 = 2.0 Hz), 7.93~ 7.91 (4H, d, J = 8.1 Hz), 7.80~ 7.78 (4H, d, J = 8.1 Hz).

Preparation of $FPTZO_2$

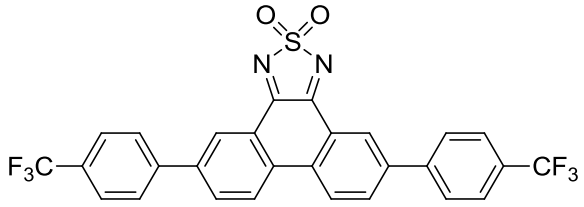

5,10-bis(4-(trifluoromethyl)phenyl)phenanthro[9,10-c][1,2,5]thiadiazole-2,2-dioxide ($FPTZO_2$)

Compound **14** (0.38 g, 1.22 mmol), compound **M3** (0.24 g, 0.56 mmol) and $Pd(PPh_3)_4$ (30 mg, 5%) were added to dehydrated toluene (180 ml) under N_2 atmosphere. The mixture was refluxed overnight. After cooling to room temperature, the mixture was filtered. The obtained filter cake was recrystallized from $CHCl_3$ yielded red crystals (0.35 g, yield: 83%). High resolution EI-MS (M^+) for $C_{20}H_8N_2S_4$ found: 556.0679; calcd: 556.0680. NMR could not be obtained due to its low solubility.

Preparation of 16

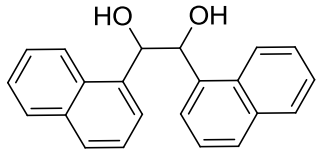

1,2-di(naphthalen-1-yl)ethane-1,2-diol (16).

Sec-butylmagnesium chloride (100 mL, 200 mmol, 2.0 M in ethyl ether) was added to the mixture of bis(cyclopentadienyl)titanium(IV) dichloride (49.8g, 200 mmol) in anhydrous tetrahydrofuran (180 mL) at -78˚C under N_2 gas. The mixture was stirred at -78 ˚C for 2 hours and then the temperature was allowed to slowly rise to room temperature for 0.5 hour. The mixture became a green suspension. 1-naphthaldehyde (23.4g, 150 mmol) was slowly added to the mixture at -78 ˚C under N_2 gas. The mixture was stirred for 3 hours. The obtained black mixture was quenched with water (20 mL), filtered, and washed by ethyl ether. The filtrate was extracted with dichloromethane (300 mL × 3) and the combined organic layers were dried over Na_2SO_4. After removing the solvent, the residue was purified by chromatography, eluting with hexane/ethyl acetate (2 : 1, 1 : 1) to afford a light yellow solid 18.7 g (yield: 80%). ^1H NMR ($CDCl_3$, 600 MHz): δ 7.87~ 7.85 (2H, d, J = 8.4 Hz), 7.74~ 7.73

(2H, d, *J* = 8.4 Hz), 7.71~ 7.70 (2H, d, *J* = 7.8 Hz), 7.68~ 7.67 (2H, d, *J* = 7.2 Hz), 7.40~ 7.37 (2H, t, *J* = 8.1 Hz), 7.37 ~ 7.34 (2H, t, *J* = 7.5 Hz), 7.28 ~ 7.26 (2H, t, *J* = 7.8 Hz), 5.78 (2H, s), 2.99 (2H, s); ^{13}C NMR ($CDCl_3$, 150 MHz): δ 136.07, 133.67, 130.88, 128.67, 128.60, 125.76, 125.34, 125.11, 124.83, 122.98, 74.42.

Preparation of 17

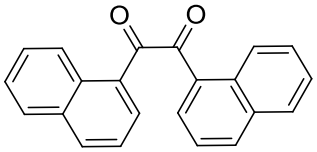

1,2-di(naphthalen-1-yl)ethane-1,2-dione (17).

Compound **16** (9.6 g, 30.6 mmol) and N-Bromosuccinimide (13.6 g, 76.0 mmol) were added to CCl_4 (150 mL). The mixture was refluxed for 5 hours. The obtained red suspension was filtered, and washed by ethyl ether. The red filtrate was extracted with dichloromethane (500 mL × 2) and the combined organic layers were dried over Na_2SO_4. After removing the solvent, the residue was purified by chromatography, eluting with hexane/dichloromethane (2 : 1, 1 : 1) to afford a yellow solid 4.6 g (yield: 49%). ^{1}H NMR ($CDCl_3$, 600 MHz): δ 9.36~ 9.35 (2H, d, *J* = 8.4 Hz), 8.14~ 8.12 (2H, d, *J* = 8.4 Hz), 8.03~ 8.02 (2H, d, *J* = 7.2 Hz), 7.97~ 7.95 (2H, d, *J* = 7.8 Hz), 7.77~ 7.75 (2H, t, *J* = 7.8 Hz), 7.66 ~ 7.63 (2H, t, *J* = 7.5 Hz), 7.51 ~ 7.48 (2H, t, *J* = 7.8 Hz); ^{13}C NMR ($CDCl_3$, 150 MHz): δ 196.93, 135.76, 135.01, 134.15, 131.19, 129.39, 128.78, 127.08, 126.07, 126.05, 124.47.

Preparation of 18

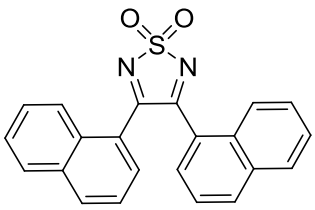

3,4-di(naphthalen-1-yl)-1,2,5-thiadiazole 1,1-dioxide (18)

Compound **17** (3.0 g, 9.7 mmol) and sulfamide (4.5 g, 47.0 mmol) were added to anhydrous ethanol (50 mL). The mixture was refluxed for 8 hours, and HCl gas was introduced during the refluxing. The mixture was treated by water (50 mL), and

extracted with dichloromethane (100 mL ×2). The combined organic layers were dried over Na_2SO_4. After removing the solvent, the residue was purified by chromatography, eluting with hexane/ethyl acetate (4 : 1, 3 : 1) to afford a yellow solid 1.03 g (yield: 40%). Crystals can be obtained by slow evaporation of the dichloromethane solution. High resolution EI-MS (M^+) for $C_{20}H_8N_2S_4$ found: 370.07756; calcd: 368.07760.^{1}H NMR ($CDCl_3$, 400 MHz): δ 8.29~ 8.27 (2H, m), 7.99~ 7.97 (2H, d, J = 8.3 Hz), 7.91~ 7.89 (2H, m), 7.60~ 7.55 (4H, m), 7.24~ 7.16 (4H, m); ^{13}C NMR ($CDCl_3$, 100 MHz): δ 165.77, 133.99, 133.57, 130.80, 130.67, 128.91, 128.62, 127.31, 124.95, 124.76, 123.82.

Preparation of $PTDAO_2$

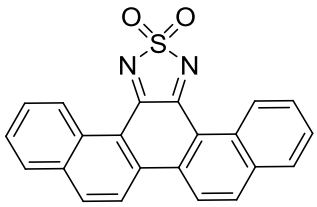

Piceno[13,14-c][1,2,5]thiadiazole 14,14-dioxide ($PTDAO_2$)

Anhydrous alumium chloride (0.74 g, 5.5 mmol) was added to the yellow solution of compound **18** (0.51 g, 1.4 mmol) in anhydrous dichloromethane (25 ml) at 0 ˚C under N_2 gas. The mixture was stirred at room temperature for 3 hours. The mixture was treated by ice-water (50 mL), and filtered. The filter cake was dried in desiccator. 0.26 g light brown solid was obtained (yield: 51%). Crystals can be obtained by sublimation at 260 ˚C in the vacuum or by slow evaporation of the dichloromethane solution. UV-vis absorption: λ_{max} = 256nm. High resolution EI-MS (M^+) for $C_{20}H_8N_2S_4$ found: 368.0623; calcd: 368.0619. ^{1}H NMR ($CDCl_3$, 600 MHz): δ 9.76~ 9.75 (2H, d, J = 7.2 Hz), 8.27~ 8.22 (4H, m), 7.89~ 7.88 (2H, d, J = 8.0 Hz), 7.80~ 7.78 (2H, t, J = 7.7 Hz), 7.64~ 7.62 (2H, t, J = 7.3 Hz); ^{13}C NMR can't be obtained due to the low solubility in common organic solvents.

Preparation of [TEA][$PTDAO_2$]

[TEA][$PTDAO_2$] was obtained by electrochemical reduction. Tetraethylammonium

perchlorate (TEAP) (20.0 mg) was added to the both side tube of an H-shape cell as an electrolyte, and **$PTDAO_2$** (6.0 mg) was added to one side of the H-shape tube. Then 1, 2-dimethylethanewas (DME) was added to the H-shape cell under N_2 gas. Current (0.5-0.9 μA) was applied to the solution by Pt electrode (**$PTDAO_2$** is in the cathode). After 2 weeks, black needle-shaped crystals had grown. The mixture was filtered and [TEA][$PTDAO_2$] was separated using microscope.

Crystal growth and X-ray analysis

Crystals of **$FPTZO_2$** were obtained by slowly evaporation of the $CHCl_3$ solution at room temperature. Crystals of compound **18** were grown by slowly evaporation of the DCM solution at room temperature. Crystals of **$PTDAO_2$** were obtained by slowly evaporation of the DCM solution at room temperature or by sublimation at 260°C ~ 280°C.

Crystals were mounted on a loop using oil (CryoLoop, Immersion Oil, Type B; Hampton Research Corp.) and set on a Rigaku RA-Micro007 with a Saturn CCD detector using graphite-monochromated Mo *K*α radiation (λ = 0.710690 Å) under a cold nitrogen steam. The frame data were integrated and corrected for absorption with the Rikagu/MSC CrystalClear package.[15] The structures were solved by direct methods[16] and standard difference map techniques, and were refined with full-matrix least-square procedures on F^2 by a Rikagu/MSC CrystalStructure package.[17] Anisotropic refinement was applied to all non-hydrogen atoms. All hydrogen atoms were placed at calculated positions and refined using a riding model.

Magnetic measurements

Magnetic susceptibility measurements were carried out on polycrystalline samples on a MPMS-XL Quantum Design magnetometer. All of the measurements used a plastic straw as the sample folder. Measurements for [TEA][$PTDAO_2$] were performed under 0.5 T in the temperature range of 2–300 K. The temperature dependences of the paramagnetic susceptibilities (χ_p) of the anion radical salts were calculated with paramagnetic susceptibilities obtained as fitting parameters.

Theoretical calculations

The molecular orbital calculations based on density functional theory were carried out using the Gaussian09, revision C.01 program package.[18] The molecular structures were optimized using HF and B3LYP methods[19] with 6-31G(d) basis sets.

Intermolecular hopping carrier mobilities were calculated on the basis of Marcus theory. First, intermolecular electronic coupling matrix elements (V) were calculated with equation 2 using intermolecular charge transfer integrals (H_{ab}), overlap integrals (S_{ab}), and the energies of the two molecular orbitals (H_{aa} and H_{bb}) calculated at PW91/TZ2P level using the ADF 2012 program package.

$$V = \frac{H_{ab} - S_{ab}(H_{aa} - H_{bb})/2}{1 - S_{ab}^2} \qquad (2)$$

Then the intermolecular charge transfer rate constants (k_{ET}) were evaluated from equation 3.

$$k_{ET} = \frac{V^2}{h}\left(\frac{\pi}{\lambda k_B T}\right)^{1/2} \exp\left(-\frac{\lambda}{4k_B T}\right) \qquad (3)$$

Where, h, k_B, and T are Planck's constant, Boltzmann constant, and temperature, respectively. The reorganization energies upon intermolecular hole transfer (λ) were obtained from $\lambda = (E^{+*} - E^{+}) + (E^{*} - E)$. Where, E, E^{+}, E^{*}, and E^{+*} were the heat of formations for an optimized neutral molecule, optimized anion molecule, neutral state on anion structure, and anion state on neutral structure, respectively, calculated at B3LYP/6-31G(d) level. Intermolecular hopping mobilities (μ) were estimated from the following equation (4).

$$\mu_{hopping} = \frac{ed^2}{k_B T} k_{ET} \qquad (4)$$

Where, d is the intermolecular center-to-center distances of adjacent molecules.

Thin-film X-ray analysis

X-ray diffractions of vapor deposited thin films on bare Si substrates were obtained by Rikagu Smartlab X-ray diffractometer with a Cu $K\alpha$ source (λ = 1.541 Å) in air.

Fabrication of the thin-film transistors

Bottom-contact, bottom-gate devices: thin films were deposited on Pt electrode with

a gap of 2 μm over a 2 × 2mm area (corresponding to 2 μm gap and 1 m width) as source/drain electrodes patterned on n-doped silicon substrates covered with 300nm-thick SiO_2 layer.

Top-contact, bottom-gate devices: thin films were deposited on silicon substrates covered with 300nm-thick SiO_2 layer, then Al was deposited on the thin films with channels of 30 μm or 100 μm at a deposition rate of 0.5 ~ 1.5 Å/s.

Prior to deposition, the substrates were cleaned by sonication in acetone and isopropyl alcohol followed by exposure to O_2 plasma. Films were deposited by vacuum sublimation (pressure ~ 5×10^{-4} Pa) at a deposition rate 0.2 ~ 0.6 Å/s. Organic field-effect transistor measurements were carried out in a vacuum with a Keithley 2636A dual channel source meter. The field-effect mobility (μ_{FET}) was calculated in the linear region of transfer curves.

3.5 Appendix

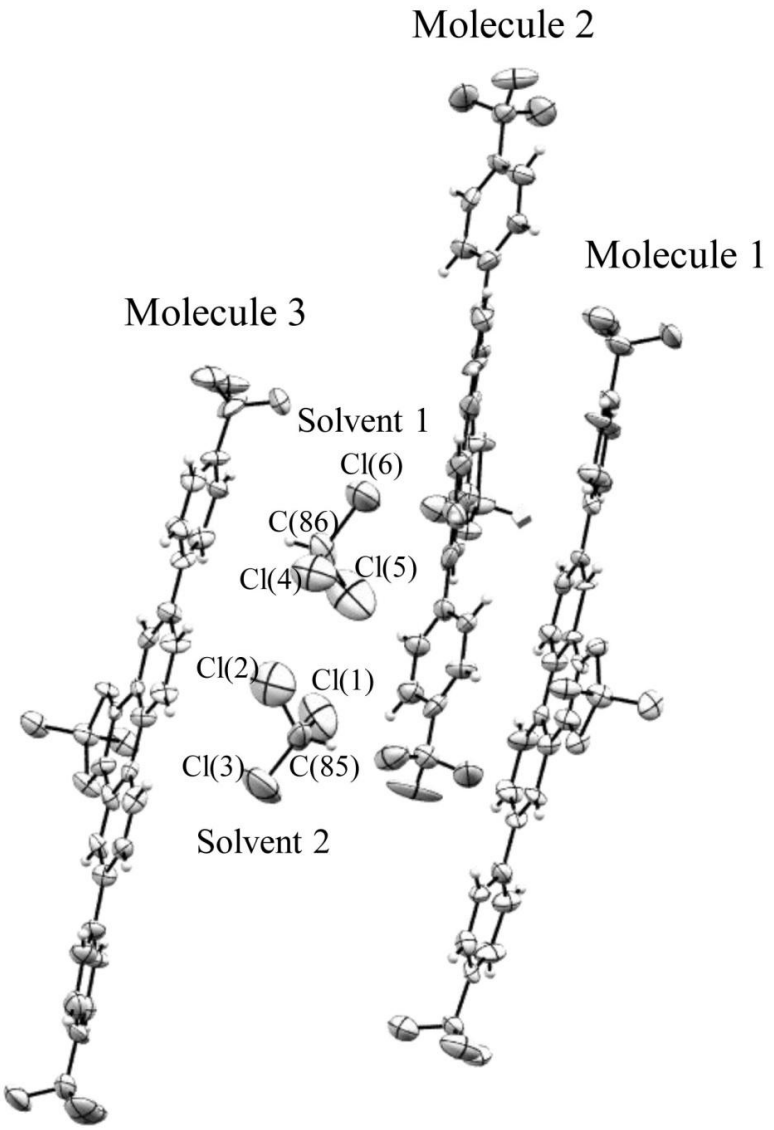

Fig. 3-22. ORTEP drawing of molecular structure of **$FPTZO_2$**

Table 3-7. Positional parameters and equivalent isotropic thermal parameters of **$FPTZO_2$ (solvent molecules) ()**

atom	x	y	z	Beq
Cl(1)	0.8606(4)	0.7316(5)	0.3779(4)	9.77(16)
Cl(2)	1.1602(5)	0.7276(4)	0.3234(4)	10.23(16)
Cl(3)	0.9841(9)	0.8741(4)	0.2065(3)	11.7(2)
Cl(4)	1.0821(5)	0.4928(4)	0.5165(4)	8.86(14)
Cl(5)	0.7953(5)	0.4689(6)	0.5696(4)	12.5(2)
Cl(6)	1.0019(8)	0.3401(3)	0.6831(3)	10.93(19)
C(85)	0.9874(18)	0.8038(9)	0.3190(10)	6.1(3)
C(86)	0.9684(19)	0.4103(11)	0.5635(10)	6.3(3)

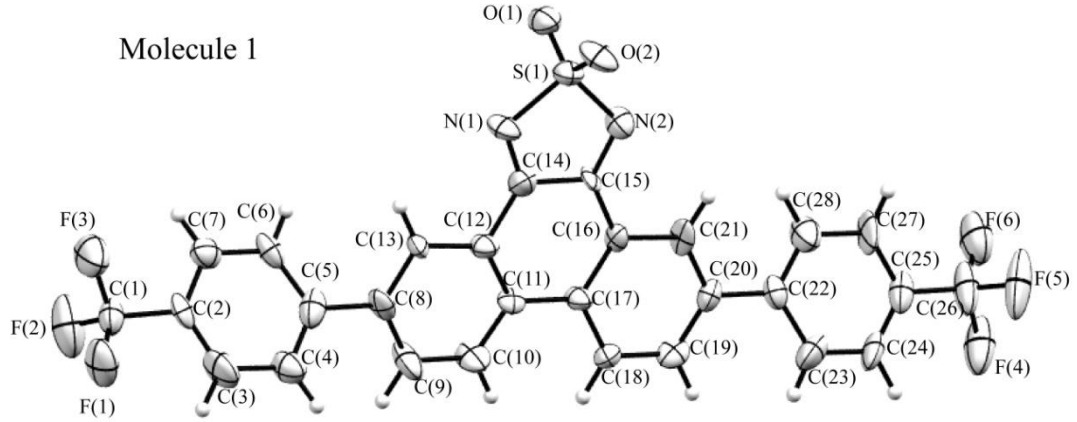

Fig. 3-23. ORTEP drawing of molecular structure of **FPTZO$_2$ (molecule 1)** with atomic numbering scheme

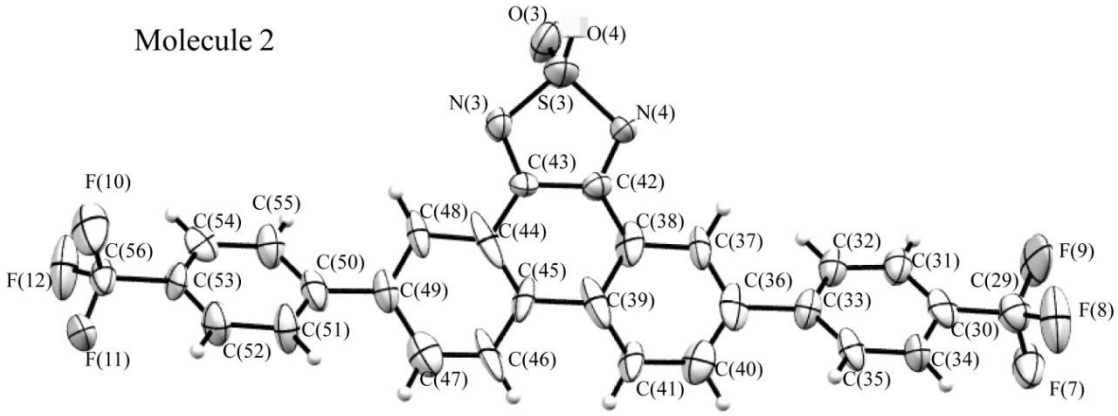

Fig. 3-24. ORTEP drawing of molecular structure of **FPTZO$_2$ (molecule 2)** with atomic numbering scheme

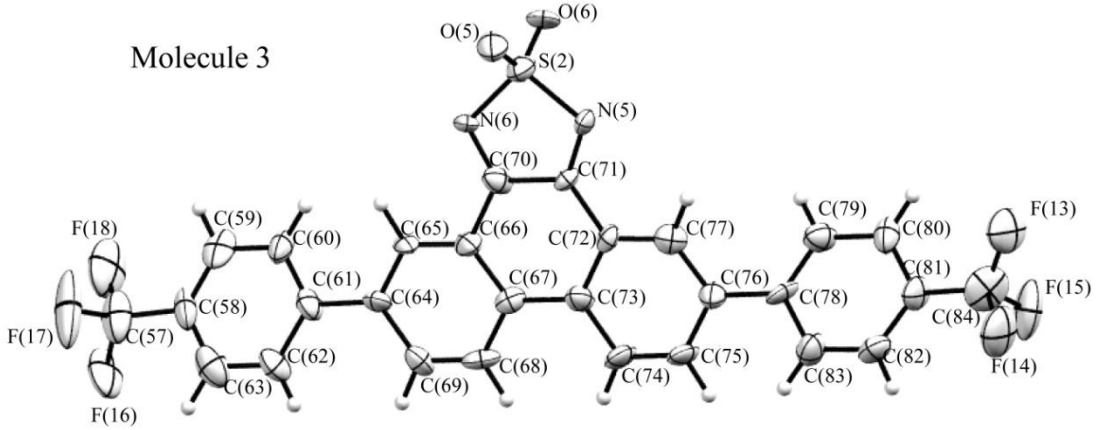

Fig. 3-25. ORTEP drawing of molecular structure of **FPTZO$_2$ (molecule 3)** with atomic numbering scheme

Table 3-8. Positional parameters and equivalent isotropic thermal parameters of **$FPTZO_2$** (molecule 1: Fig. 3-23)

atom	x	y	z	Beq
S(1)	0.3253(2)	0.75222(19)	0.8663(2)	3.19(5)
F(1)	-0.4145(7)	1.1529(5)	0.3345(5)	5.40(17)
F(2)	-0.2282(12)	1.0942(6)	0.2407(6)	7.5(2)
F(3)	-0.2082(10)	1.1968(5)	0.3034(6)	6.6(2)
F(4)	0.3033(11)	-0.0691(5)	1.2949(6)	6.8(2)
F(5)	0.3066(13)	0.0186(6)	1.3804(5)	7.9(2)
F(6)	0.4941(12)	-0.0166(6)	1.2788(6)	6.6(2)
O(1)	0.4653(8)	0.7556(5)	0.8114(6)	3.87(16)
O(2)	0.2756(8)	0.8029(6)	0.9356(6)	4.20(17)
N(1)	0.2096(9)	0.7902(6)	0.7905(7)	3.14(16)
N(2)	0.3029(9)	0.6353(5)	0.9187(6)	2.92(16)
C(1)	-0.2746(13)	1.1185(8)	0.3218(8)	3.5(2)
C(2)	-0.2255(11)	1.0357(8)	0.4061(7)	2.95(19)
C(3)	-0.3212(14)	0.9736(9)	0.4623(10)	4.8(2)
C(4)	-0.2815(12)	0.8928(8)	0.5422(9)	3.8(2)
C(5)	-0.1449(14)	0.8756(8)	0.5570(8)	3.7(2)
C(6)	-0.0446(11)	0.9373(7)	0.4933(8)	2.99(19)
C(7)	-0.0900(11)	1.0179(8)	0.4197(8)	3.3(2)
C(8)	-0.0935(9)	0.7891(8)	0.6360(7)	2.84(19)
C(9)	-0.1458(14)	0.7034(8)	0.6603(9)	4.3(2)
C(10)	-0.0969(13)	0.6213(7)	0.7347(9)	3.8(2)
C(11)	0.0005(10)	0.6203(7)	0.7823(7)	2.19(16)
C(12)	0.0483(10)	0.7084(7)	0.7574(7)	2.62(18)
C(13)	0.0058(10)	0.7943(7)	0.6817(6)	2.42(17)
C(14)	0.1577(11)	0.7125(8)	0.8045(8)	3.1(2)
C(15)	0.2131(9)	0.6221(6)	0.8813(6)	1.99(15)
C(16)	0.1566(9)	0.5352(6)	0.9054(7)	2.17(16)
C(17)	0.0508(11)	0.5331(7)	0.8589(8)	2.69(18)
C(18)	-0.0065(10)	0.4470(7)	0.8880(7)	2.53(17)
C(19)	0.0409(11)	0.3635(7)	0.9629(8)	2.88(19)
C(20)	0.1436(10)	0.3638(7)	1.0071(7)	2.56(17)
C(21)	0.2027(9)	0.4488(6)	0.9799(7)	2.89(19)
C(22)	0.1980(11)	0.2750(8)	1.0801(7)	2.88(19)
C(23)	0.1171(14)	0.1977(9)	1.1269(8)	4.1(2)
C(24)	0.1695(15)	0.1114(8)	1.1929(8)	3.9(2)
C(25)	0.2965(15)	0.0987(8)	1.2182(8)	3.7(2)
C(26)	0.354(2)	0.0102(9)	1.2889(10)	5.6(3)
C(27)	0.3780(17)	0.1721(8)	1.1752(9)	5.4(3)
C(28)	0.3266(14)	0.2584(8)	1.1061(9)	4.2(2)

Table 3-9. Positional parameters and equivalent isotropic thermal parameters of **$FPTZO_2$** (molecule 2: Fig. 3-24)

atom	x	y	z	Beq
S(3)	0.0278(3)	0.1003(2)	0.9249(2)	4.89(7)
F(7)	0.5242(8)	0.7656(5)	0.4700(6)	6.3(2)
F(8)	0.3733(12)	0.8191(5)	0.5766(6)	7.6(2)
F(9)	0.3006(12)	0.7768(6)	0.4840(8)	9.3(3)
F(10)	0.4290(9)	-0.5527(6)	1.4286(6)	7.3(2)
F(11)	0.6502(8)	-0.5662(5)	1.4098(7)	6.6(2)
F(12)	0.5643(11)	-0.6052(5)	1.3181(6)	7.2(2)
O(3)	0.0021(9)	0.0685(5)	0.8608(6)	5.32(18)
O(4)	-0.0920(5)	0.1272(5)	0.9829(6)	6.2(2)
N(3)	0.1474(8)	0.0143(5)	0.9895(5)	3.38(14)
N(4)	0.1298(7)	0.1900(5)	0.8693(5)	3.13(13)
C(29)	0.4013(14)	0.7503(9)	0.5319(9)	4.1(2)
C(30)	0.4075(13)	0.6494(8)	0.6022(10)	4.2(2)
C(31)	0.3564(12)	0.5773(8)	0.5843(9)	3.8(2)
C(32)	0.3724(12)	0.4860(8)	0.6460(8)	3.8(2)
C(33)	0.4416(12)	0.4582(7)	0.7215(8)	3.4(2)
C(34)	0.4829(13)	0.6211(8)	0.6771(9)	4.1(2)
C(35)	0.4920(13)	0.5279(8)	0.7359(8)	3.8(2)
C(36)	0.4547(14)	0.3536(8)	0.7878(9)	4.5(2)
C(37)	0.3479(12)	0.3027(7)	0.8093(8)	3.9(2)
C(38)	0.3569(14)	0.2031(8)	0.8716(8)	4.2(2)
C(39)	0.4793(15)	0.1582(9)	0.9149(9)	5.3(3)
C(40)	0.5698(16)	0.3070(9)	0.8333(9)	4.6(2)
C(41)	0.5856(12)	0.2110(7)	0.8926(8)	4.2(2)
C(42)	0.2492(9)	0.1545(6)	0.8999(6)	2.89(15)
C(43)	0.2621(8)	0.0513(6)	0.9670(6)	2.94(15)
C(44)	0.3812(16)	0.0022(9)	1.0046(8)	5.6(3)
C(45)	0.4893(13)	0.0561(7)	0.9827(8)	3.9(2)
C(46)	0.6028(16)	0.0111(9)	1.0286(10)	5.9(3)
C(47)	0.6151(14)	-0.0800(9)	1.0916(9)	4.7(2)
C(48)	0.3843(14)	-0.0962(7)	1.0717(8)	4.0(2)
C(49)	0.5034(13)	-0.1393(8)	1.1101(8)	3.7(2)
C(50)	0.5185(13)	-0.2397(8)	1.1760(9)	4.3(2)
C(51)	0.5808(15)	-0.2715(8)	1.2558(8)	4.3(2)
C(52)	0.5891(14)	-0.3718(9)	1.3153(9)	4.6(2)
C(53)	0.5337(12)	-0.4364(7)	1.2985(7)	3.1(2)
C(54)	0.4735(11)	-0.4084(8)	1.2215(8)	3.6(2)
C(55)	0.4630(14)	-0.3117(8)	1.1574(9)	4.3(2)
C(56)	0.5441(12)	-0.5407(8)	1.3625(9)	3.8(2)

Table 3-10. Positional parameters and equivalent isotropic thermal parameters of **$FPTZO_2$** (molecule 3: Fig. 3-25)

atom	x	y	z	Beq
S(2)	0.6102(2)	0.45872(19)	0.0298(2)	3.21(5)
F(13)	1.1481(10)	0.0184(5)	0.5921(7)	7.2(2)
F(14)	1.1802(10)	0.1184(6)	0.6510(5)	6.2(2)
F(15)	1.3490(8)	0.0602(6)	0.5590(6)	6.3(2)
F(16)	0.6207(11)	1.2819(5)	-0.3986(6)	6.7(2)
F(17)	0.6195(15)	1.1980(6)	-0.4826(6)	10.0(3)
F(18)	0.4321(13)	1.2291(5)	-0.3804(7)	7.8(2)
O(5)	0.6592(9)	0.4061(5)	-0.0394(5)	4.06(17)
O(6)	0.4673(7)	0.4563(6)	0.0885(6)	3.91(17)
N(5)	0.7288(8)	0.4236(5)	0.1022(5)	2.35(14)
N(6)	0.6324(9)	0.5781(6)	-0.0269(6)	3.00(17)
C(57)	0.580(2)	1.2034(10)	-0.3959(10)	5.4(3)
C(58)	0.6217(16)	1.1120(8)	-0.3200(8)	4.1(2)
C(59)	0.5423(14)	1.0375(8)	-0.2743(8)	3.8(2)
C(60)	0.5929(13)	0.9544(7)	-0.2076(8)	3.4(2)
C(61)	0.7289(12)	0.9399(7)	-0.1884(8)	3.0(2)
C(62)	0.8108(13)	1.0126(7)	-0.2360(9)	3.8(2)
C(63)	0.7572(15)	1.0983(9)	-0.3029(9)	4.5(2)
C(64)	0.7814(9)	0.8490(7)	-0.1145(8)	2.55(18)
C(65)	0.7343(10)	0.7617(7)	-0.0864(6)	2.43(17)
C(66)	0.7822(11)	0.6829(8)	-0.0176(7)	2.86(19)
C(67)	0.8833(9)	0.6808(7)	0.0328(7)	2.28(16)
C(68)	0.9346(10)	0.7688(8)	0.0032(8)	3.1(2)
C(69)	0.8897(10)	0.8471(7)	-0.0654(7)	2.75(18)
C(70)	0.7286(10)	0.5885(7)	0.0109(8)	2.77(18)
C(71)	0.7829(8)	0.4985(6)	0.0867(6)	1.72(14)
C(72)	0.8804(9)	0.5046(7)	0.1382(6)	1.99(15)
C(73)	0.9333(10)	0.5935(7)	0.1103(8)	2.79(19)
C(74)	1.0325(10)	0.5966(8)	0.1604(8)	3.1(2)
C(75)	1.0788(10)	0.5152(7)	0.2299(8)	3.1(2)
C(76)	1.0290(11)	0.4248(7)	0.2593(8)	3.0(2)
C(77)	0.9323(9)	0.4242(7)	0.2074(7)	2.75(18)
C(78)	1.0779(10)	0.3372(7)	0.3370(8)	2.66(18)
C(79)	0.9887(11)	0.2750(8)	0.3942(8)	3.3(2)
C(80)	1.0288(13)	0.1955(7)	0.4717(8)	3.3(2)
C(81)	1.1679(11)	0.1785(7)	0.4909(8)	3.4(2)
C(82)	1.2630(10)	0.2399(8)	0.4270(8)	3.3(2)
C(83)	1.2184(11)	0.3167(9)	0.3540(8)	3.5(2)
C(84)	1.2061(13)	0.0933(10)	0.5726(11)	5.1(3)

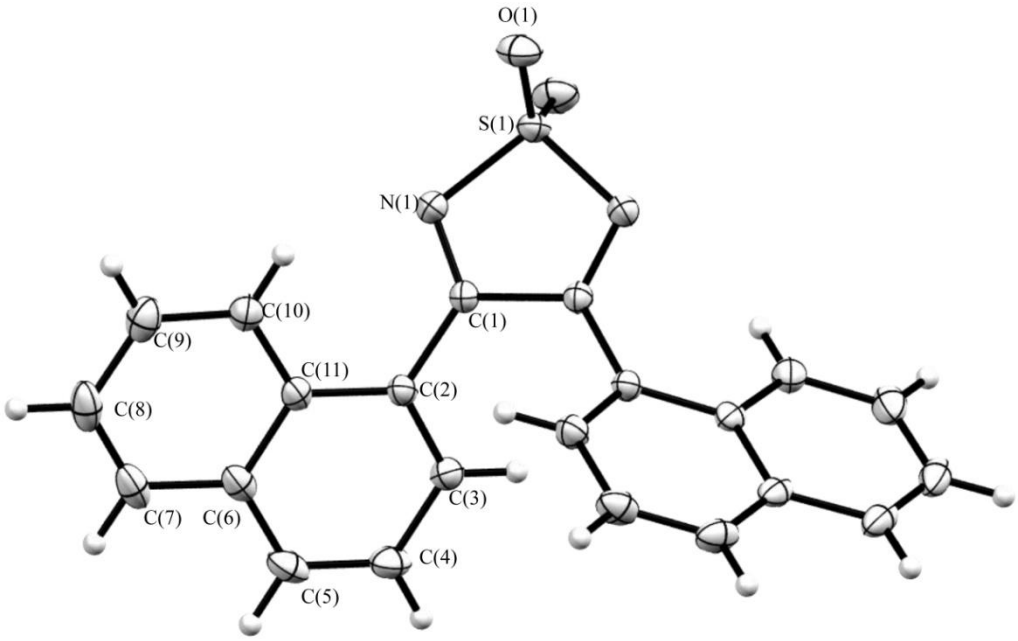

Fig. 3-26. ORTEP drawing of molecular structure of **Compound 22** with atomic numbering scheme

Table 3-11. Positional parameters and equivalent isotropic thermal parameters of **Compound 22**

atom	x	y	z	Beq
S(1)	0.5	0.55267(3)	0.25	1.515(8)
O(1)	0.49895(5)	0.61849(8)	0.39228(11)	2.289(16)
N(1)	0.43066(5)	0.45417(8)	0.19960(12)	1.614(15)
C(1)	0.45836(5)	0.34793(9)	0.21588(13)	1.356(15)
C(2)	0.41596(5)	0.23792(9)	0.16001(13)	1.412(16)
C(3)	0.44257(6)	0.15979(10)	0.06561(14)	1.732(17)
C(4)	0.40138(7)	0.06057(10)	-0.01231(15)	2.075(19)
C(5)	0.33394(7)	0.04114(10)	0.00607(15)	2.087(19)
C(6)	0.30499(6)	0.11788(10)	0.10400(14)	1.698(17)
C(7)	0.23427(6)	0.09923(11)	0.11979(16)	2.21(2)
C(8)	0.20681(6)	0.17318(13)	0.21459(16)	2.41(2)
C(9)	0.24894(7)	0.26915(12)	0.29935(16)	2.21(2)
C(10)	0.31718(6)	0.29125(10)	0.28601(15)	1.794(18)
C(11)	0.34652(5)	0.21761(9)	0.18548(13)	1.434(16)

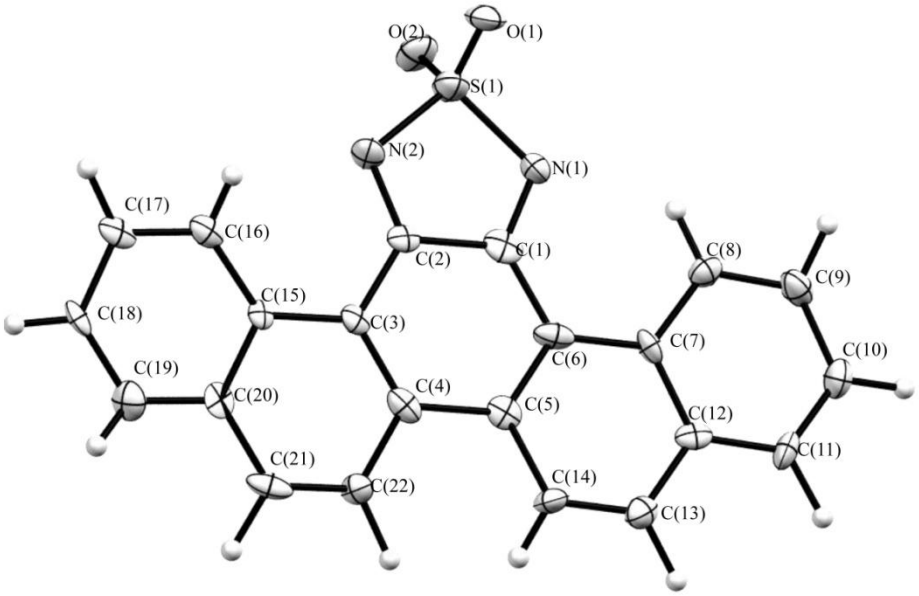

Fig. 3-27. ORTEP drawing of molecular structure of **PTDAO$_2$(α)** with atomic numbering scheme

Table 3-12. Positional parameters and equivalent isotropic thermal parameters of **PTDAO$_2$(α)**

atom	x	y	z	Beq
S(1)	0.00735(7)	0.09494(13)	0.36399(5)	2.22(2)
O(1)	-0.03615(16)	-0.0365(3)	0.39074(11)	2.23(8)
O(2)	-0.04235(17)	0.1982(3)	0.32810(12)	2.41(7)
N(1)	0.0577(2)	0.2031(3)	0.41356(14)	1.74(10)
N(2)	0.0951(2)	0.0256(3)	0.32972(14)	1.68(9)
C(1)	0.1403(3)	0.1875(4)	0.40540(18)	1.86(12)
C(2)	0.1633(2)	0.0831(4)	0.35563(17)	1.36(10)
C(3)	0.2532(2)	0.0544(4)	0.33953(16)	1.30(11)
C(4)	0.3160(2)	0.1334(4)	0.37115(17)	1.56(11)
C(5)	0.2943(2)	0.2280(4)	0.42219(18)	1.41(12)
C(6)	0.2087(2)	0.2564(5)	0.43967(19)	1.68(12)
C(7)	0.1911(2)	0.3500(4)	0.48879(18)	1.41(11)
C(8)	0.1061(2)	0.3793(4)	0.50990(17)	1.74(11)
C(9)	0.0942(2)	0.4744(4)	0.55680(16)	2.05(12)
C(10)	0.1661(3)	0.5370(4)	0.58620(17)	1.99(12)
C(11)	0.2476(2)	0.5071(5)	0.56714(17)	1.77(11)
C(12)	0.2616(2)	0.4130(4)	0.51960(17)	1.43(11)
C(13)	0.3469(2)	0.3839(4)	0.50053(17)	1.75(12)
C(14)	0.3625(2)	0.2944(4)	0.45426(18)	1.82(12)
C(15)	0.2773(2)	-0.0442(4)	0.29248(17)	1.08(11)
C(16)	0.2186(2)	-0.1297(4)	0.25855(17)	1.61(11)
C(17)	0.2474(2)	-0.2246(4)	0.21509(17)	1.72(12)
C(18)	0.3370(2)	-0.2348(4)	0.20318(16)	1.72(12)
C(19)	0.3958(2)	-0.1521(4)	0.23531(17)	2.06(12)
C(20)	0.3674(2)	-0.0568(4)	0.27919(17)	1.43(11)
C(21)	0.4279(2)	0.0322(4)	0.31068(18)	2.02(12)
C(22)	0.4040(2)	0.1246(4)	0.35403(17)	1.57(11)

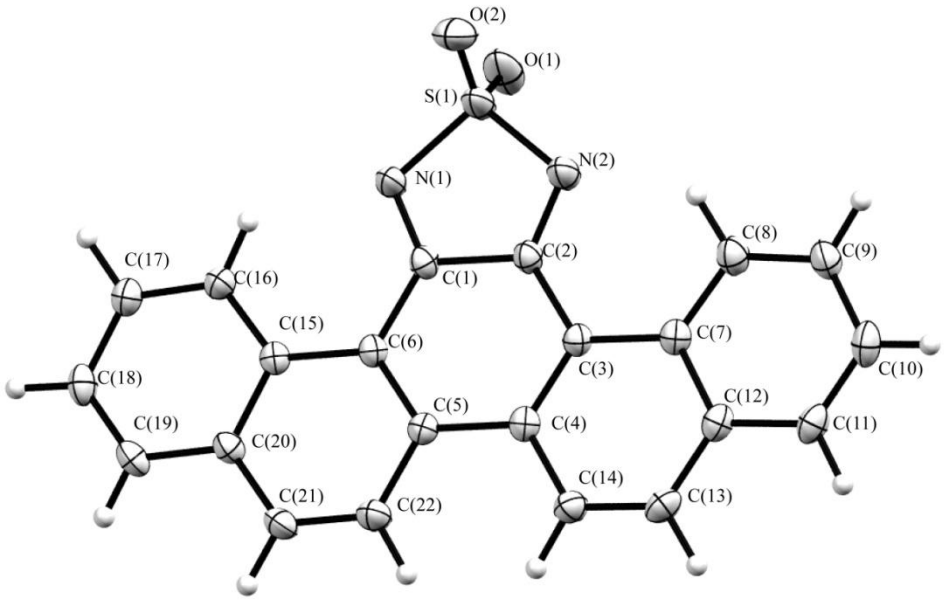

Fig. 3-28. ORTEP drawing of molecular structure of **PTDAO$_2$(β)** with atomic numbering scheme

Table 3-13. Positional parameters and equivalent isotropic thermal parameters of **PTDAO$_2$(β)**

atom	x	y	z	Beq
S(1)	0.21600(10)	0.70291(5)	0.70519(5)	2.683(18)
O(1)	0.3798(3)	0.67351(17)	0.77001(16)	3.78(4)
O(2)	0.0404(3)	0.62437(17)	0.71122(17)	3.78(4)
N(1)	0.1914(2)	0.85657(17)	0.75026(17)	2.16(3)
N(2)	0.2597(2)	0.70974(17)	0.55453(17)	2.26(3)
C(1)	0.2152(2)	0.91508(19)	0.65274(19)	1.59(3)
C(2)	0.2546(3)	0.8266(2)	0.53467(19)	1.63(3)
C(3)	0.2837(2)	0.87509(19)	0.41582(19)	1.50(3)
C(4)	0.2726(2)	1.0065(2)	0.41640(19)	1.58(3)
C(5)	0.2324(2)	1.0924(2)	0.53144(19)	1.50(3)
C(6)	0.2069(2)	1.05032(19)	0.64901(18)	1.43(3)
C(7)	0.3201(2)	0.7936(2)	0.30239(19)	1.61(3)
C(8)	0.3322(3)	0.6613(2)	0.2939(2)	2.16(4)
C(9)	0.3682(3)	0.5911(2)	0.1820(2)	2.23(4)
C(10)	0.3917(3)	0.6480(2)	0.0716(2)	2.28(4)
C(11)	0.3809(3)	0.7752(2)	0.07586(19)	2.04(3)
C(12)	0.3467(2)	0.8509(2)	0.19006(19)	1.78(3)
C(13)	0.3392(3)	0.9832(2)	0.1948(2)	2.10(3)
C(14)	0.3042(3)	1.0584(2)	0.3028(2)	1.94(3)
C(15)	0.1708(2)	1.13658(19)	0.75913(19)	1.49(3)
C(16)	0.1485(3)	1.1024(2)	0.8821(2)	1.90(3)
C(17)	0.1133(3)	1.1912(2)	0.9811(2)	2.03(3)
C(18)	0.0980(3)	1.3184(2)	0.9651(2)	2.07(3)
C(19)	0.1210(3)	1.3554(2)	0.8493(2)	2.01(3)
C(20)	0.1573(3)	1.2671(2)	0.7447(2)	1.70(3)
C(21)	0.1791(3)	1.3053(2)	0.6244(2)	2.13(4)
C(22)	0.2163(3)	1.2226(2)	0.5221(2)	2.03(3)

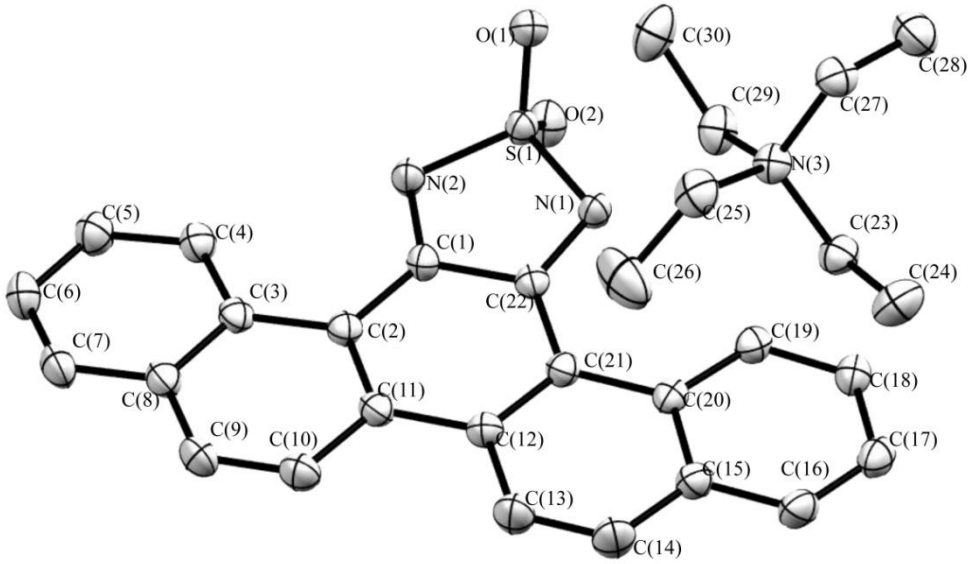

Fig. 3-29. ORTEP drawing of molecular structure of [TEA][$PTDAO_2$] with atomic numbering scheme

Table 3-14. Positional parameters and equivalent isotropic thermal parameters of [TEA][$PTDAO_2$]

atom	x	y	z	Beq
S(1)	0.23610(4)	-0.27165(4)	0.02250(3)	1.773(9)
O(1)	0.13077(12)	-0.25871(11)	-0.07786(10)	2.24(2)
O(2)	0.31271(13)	-0.37452(10)	-0.01517(11)	2.40(2)
N(1)	0.34023(14)	-0.13735(12)	0.10003(12)	1.88(2)
N(2)	0.16897(14)	-0.28496(12)	0.12618(12)	2.03(2)
N(3)	0.27455(14)	0.28763(12)	0.05674(12)	1.97(2)
C(1)	0.22475(16)	-0.18130(14)	0.22684(14)	1.71(2)
C(2)	0.19114(16)	-0.14928(15)	0.33915(14)	1.75(2)
C(3)	0.09607(16)	-0.23210(15)	0.36084(14)	1.80(2)
C(4)	0.03866(18)	-0.35792(17)	0.27940(17)	2.14(2)
C(5)	-0.0501(2)	-0.43194(19)	0.30493(18)	2.58(3)
C(6)	-0.0877(2)	-0.3844(2)	0.41239(19)	2.77(3)
C(7)	-0.0336(2)	-0.26437(19)	0.49264(18)	2.60(3)
C(8)	0.06004(17)	-0.18702(16)	0.47057(15)	2.05(2)
C(9)	0.12173(19)	-0.06468(18)	0.55824(17)	2.47(3)
C(10)	0.21525(19)	0.00883(18)	0.54015(16)	2.35(3)
C(11)	0.25318(17)	-0.02977(15)	0.43070(14)	1.88(2)
C(12)	0.35561(17)	0.05401(15)	0.41670(14)	1.92(2)
C(13)	0.4190(2)	0.17278(18)	0.51291(18)	2.64(3)
C(14)	0.5174(2)	0.25080(18)	0.50481(16)	2.78(3)
C(15)	0.56458(17)	0.21741(15)	0.40084(15)	2.09(2)
C(16)	0.67131(19)	0.29743(17)	0.39545(17)	2.43(3)
C(17)	0.72063(19)	0.26385(17)	0.29788(17)	2.34(3)
C(18)	0.66485(18)	0.14781(17)	0.20144(17)	2.09(2)
C(19)	0.55993(17)	0.06835(16)	0.20252(16)	1.85(2)
C(20)	0.50539(16)	0.10011(14)	0.30165(14)	1.75(2)
C(21)	0.39633(16)	0.01981(14)	0.31019(14)	1.72(2)
C(22)	0.32542(16)	-0.09625(14)	0.21171(14)	1.67(2)
C(23)	0.42668(19)	0.32904(18)	0.1254(2)	2.31(3)
C(24)	0.4735(2)	0.4706(2)	0.1753(2)	3.33(4)
C(25)	0.1884(2)	0.3516(2)	0.1375(2)	2.78(3)
C(26)	0.2111(3)	0.3257(3)	0.2534(2)	4.70(5)
C(27)	0.2339(2)	0.3259(2)	-0.05418(18)	2.38(3)
C(28)	0.3060(2)	0.2679(2)	-0.1481(2)	3.24(3)
C(29)	0.2494(2)	0.14352(17)	0.0186(2)	2.49(3)
C(30)	0.1053(2)	0.0812(2)	-0.0619(2)	3.22(4)

References

(1) (a) Almeataq, M. S.; Yi, H. A.; Al-Faifi, S.; Alghamdi, A. A. B.; Iraqi, A.; Scarratt, N. W.; Wang, T.; Lidzey, D. G. *Chem. Commun.* **2013**, *49*, 2252-2254; (b) Beaujuge, P. M.; Tsao, H. N.; Hansen, M. R.; Amb, C. M.; Risko, C.; Subbiah, J.; Choudhury, K. R.; Mavrinskiy, A.; Pisula, W.; Bredas, J. L.; So, F.; Mullen, K.; Reynods, J. R. *J. Am. Chem. Soc.* **2012**, *134*, 8944-8957; (c) Castro, M. C. R.; Schellenberg, P.; Belsley, M.; Fonseca, A. M. C.; Fernandes, S. S. M.; Raposo, M. M. M. *Dyes Pigm.* **2012**, *95*, 392-399; (d) Welch, G. C.; Coffin, R.; Peet, J.; Bazan, G. C. *J. Am. Chem. Soc.* **2009**, *131*, 10802-10803; (e) Wu, G. L.; Zhao, G. J.; He, C.; Zhang, J.; He, Q. G.; Chen, X. M.; Li, Y. F. *Sol. Energy Mater. Sol. Cells* **2009**, *93*, 108-113.

(2) (a) Chou, H. H.; Chen, Y. C.; Huang, H. J.; Lee, T. H.; Lin, J. T.; Tsai, C. I. T.; Chen, K. *J. Mater. Chem.* **2012**, *22*, 10929-10938; (b) Schmidt-Hansberg, B.; Klein, M. F. G.; Sanyal, M.; Buss, F.; de Medeiros, G. Q. G.; Munuera, C.; Vorobiev, A.; Colsmann, A.; Scharfer, P.; Lemmer, U.; Barrena, E.; Schabel, W. *Macromolecules* **2012**, *45*, 7948-7955; (c) Yuen, J. D.; Fan, J.; Seifter, J.; Lim, B.; Hufschmid, R.; Heeger, A. J.; Wudl, F. *J. Am. Chem. Soc.* **2011**, *133*, 20799-20807.

(3) (a) Shi, S. H.; Katz, T. J.; Yang, B. W. V.; Liu, L. B. *J. Org. Chem.* **1995**, *60*, 1285-1297; (b) Suzuki, T.; Fujii, H.; Yamashita, Y.; Kabuto, C.; Tanaka, S.; Harasawa, M.; Mukai, T.; Miyashi, T. *J. Am. Chem. Soc.* **1992**, *114*, 3034-3043; (c) Yamashita, Y.; Ono, K.; Tanaka, S.; Imaeda, K.; Inokuchi, H.; Sano, M. *J Chem. Soc. Chem. Comm.* **1993**, 1803-1805.

(4) (a) Cimrova, V.; Kminek, I.; Pavlackova, P.; Vyprachticky, D. *J Polym Sci Pol Chem* **2011**, *49*, 3426-3436; (b) Hwang, Y. J.; Kim, F. S.; Xin, H.; Jenekhe, S. A. *Macromolecules* **2012**, *45*, 3732-3739; (c) Steinberger, S.; Mishra, A.; Reinold, E.; Mena-Osteritz, E.; Muller, H.; Uhrich, C.; Pfeiffer, M.; Bauerle, P. *J. Mater. Chem.* **2012**, *22*, 2701-2712.

(5) (a) Linder, T.; Badiola, E.; Baumgartner, T.; Sutherland, T. C. *Org. Lett.* **2010**,

12, 4520-4523; (b) Shuku, Y.; Suizu, R.; Awaga, K. *Inorg. Chem.* **2011**, *50*, 11859-11861; (c) Shuku, Y.; Suizu, R.; Awaga, K.; Sato, O. *CrystEngComm* **2009**, *11*, 2065-2068; (d) Svartman, E. L.; Rozas, M. F.; Piro, O. E.; Castellano, E.; Mirifico, M. V. *Synthesis-Stuttgart* **2006**, 2313-2318; (e) Mirifico, M. V.; Caram, J. A.; Gennaro, A. M.; Cobos, C. J.; Vasini, E. J. *J. Phys. Org. Chem.* **2009**, *22*, 964-970.

(6) Helgesen, M.; Gevorgyan, S. A.; Krebs, F. C.; Janssen, R. A. J. *Chem. Mater.* **2009**, *21*, 4669-4675.

(7) (a) Algieri, A. A.; Luke, G. M.; Standridge, R. T.; Brown, M.; Partyka, R. A.; Crenshaw, R. R. *J. Med. Chem.* **1982**, *25*, 210-212; (b) Dunn, P. J.; Rees, C. W. *J. Chem. Soc., Perkin Trans.* **1989**, *12*, 2485-2487.

(8) Mitsuhashi, R.; Suzuki, Y.; Yamanari, Y.; Mitamura, H.; Kambe, T.; Ikeda, N.; Okamoto, H.; Fujiwara, A.; Yamaji, M.; Kawasaki, N.; Maniwa, Y.; Kubozono, Y. *Nature* **2010**, *464*, 76-79.

(9) (a) Kawasaki, N.; Kubozono, Y.; Okamoto, H.; Fujiwara, A.; Yamaji, M. *Appl. Phys. Lett.* **2009**, *94*; (b) Okamoto, H.; Kawasaki, N.; Kaji, Y.; Kubozono, Y.; Fujiwara, A.; Yamaji, M. *J. Am. Chem. Soc.* **2008**, *130*, 10470-10471; (c) Sugawara, Y.; Ogawa, K.; Goto, H.; Oikawa, S.; Akaike, K.; Komura, N.; Eguchi, R.; Kaji, Y.; Gohda, S.; Kubozono, Y. *Sensor Actuat B-Chem* **2012**, *171*, 544-549.

(10) Handa, Y.; Inanaga, J. *Tetrahedron Lett.* **1987**, *28*, 5717-5718.

(11) Khurana, J. M.; Kandpal, B. M. *Tetrahedron Lett.* **2003**, *44*, 4909-4912.

(12) (a) Dadvand, A.; Cicoira, F.; Chernichenko, K. Y.; Balenkova, E. S.; Osuna, R. M.; Rosei, F.; Nenajdenko, V. G.; Perepichka, D. F. *Chem. Commun.* **2008**, 5354-5356; (b) Saji, T.; Aoyagui, S. *J. Electroanal. Chem.* **1979**, *98*, 163-166. (c) LUMO = -4.8 - $E_{1/2}$ (*vs.* Fc/Fc^{+}); $E_{1/2}$ = (E_{pa} - E_{pc})/2. $E_{1/2}$ (Picene) = $E_{1/2}$ (ref. 12b) - $E_{1/2}$ (Ferrocene). $E_{1/2}$ (Ferrocene) = 0.55 V was determined in the same condition as ref. 12b.

(13) (a) Newton, M. D. *Chem Rev* **1991**, *91*, 767-792; (b) Senthilkumar, K.; Grozema, F. C.; Bickelhaupt, F. M.; Siebbeles, L. D. A. *J. Chem. Phys.* **2003**,

119, 9809-9817; (c) Senthilkumar, K.; Grozema, F. C.; Guerra, C. F.; Bickelhaupt, F. M.; Lewis, F. D.; Berlin, Y. A.; Ratner, M. A.; Siebbeles, L. D. A. *J. Am. Chem. Soc.* **2005**, *127*, 14894-14903.

(14) Satapathy, R.; Wu, Y. H.; Lin, H. C. *Org. Lett.* **2012**, *14*, 2564-2567.

(15) CrystalClear, R. C., 1999;; CrystalClear Software User's Guide, M. s. C., 2000;; Pflugrath, J. W. *Acta Crystallogr., Sect. D,* **1999**, *55*, 1718-1725.

(16) Sheldrick, G. M. *SHELX97* **1997**.

(17) Structure, C. C.; Analysis Package, R. a. R. A., 9009 New; Trails Dr., T. W., TX, USA, **2000-2007**.

(18) Frisch, M. J.; Trucks, G. W.; Schlegel, H. B.; Scuseria, G. E.; Robb, M. A.; Cheeseman, J. R.; Montgomery, J. A. J.; Vreven, T.; Kudin, K. N.; Burant, J. C.; Millam, J. M.; Iyengar, S. S.; Tomasi, J.; Barone, V.; Mennucci, B.; Cossi, M.; Scalmani, G.; Rega, N.; Petersson, G. A.; Nakatsuji, H.; Hada, M.; Ehara, M.; Toyota, K.; Fukuda, R.; Hasegawa, J.; Ishida, M.; Nakajima, T.; Honda, Y.; Kitao, O.; Nakai, H.; Klene, M.; Li, X.; Knox, J. E.; Hratchian, H. P.; Cross, J. B.; Bakken, V.; Adamo, C.; Jaramillo, J.; Gomperts, R.; Stratmann, R. E.; Yazyev, O.; Austin, A. J.; Cammi, R.; Pomelli, C.; Ochterski, J. W.; Ayala, P. Y.; Morokuma, K.; Voth, G. A.; Salvador, P.; Dannenberg, J. J.; Zakrzewski, V. G.; Dapprich, S.; Daniels, A. D.; Strain, M. C.; Farkas, O.; Malick, D. K.; Rabuck, A. D.; Raghavachari, K.; Foresman, J. B.; Ortiz, J. V.; Cui, Q.; Baboul, A. G.; Clifford, S.; Cioslowski, J.; Stefanov, B. B.; Liu, G.; Liashenko, A.; Piskorz, P.; Komaromi, I.; Martin, R. L.; Fox, D. J.; Keith, T.; Al-Laham, M. A.; Peng, C. Y.; Nanayakkara, A.; Challacombe, M.; Gill, P. M. W.; Johnson, B.; Chen, W.; Wong, M. W.; Gonzalez, C.; Pople, J. A. *Gaussian 03, revision C.02* **2004**, Gaussian, Inc.: Wallingford, CT.

(19) (a) Becke, A. D. *Phys. Rev. A: At., Mol., Opt. Phys.*, **1988**, *38*, 3098-3100; (b) Becke, A. D. *J. Chem. Phys.* **1993**, *98*, 5648-5652; (c) Lee, C.; Yang, W.; Parr, R. G. *Phys. Rev. B: Condens. Matter Mater. Phys.*, **1988**, *37*, 785-789; (d) Stephens, P. J.; Devlin, F. J.; Chabalowski, C. F.; Frisch, M. J. *J. Phys. Chem.* **1994**, *98*, 11623-11627.

Chapter 4 Conclusion

In this thesis, two series of polyaromatic molecules with hetero-atoms were developed for organic electronics: a series of thiophene-fused phenazine derivatives and a series of thiadiazole-fused aromatic molecules with hetero-atoms, sulfur and nitrogen atoms.

A series of novel thiophene-fused phenazine derivatives were developed in chapter 2. These thiophene-fused derivatives were synthesized by a simple condensation reaction between corresponding diketones and diamines. The redox potentials and the UV-Vis absorption spectra of these derivatives were significantly affected by the positions of the sulfur atoms and the alkyl groups. The donor abilities of the phenazine derivatives are weaker than that of the reported anthrancene analogues, and the optical properties of the phenazines are different from that of the anthrancene analogues due to the introduction of the nitrogen atoms. Charge transport properties were also investigated in the solid state of these materials. These thiopene-fused phenazines showed p-type charge transport characteristic in the thin-film state, and the conductivity of these thin films and single crystals exhibited large improvement of 3-5 orders of magnitude by iodine vapor doping up to 0.1 S cm^{-1}. The charge transport characteristics and conductivity of these materials suggest that these molecules are applicable for organic electronics.

In chapter 3, a series of thiadiazole-fused polyaromatic molecules were developed. Interestingly, the acceptor abilities of the thiadiazole derivatives could be tuned by changing the oxidation number at the sulfur atom on the thiadiazole ring. One of the thiadiazole-fused materials, thiadiazole-dioxide fused picene (**$PTDAO_2$**) exhibited strong acceptor ability and n-channel charge mobility in its thin-film state. In addition, **$PTDAO_2$** afforded anion radical salt with tetraethylammonium (TEA) cation which showed paramagnetic property with dimeric antiferromagnetic intermolecular interaction due to the dimeric packing structures in the crystal. These properties

illustrate that the thiadiazole-fused polyaromatic molecules could be applied for the organic electronics and magnetic materials.

In summary, two series of fused aromatic molecules with Sulfur and Nitrogen atoms were designed and synthesized. Characteristic optical and electronic properties were investigated due to the introduction of the hetero-atoms. Furthermore, the thiophene-fused phenazines, developed in this thesis, could afford metal-coordination complexes with various metal ions. This will be a promising future work of these materials. Thiadiazole derivatives with different oxidation states of **$PTDAO_2$** could be developed as well. Although the electronic properties of neutral state of these materials were mainly investigated in this thesis, charge-transfer complexes, metal-coordination complexes and ion radical salts of these molecules could be also prepared. These series of novel fused aromatic molecule can be widely applied and contributed to the field of molecular conductors, molecular magnetism, and molecular electronics.

Acknowledgements

My deepest gratitude goes first and foremost to Professor Kunio Awaga, my supervisor, for his support and guidance during the three years of my doctor course. His guidance to an interesting field of organic electronics made me learned very much knowledge in this field. He gave much suggestion during the research. Most importantly, he taught me how to think in a scientific way, how to solve the problem, and how to do research which are very important for a researcher. His meticulous and rigorous scholarship educates me how to be an excellent researcher.

I also give many thanks to Professor Michio M. Matsushita for his guidance and kind discussion of my study. During my research, he taught me various experimental techniques such as device fabrication, and various measurements; he also taught me the knowledge of theoretical calculation, and gave me much useful advice about my study. With his help, I have published a paper and another paper is in preparation. With his help, I can complete this doctor thesis smoothly.

I thank Dr. Hirofumi Yoshikawa for his help about the instruments and chemicals.

It is my pleasure to thank Professor Shigehiro Yamaguchi's group for offering the measurements of fluorescence properties and for his kind discussion, Dr. Yoshiaki Shuku for his help of various measurements and discussion, Dr. Simon Delgleish for his help of the English modification and discussion, Dr. Takuya Fujimoto for his help of the FET measurements, Dr. Laigui Hu for his help of device fabrication.

My thanks also go to Ms. Sayuri Handa, Ms. Motoko Tsuchibe, Mr. Ryosuke Kakuya, Mr. Shigemi Kondou for their help of my life, and all the other colleagues in our lab.

Last my thanks would go to my beloved family for their loving considerations and great confidence in me all through these years. I also owe my sincere gratitude to my friends who gave me their help of my life in Nagoya.

List of publications

Publications related to this thesis:

1. ***Yongfa Xie**, Takuya Fujimoto, Simon Dalgleish, Yoshiaki Shuku, Michio M. Matsushita, Kunio Awaga*.* "Synthesis, Optical Properties and Charge Transport Characteristics of a Series of Novel Thiophene-fused Phenazine Derivatives" ***Journal of Materials Chemistry C.*** **2013**, *1, 3467-3481.*
2. ***Yongfa Xie**, Michio M. Matsushita, Kunio Awaga*.* "Picene Fused with Thiadiazole-dioxide Moiety Exhibits n-channel Charge Transport Characteristics" *in preparation.*

Publications not related to this thesis:

1. *Hongwei Zhou*,* ***Yongfa Xie**, Lianjun Ren, Kai Wang.* "Sulfur-Participated Nazarov-Type Cyclization: A Simple and Efficient Synthesis for 3-Thio-1H-indenes" ***Advanced Synthesis & Catalysis.*** **2009**, *351, 1289-1292.*
2. *Hongwei Zhou*,* ***Yongfa Xie**, Lianjun Ren and Rui Su.* "Sulfur-Assisted Five-Cascade Sequential Reactions for the Convenient and Efficient Synthesis of Allyl Thiophen-2-yl Acetates, Propionates, and Ketones." ***Organic Letters.*** **2010**, *12, 356-359.*
3. *Hongwei Zhou*, Da Zhu,* ***Yongfa Xie,*** *Huafeng Huang, Kai Wang.* "$Ga(OTf)_3$-Promoted Sequential Reactions via Sulfur-assisted Propargyl-Allenyl Isomerizations and Intramolecular [4 + 2]cycloaddition for the Synthesis of 1,3-dihydrobenzo[c]thiophenes" ***The Journal of Organic Chemistry.*** **2010**, *75, 2706-2709.*